Formation of hard magnetic $L1_0$-FePt / FePd monolayers from elemental multilayers

Von der Fakultät Chemie der Universität Stuttgart zur
Erlangung der Würde eines Doktors der Naturwissenschaften
(Dr. rer. nat.) genehmigte Abhandlung

vorgelegt von

Nam Hoon Goo

geboren in Seoul, Südkorea

Hauptberichter: Prof. Dr. Gisela Schütz
Mitberichter: Prof. Dr. Eduard Arzt

Tag der mündlichen Prüfung: 18.06.2007

Max-Planck-Institut für Metallforschung

Stuttgart

2007

INDEX 1

1. Introduction

Magnetic recording has been applied widely for digital data storage in computers and multimedia applications since its first invention by Valdemar Poulsen [1]. The magnetic hard disk drive plays an important role in digital data storage with its large capacity and cheap price. In modern hard disk drive technology, the key issue is how to increase the storage density over 100 Gb/inch^2. However the pursuit of higher recording densities is limited by the thermal effect of the ferromagnetic substance known as the 'superparamagnetic effect' [2]. To overcome this problem, perpendicular magnetic recording has been proposed as an alternative to conventional longitudinal recording [3]. Perpendicular recording has the advantage in achieving higher storage densities, and suppressing the superparamagnetic effect by aligning the magnetic recording bits perpendicular to the disk plate. Therefore a lot of research works has been carried out on magnetic materials which can be used for the perpendicular magnetic recording.

The ordered $L1_0$-FePt and $L1_0$-FePd alloys are the most promising candidates as new materials for perpendicular magnetic recording media due to the high uniaxial magnetocrystalline anisotropy (K_1 (FePt) = 6.6 MJ/m^3, K_1 (FePd) = 1.8 MJ/m^3) [4-11]. The high magnetocrystalline anisotropy of FePt and FePd results in high coercivities which is the prerequisite for the thermal stability of small particles in high-density magnetic recording media. The ordered $L1_0$-FePt and $L1_0$-FePd alloys can be produced by a transformation of the disordered alloy into the ordered $L1_0$ structure. The disordered alloy has a face-centered cubic (fcc) structure and soft magnetic properties with cubic anisotropy. After the phase transformation, the unit cell of the ordered $L1_0$-phase shows a face-centered tetragonal (fct) structure. In this tetragonal structure the unit cell is composed of alternating stacks of Fe and Pt (Pd) atomic layers along the tetragonal *c*-axis. The uniaxial nature of the magnetic anisotropy of the $L1_0$-FePt and FePd ordered phases along their tetragonal *c*-axis results from the structural anisotropy.

For application of ordered $L1_0$-FePt and FePd in perpendicular magnetic recording, besides the intrinsic magnetic properties the microstructure (crystallographic texture, grain isolation, and grain size distribution) needs to be controlled. One of the most important requirements is to orient the tetragonal *c*–axis perpendicular to the film plane. This can be obtained by an epitaxial growth of $L1_0$-FePt on heated MgO (001) substrates with a Pt (001) buffer layer [12], and by

polycrystalline films with a strong (001) texture prepared from (Fe/Pt)n multilayers followed by thermal annealing [13, 14]. The transformation from the fcc disordered structure to the tetragonal $L1_0$ structure involves a distortion in the fcc unit cell due to the differences of lattice parameters between the fcc and fct unit cell. This distortion induces strains in the transformed fct crystal lattice. The way to release these stresses can control the favored direction of the tetragonal *c*-axis [15]. However, the mechanism of the epitaxial growth of $L1_0$-FePt films and the formation of a (001) texture in polycrystalline films are not clear so far.
Besides the influence of the microstructure, a strong dependence of the anisotropy constant K_1 on the degree of chemical order has been reported [16]. Therefore the intrinsic magnetic properties of $L1_0$-FePt film, such as the spontaneous polarization J_s and the magnetocrystalline anisotropy constant K_1 have to be investigated for various compositions as a function of temperature.

In this thesis, ordered $L1_0$-FePt and FePd films of different nominal compositions are prepared from Fe/Pt and Fe/Pd multilayers by annealing. In case of the $L1_0$-FePt films the composition of the films is modified by changing the individual elemental layer thicknesses in the multilayer precursors. This simple variation of the composition is the great advantage of the multilayer approach compared to sputtering single alloy layer from an alloy target. The formation mechanism of the fct phase from the multilayers and the microstructural properties are investigated. The characteristics of the hysteresis loop (coercivity $\mu_0 H_c$, remanence J_r) and of the intrinsic magnetic properties (anisotropy constant K_1, spontaneous polarization J_s, exchange constant A) of the ordered $L1_0$-FePt and FePd films are studied. The effects of the composition of the $L1_0$-FePt films on the microstructural and magnetic properties are investigated. The microstructure of these ordered $L1_0$-FePt films are then correlated to the magnetic properties with microstructural parameters by investigating the temperature dependence of the coercivity.

2. Ferromagnetism

2.1 Ferromagnetic ordering

2.1.1 Ordering due to exchange interaction

The magnetic properties of a solid are determined by the magnetic properties of its electrons. In ferromagnetic solids the atoms have permanent magnetic moments and neighbored moments are ordered parallel without applying an external magnetic field. The origin of the ordering is the quantum mechanical exchange interaction. The exchange energy can be explained by the Heisenberg Hamiltonian [17]

$$\langle H \rangle = -2J \sum \sum S_i S_j \ , \qquad (2.1)$$

where J is called the exchange integral, and S_i and S_j represent two neighbored spin moments. The sign of J determines the types of spin alignment. For ferromagnetic solids J is positive. The exchange energy corresponds to the difference in electrostatic energy between antiparallel and parallel spin alignment. The energy difference results from the principle of Pauli according to which electrons with parallel spins have large distances from each other and therefore a smaller Coulomb energy than electrons with antiparallel spins.
As long as the exchange energy is larger than the kinetic energy required for the electrons occupying higher energy levels in the parallel spin configuration the ferromagnetic spin alignment is favored.

2.1.2 Spontaneous polarization J_s

The magnetic moments $\boldsymbol{\mu}_m$ which are aligned parallel in the volume $\Delta\nu$ define the spontaneous polarization $\boldsymbol{J}_s$ or spontaneous magnetization $\boldsymbol{M}_s$ ($\mu_0 = 4\,\pi \times 10^{-7}$ Vs/Am, vacuum permeability).

$$\boldsymbol{J}_s = \mu_0 \boldsymbol{M}_s = \mu_0 \lim_{\Delta\nu \to 0} \frac{1}{\Delta\nu} \sum \boldsymbol{\mu}_m \quad \text{[T]} \qquad (2.2)$$

The spontaneous polarization is temperature dependent. With increasing temperature spin waves are excited resulting in a continuous decrease of the spontaneous polarization. If the temperature

is beyond a certain critical value, the so called Curie temperature T_C, J_s reaches zero. In general, the temperature dependence of J_s of a ferromagnetic substance follows the Bloch $T^{3/2}$ law

$$\frac{\Delta J_s(T)}{J_s(0)} = aT^{3/2} \quad . \tag{2.3}$$

The constant a contains experimental parameters. The plot of the Bloch law for a ferromagnetic solid is shown in Fig. 2.1. Above the Curie temperature the material becomes paramagnetic, i.e., the spins are randomly oriented and their thermal oscillations are uncorrelated.

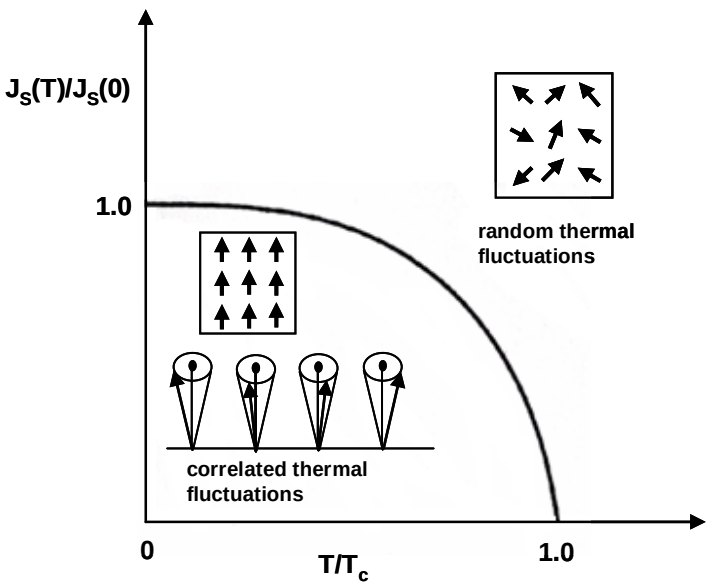

Fig. 2.1 Temperature dependence of the spontaneous polarization – Bloch's $T^{3/2}$ law.

2.2 Hysteresis loop

The magnetic behavior of a ferromagnetic material is characterized by the hysteresis loop. The hysteresis loop is obtained by measuring the field dependence of the polarization $\boldsymbol{J}$ in the specimen along the direction of the applied field $\mu_0\boldsymbol{H}$. The characteristic parameters appearing in the hysteresis loop are the saturation polarization J_s, the remanence J_r, and the coercivity $\mu_0 H_c$ (Fig. 2.2). The saturation polarization J_s gives an upper limit for the polarization which can be achieved. It is an intrinsic property of a material which is not affected by external effects, as e.g. the field direction and the shape of the sample. The remanence J_r is the polarization value obtained after applying a large field enough for saturation, and then removing it. If a specimen

has a perfect microstructure and the field is applied along its easy axis direction, the remanence J_r and saturation polarization J_s will be the same. However, various structural and geometrical features reduce the value of J_r below J_s. The coercivity, $\mu_0 H_c$ is the field needed to reduce the polarization from the remanence value to zero. According to the coercivity ferromagnetic materials can be classified into hard and soft magnets. The coercive field values of hard magnetic materials are 50 - 100 kA/m in alnico alloys, 300 kA/m in hexagonal ferrites, and exceed 1000 kA/m in FePt and CoPt alloys. Hard magnetic materials are used as stable and permanent sources for magnetic fields, and as magnetic recording media. Soft magnetic materials have low coercive field values which are of the order of 1 - 10 A/m. Typical soft magnetic materials are α-Fe, Fe-Si, Mn-Zn, and Fe-Ni (permalloy).

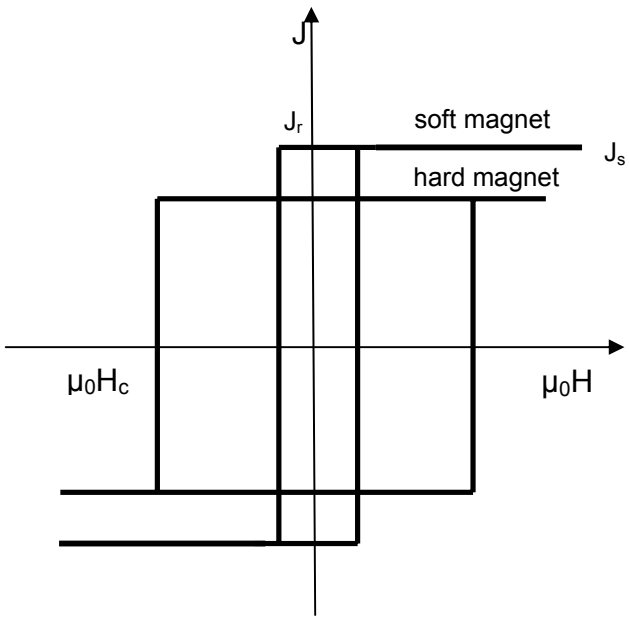

Fig. 2.2 Ideal hysteresis loops for a ferromagnetic hard and soft magnetic material.

2.3 Micromagnetism

The theory of micromagnetics is a continuum theory to predict the magnetization behavior of a specimen by considering its magnetic free energy. The magnetic free energy is expressed as a function of the position vector $\boldsymbol{r}$ and the external field $\boldsymbol{H}$. By minimizing the magnetic free energy, the vector field of the magnetization directions $\boldsymbol{J(r)} = J(r)/J_s$ is determined under the constraint J_s = constant [18, 19]. On the basis of the theory of micromagnetism it is assumed that

a magnetic material is a continuous media, and the direction cosines of the J_s vector, γ_i ($\gamma_1^2 + \gamma_2^2 + \gamma_3^2 = 1$), are also continuous functions of the positions. According to this principle, the stable configuration of the polarization vector ***J(r)*** is determined by the values of the direction cosines, and it is possible to predict the domain structures and magnetic hysteresis loops as a function of an external field.

2.3.1 Magnetic free energy

The energy terms considered in the magnetic free energy are the exchange energy, the magnetocrystalline anisotropy energy, the stray field energy, the magnetostatic energy (Zeeman energy), the surface anisotropy energy, and the magnetoelastic energy. With neglecting the surface anisotropy and magnetoelastic effects, the magnetic free energy is described as the sum of the other four energy terms.

2.3.1.1 Exchange energy

Whenever the polarization J_s changes its orientation from point to point, there is a misorientation of neighboring moments, and this costs extra energy. This energy cost is the exchange energy. The exchange energy has its origin from the Heisenberg Hamiltonian for the interacting spins and is expressed as

$$\Phi_{ex} = \int A \cdot \sum_{i=1}^{3} (\nabla \gamma_i)^2 dV = \int A\{(\nabla\theta)^2 + \sin^2\theta(\nabla\varphi)\}^2 dV \,. \tag{2.4}$$

Here, γ_i is the direction cosine of J_s, and A is the exchange stiffness constant. With the molecular field theory and the relation between J_s and the Curie temperature T_C, A is written as

$$A = \frac{J_s S^2 c}{a} = \frac{3k_B T_C S \cdot c}{2a(S+1)} \quad , \tag{2.5}$$

where S is the spin quantum number, a the lattice constant and k_B the Boltzmann constant. The parameter c counts the number of atoms in a unit cell and amounts to $c = 1$ for simple cubic

lattices, c = 2 for bcc and c = 4 for fcc lattices. The value of A can be obtained from the Bloch $T^{3/2}$ law or the specific domain wall energy. The typical value of A in FePt alloys is 1×10^{-11} J/m.

2.3.1.2 Magnetocrystalline anisotropy energy

The magnetocrystalline anisotropy energy is related to the crystal symmetry of a solid material, and the preference of the magnetization to lie in a particular direction, the so called easy axis. With the magnetocrystalline anisotropy the free energy of a magnetic material increases if ***J(r)*** deviates from the magnetic easy axis.

For cubic anisotropy (e.g. Fe, and Ni), the anisotropy energy is written as

$$\Phi_K = \int (K_0 + K_1(\gamma_1^2\gamma_2^2 + \gamma_2^2\gamma_3^2 + \gamma_3^2\gamma_1^2) + K_2(\gamma_1^2\gamma_2^2\gamma_3^2) + \cdots)dV . \tag{2-6}$$

Here, K_n are the crystalline anisotropy constants.

For uniaxial anisotropy, the energy is

$$\Phi_K = \int (K_{u0} + K_{u1}\sin^2\theta + K_{u2}\sin^4\theta + \cdots)dV \tag{2.7}$$

θ is the angle between the polarization $\boldsymbol{J_s}$ and the easy axis, and K_1, K_2 are the anisotropy constants. The anisotropy constants can be determined experimentally.

The crystalline anisotropy is mainly due to spin-orbit interaction, which makes $\boldsymbol{J_s}$ directed to a specific direction. The anisotropy constants K_1 and K_2 are a measure for the strength of the anisotropy. The values are temperature dependent. Normally they become smaller as the temperature increases and are reduced to zero when the Curie temperature is reached. In alloys, the anisotropy constants vary remarkably with the composition.

2.3.1.3 Magnetostatic energy (Zeeman energy)

The magnetostatic energy is the potential energy of a magnetic moment in an applied field and writes

$$\Phi_H = -\int \boldsymbol{H_{ext}} \cdot \boldsymbol{J_s} dV . \tag{2.8}$$

The energy is required for rotating $\boldsymbol{J_s}$ into the direction of $\boldsymbol{H_{ext}}$.

2.3.1.4 Stray field energy

The stray field energy denotes the interaction of the spontaneous polarization $\boldsymbol{J}_s$ of a ferromagnet with its own stray field $\boldsymbol{H}_s$ (dipole-dipole interaction)

$$\Phi_S = -\frac{1}{2}\int \boldsymbol{J}_s \cdot \boldsymbol{H}_s dV . \tag{2.9}$$

$\boldsymbol{H}_s$ is due to both magnetic surface charges and volume charges and is given by a potential U according to $\boldsymbol{H}_s = -\nabla U$. The potential U is obtained from solving Poisson's equation $\Delta U = \frac{1}{\mu_0} div \boldsymbol{J}_s$.

In the case of ellipsoidal samples the stray field in the sample is given by $\mu_0 \boldsymbol{H}_s = -N \cdot \boldsymbol{J}$. The N is called demagnetization factor.

2.3.2 Minimization of the magnetic free energy

The total magnetic free energy of a magnetized body is the sum of the above four energy terms, and can be minimized by first-order variation of the energy functional Φ_{total}

$$\delta\Phi_{total} = \delta(\Phi_A + \Phi_K + \Phi_S + \Phi_G) = 0 . \tag{2.12}$$

The solution of this variational problem gives the equilibrium configuration of the magnetic polarization $\boldsymbol{J}_s$ in the specimen. By minimizing the magnetic free energy, the nucleation field and the hysteresis loop of a magnetic material can be simulated [20, 21].

2.4 Magnetization processes in a multi-domain particle

In the thermally demagnetized state a ferromagnet consists of many magnetic domains. The magnetic polarization, $\boldsymbol{J}_s$ in each domain is uniform. The domains are separated by domain walls in which the direction of $\boldsymbol{J}_s$ changes from the easy axis of one domain to the other one. By the formation of domains and domain walls the large stray field energy is reduced. However, the creation of domain walls requires wall energy (exchange and magnetocrystalline energy) because of the change of $\boldsymbol{J}_s$ in direction. The equilibrium wall thickness δ is given by the exchange length of the material.

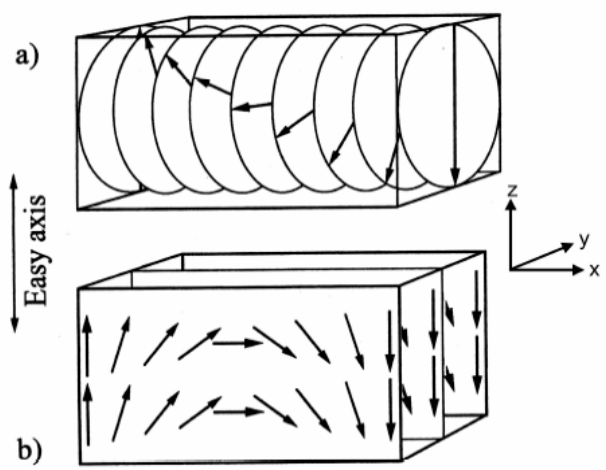

Fig. 2.3 Magnetization orientation in a 180º Bloch wall (a) and a 180º Néel wall (b) [22].

In case of a 180º wall, two types of domain walls exist. The Bloch wall and the Néel wall (Fig. 2.3). The Bloch wall has no charges inside the wall and the stray field energy is nearly zero because the magnetic polarization $\boldsymbol{J_s}$ rotates in the plane parallel to the wall plane. In the Néel wall geometries $\boldsymbol{J_s}$ rotates in the plane of the specimen and not in the wall plane. The total energy of the two wall geometries depend on the dimension of the specimen. For a bulk specimen (specimen dimension >> domain wall thickness) the Bloch wall is approximately stray field free (there exists only a small stray field at the surface). For a thin film sample (specimen dimension << domain wall thickness) the Néel wall is approximately stray field free (there exists only a small stray field in the volume).

The wall thickness δ and energy γ are given for the 180º stray field free wall

$$\delta = \pi\sqrt{\frac{A}{K_1}} \qquad \text{and} \quad \gamma = 4\sqrt{AK_1} \tag{2.13}$$

and for the wall with non-vanishing stray field

$$\delta = \pi\sqrt{\frac{A}{K_1 + J_s^2/(2\mu_0)}} \qquad \text{and} \quad \gamma = 4\sqrt{A(K_1 + \frac{J_s^2}{2\mu_0})} \quad . \tag{2.14}$$

When an external field is applied, the magnetization of the multi-domain particle increases due to domain wall movement and rotation of the magnetization in each domain. According to Fig. 2.4 at the initial state the domain wall movement is reversible and J increases linearly with the

field. With increasing field, domains with magnetization oriented in field direction become larger and the domain wall movement is irreversible. At larger fields, the magnetization process is dominated by the rotation of the spontaneous polarization $\boldsymbol{J_s}$ in the domains. In this region a rather large increase in field is required to produce a small increase of polarization J.

During the demagnetization process, the domain wall motion and rotation mechanism may also occur, however, the wall movement can be hindered by pinning at various lattice defects or phase boundaries. The impedance of wall motion requires an additional energy to be overcome, and results in hysteresis loops with large coercivities.

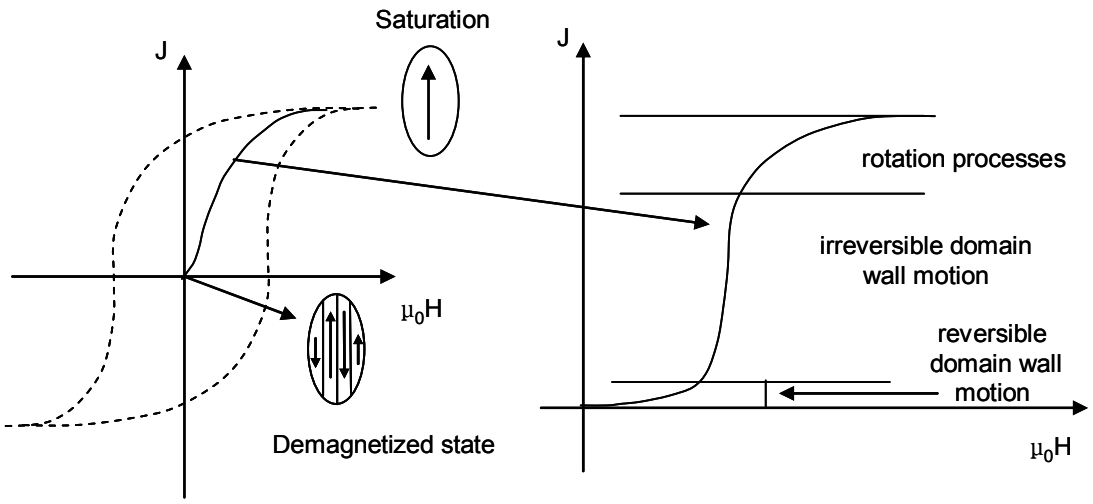

Fig.2.4 Magnetization processes in a multi-domain particle.

2.5 Magnetization processes in a single-domain particle

As long as the energy needed to create a domain wall exceeds the stray field energy saved when the single-domain state transforms into the multidomain state the single domain state is favored in a particle. The critical radius at which a single-domain spherical particle transformes into a multidomain one is given by [23]

$$r_{crit.} = 9\mu_0 \frac{\gamma_B}{J_S^2} \tag{2-15}$$

, where γ_B is the domain wall energy, $\gamma_B = 4\sqrt{AK_1}$.

When the external field is parallel to the easy axis of a single domain particle with uniaxial anisotropy, the hysteresis loop has an exact rectangular shape (Fig. 2.2). The magnetization reversal of this single domain can take place by three different nucleation modes, i.e. the homogeneous rotation, the curling and the buckling. The value of nucleation field varies with the modes and is dependent on the size of the particle. Fig. 2.5 shows the nucleation modes in a single domain particle in the case of an infinite cylinder.

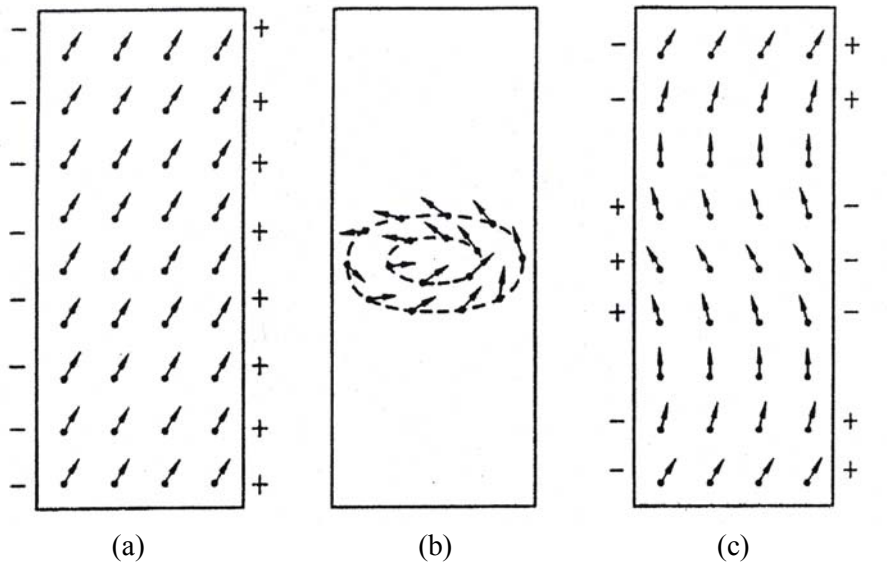

Fig 2.5 Nucleation modes of a single domain particle with the shape of an infinite cylinder:
(a) Coherent rotation mode (b) Curling mode and (c) Buckling mode [24].

In the case of the ellipsoidal particle, the nucleation field can be calculated from the linearized micromagnetic equation resulting from the variation of the magnetic fee energy.
The nucleation field of the homogeneous rotation is given by [19, 24]

$$H_N = \frac{2K_1}{J_s} - (N_{//} - N_{\perp})\frac{J_s}{\mu_0} \quad , \qquad (\Phi_A = 0 \ , \ \Phi_S \neq 0) \ . \tag{2.16}$$

For the curling modes, the nucleation field is given by

$$H_N = \frac{2K_1}{J_S} - N_{//}\frac{J_S}{\mu_0} + 2\pi k\frac{A}{R^2 J_S} \quad , \qquad (\Phi_A \neq 0 \ , \ \Phi_S = 0) \ . \tag{2.17}$$

Here the value of k is a geometric factor and amounts 1.08 for an infinite cylinder, and 1.38 for a sphere. The nucleation field for the curling mode is dependent on the particle radius R, whereas

the nucleation field for the homogenous rotation mode does not. With decreasing particle size, the nucleation field of the curling mode is always greater than that of the homogeneous rotation mode. Thus for small particles, the homogeneous rotation mode is dominant.

2.6 Coercivity mechanism

The coercivity of a permanent magnet is a measure of the energy barrier to be overcome by applying a magnetic field in order to reverse the magnetization of the magnet. From the linearized micromagnetic equations, the coercive field of an ideal ellipsoidal particle can be calculated as [25, 26]

$$H_N = \frac{2K_1}{J_s} - (N_{//} - N_{\perp})\frac{J_s}{\mu_0} \quad . \tag{2.18}$$

However, in real magnetic materials, the coercive field deviates by a factor of 4 ~ 5 from the prediction of eq (2.18) (Brown's paradox). The reason for this discrepancy is the real microstructure of a magnet. Taking into account the microstructural effects, the coercive field can be rewritten by the following global formula

$$\mu_0 H_C = \mu_0 \frac{2K_1}{J_s}\alpha - N_{eff} J_s \, . \tag{2.19}$$

Here α is the microstructural parameter which gives information about the microstructure modifying the ideal nucleation field. The shape of particles, such as sharp corners which generate strong demagnetization fields, also affects the coercivity of real magnets. The shape effect is characterized by the effective demagnetization factor N_{eff}.

There exist in principle two different mechanisms which are the reason for large coercivities, nucleation and domain wall pinning. In the nucleation model, the reversal of a saturated magnet is initiated at grain boundaries and at the coercivity the magnetization switches irreversibly into the other direction. On the other hand, in the domain wall pinning model the large coercivities arise from domain walls which are pinned at pinning sites until the coercivity is reached. In the two coercivity mechanisms, the microstructural parameter α has a different meaning.

2.6.1. Nucleation model

The nucleation at the grain boundaries is initiated by misoriented grains, magnetically inhomogeneous regions in grain boundaries, and exchange coupling between grains. This reduces the energy barrier for the magnetization reversal and makes the coercive field smaller than the ideal nucleation field. In the case of the nucleation mechanism, the microstrucrural parameter α can be expanded by $\alpha = \alpha_\psi \alpha_K \alpha_{ex}$.

2.6.1.1 Effects of misoriented grains, α_ψ

When an oblique magnetic field is applied to an ellipsoidal particle in the single domain state, the nucleation field H_N has been calculated for the condition $|K_1| > |2K_2|$ as follows [27]

$$H_N(\psi_0) = \frac{1}{\{(\cos\psi_0)^{\frac{2}{3}} + (\sin\psi_0)^{\frac{2}{3}}\}^{\frac{3}{2}}} \left[1 + \frac{2K_2}{K_1 + (N_{//} - N_\perp)\frac{J_S^2}{2\mu_0}} \frac{(\tan\psi_0)^{\frac{2}{3}}}{1 + (\tan\psi_0)^{\frac{2}{3}}} \right] \cdot H_N(0)$$

$$= \alpha_\psi H_N(0) \ . \qquad (2.20)$$

ψ_0 is the oblique angle between the easy axis and the direction of the applied field, and $H_N(0)$ is the nucleation field obtained when the field is applied along the easy axis. The microstructural parameter α_ψ decreases the nucleation field, and is a function of the angle ψ_0. It has a minimum value for $\psi_0 = \pi/4$, leading to the minimum nucleation field $H_N^{\min}$. For Nd-Fe-B, and Pr-Fe-B magnets, the angular dependence of α_ψ is shown in Fig. 2.7.

For an assembly of uniaxial spherical particles ($N_{//} = N_\perp = 1/3$) which are randomly oriented, $H_N^{\min}$ is given by [28]

$$H_N^{\min} = \frac{1}{2\sqrt{2}J_S}\left[K_1 + \frac{K_2}{4}(W - \frac{K_1}{K_2} + 3)\right]\sqrt{W(\frac{K_1}{K_2}+1) - (\frac{K_1}{K_2})^2 - \frac{2K_1}{K_2} + 3}, \qquad (2.21)$$

with $W = \pm\sqrt{(\frac{K_1}{K_2}+1)^2 + 8}$.

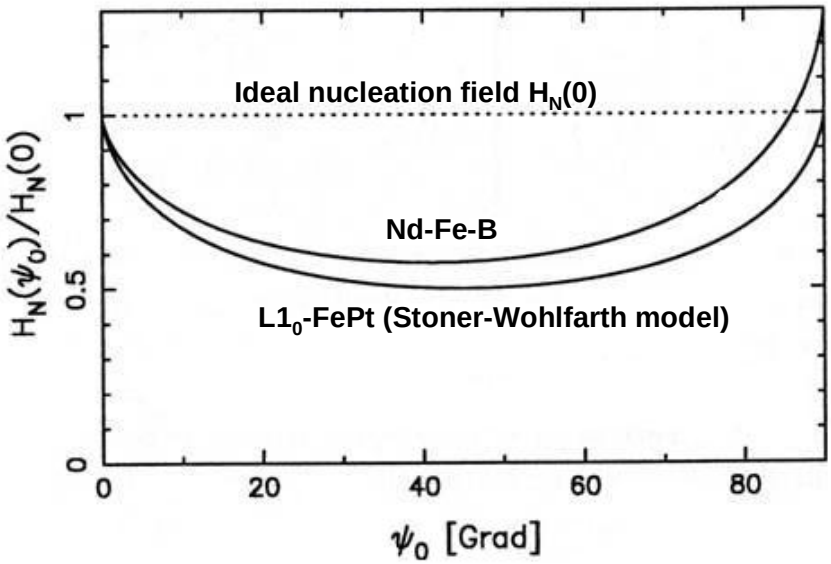

Fig. 2.6 Angular dependence of the microstructural parameter α_ψ for a spherical Pr_2FeB and $Nd_2Fe_{14}B$ single-domain particles as a function of the misorientiation angle ψ_0 [27].

Here the + sign holds for $K_2 > 0$, $K_1 > -2K_2$ and the – sign for $K_2 < 0$, $K_1 > 0$.

If the K_2 value is small enough to satisfy the condition $0 < K_2 < 1/4K_1$, $H_N^{\min}$ is approximately given by

$$H_N^{\min} \cong \frac{K_1 + K_2}{J_s} \cong \frac{K_1}{J_s} \ . \qquad (2.22)$$

Therefore, the reduced coercive field of an isotropic magnet can be evaluated quantitatively by eq. (2.22).

2.6.1.2 Effect of inhomogeneous grain boundaries, α_K

If the intrinsic magnetic properties (J_s, K_1) of a grain boundary differ from those of the grain inside, the nucleation field will also deviate from the ideal value. For a special case of a planar soft magnetic grain boundary of width $2r_0$ the nucleation field and the microstructural parameter α_K has been analytically treated by Kronmüller [25]. Fig. 2.8 shows the schematic model of the soft magnetic planar nucleus. The variation of the anisotropy constant K_1 is given by

$$K_1(z) = K_1(\infty) - \frac{\Delta K}{\cosh^2(\frac{z}{r_0})} \tag{2.23}$$

with $K_1(\infty) = K_1$ for $|z| > r_0$, and ΔK is the anisotropy constant in the grain boundary region. From this relation the nucleation field is obtained as

$$H_N = \frac{2K_1(\infty)}{J_s}\alpha_K - N_{eff}J_s \tag{2.24}$$

with

$$\alpha_K = 1 - \frac{1}{4\pi^2}\frac{\delta_B^2}{r_0^2}\left[1 - \sqrt{1 + \frac{4\Delta K r_0^2}{A}}\right]^2 , \tag{2-25}$$

where δ_B is the domain wall width. With the assumption that grain boundaries are very narrow ($r_0 < \delta_B$) and $\Delta K \approx K_1$, the value of α_K is unity resulting in the ideal nucleation field including stray field term.

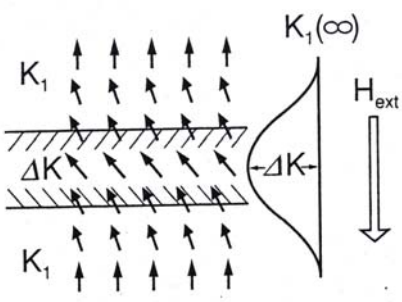

Fig.2.7 The nucleation model for a soft magnetic planar grain boundary of width $2r_0$ between hard magnetic grains [29].

2.6.1.3 Effect of exchange coupling between grains, α_{ex}

By the microstructural parameter α_{ex} the cooperative magnetization reversal process of exchange coupled grains in polycrystalline magnets can be analyzed. By exchange coupling between neighboring grains the coercive field is further reduced. α_{ex} can be evaluated to $\alpha_{ex} \approx 0.5$.

2.6.2 Domain wall pinning model

The domain wall pinning is caused by magnetically inhomogeneous regions in grains which anchor walls not to pass freely. For effective pinning planar defects are required. If the anisotropy potential of the defects differs from their surrounding, the defects interact with moving domain walls. This may increase the coercivity compared to the ideal nucleation field. In this case the microstructural parameter from the wall pinning effect is greater than unity [30].

2.7 Approach to the saturation

Experimentally the magnetization behavior at high magnetic fields (in the first quadrant of hysteresis loop) can be described by

$$J(H) = J_s - \sum_i \frac{a_{\frac{i}{2}}}{H^{\frac{i}{2}}} \ , \quad i = 1, 2, \ldots\ldots \tag{2.26}$$

Here the $a_{i/2}$ terms result from the intrinsic and extrinsic properties. The intrinsic properties include K_1, J_s and A values and the extrinsic properties result from structural defects. In the case of hard magnetic materials the intrinsic magnetic properties are governing the approach to saturation. The field dependence of *J(H)* can be analytically derived from the micromagnetic equations, and at high magnetic fields $H > 2K_1/J_s$ the angle θ between J_s and H for a uniaxial crystal is obtained as

$$\theta = \frac{K_1 \sin 2\varphi_0}{2K_1 \cos 2\varphi_0 + HJ_s} \ , \tag{2.27}$$

and *J(H)* can be written as

$$J(H) = J_s \left(1 - \frac{1}{2} \left(\frac{K_1 \sin 2\varphi_0}{2K_1 \cos 2\varphi_0 + HJ_s} \right)^2 \right) \tag{2.28}$$

For the condition of $H \to \infty$, J(H) is reduced to [31-33]

$$J(H) = J_s \left(1 - \frac{4}{15} \frac{K_1^2}{J_s^2} \frac{1}{H^2}\right) \ . \tag{2.29}$$

By fitting the experimental hysteresis loop to this relation, the intrinsic material parameters of J_s and K_1 can be obtained.

3. Magnetic recording media

By magnetic recording information or data is stored through the magnetization orientation of magnetic particles. A magnetic recording facility includes the magnetic storage media and heads to write and read the data. The recording medium is made of a (middle) hard magnetic material with a coercivity up to 0.2 T. For writing data a magnetic field can be induced by an electric recording signal. Then data is stored in form of a magnetization pattern. Afterwards, the written magnetic pattern is moved across the poles of the reading head, where a voltage is induced by the stray field of the magnetization. This voltage is amplified and reproduces the recorded information.

3.1 Areal density and superparamagnetism

Currently, data storage is of digital type. The most important question in developing new recording media is how to increase the areal storage density, i.e the number of bits per inch^2. This density has doubled every 1~2 years since 1960, and a modern hard disk drive has a recording density over 100 Gbit/inch^2 [34, 35] (Fig. 3.1). In order to realize higher recording densities recording media with smaller particles are required. However, there exists a limit below which the particle size should not be reduced (superparamagnetic limit) [2]. Superparamagnetism is a phenomenon by which a small ferromagnetic particle loses its spontaneous ferromagnetic ordering even below the Curie temperature. This is caused by the fact that the energy required to rotate the spontaneous polarization of the particle is comparable to the thermal fluctuation energy at ambient temperatures. In the absence of external fields, the energy barrier for magnetization reversal of a single-domain particle is determined by the magnetocrystalline anisotropy and the volume of the particle [36]

$$\Delta E \propto K_1 \cdot V \quad . \tag{3.1}$$

For very small particle volumes, the energy barrier is small enough to be overcome by thermal fluctuations. This leads to the loss of coercivity of the magnetic medium and therefore of the recorded data. For an effective decrease of the bit size while maintaining long term stability against thermal fluctuations, a large magnetic anisotropy constant is required. However, a larger K_1 value will make it very difficult to record a bit by conventional field strengths of the writing

head. Therefore, the choice of materials with appropriate magnetic properties is substantial for manufacturing high density magnetic recording media.

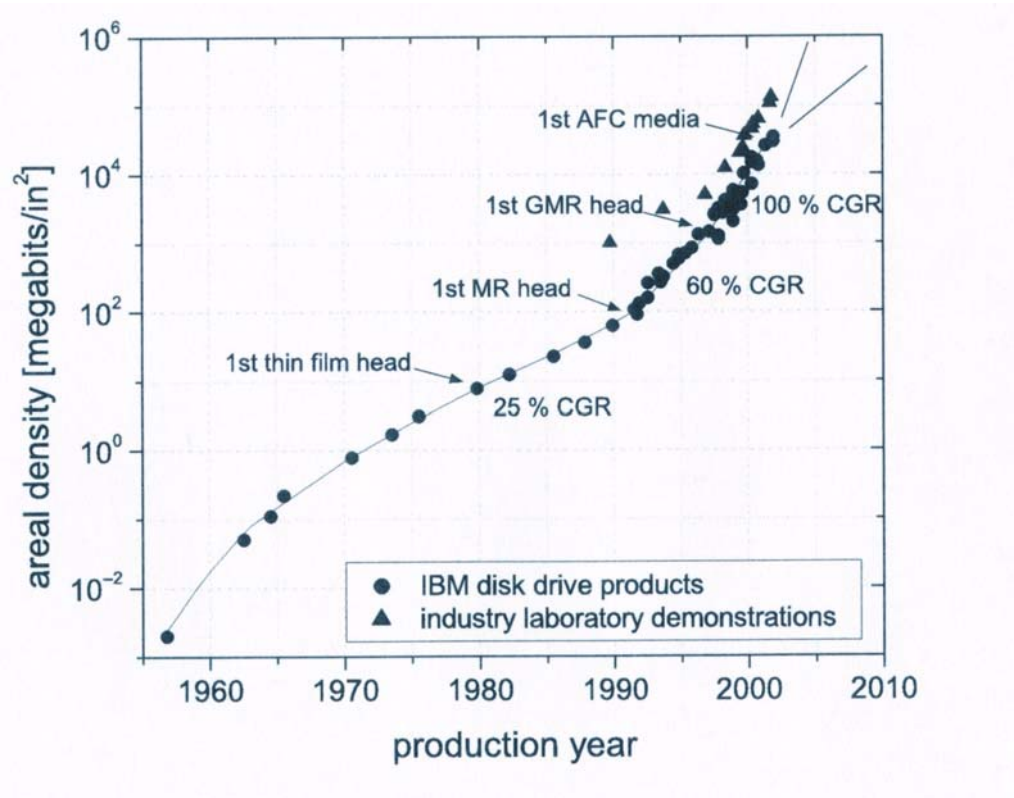

Fig. 3.1 Progress of the areal density of recorded data in magnetic recoding media [37].

3.2. Types of recording media

In addition to the magnetic properties of magnetic materials, the way to write a bit is also important to realize high recording densities. In general bits can be written with magnetization orientation parallel (longitudinal magnetic recording) or perpendicular (perpendicular magnetic recording) to the media plane (Fig. 3.2).

For increasing the areal density, perpendicular recording has been proposed as an alternative to the conventional longitudinal recording [38]. A fundamental advantage of perpendicular recording over longitudinal recording is the magnetostatically stabilized bit-pattern for high areal densities.

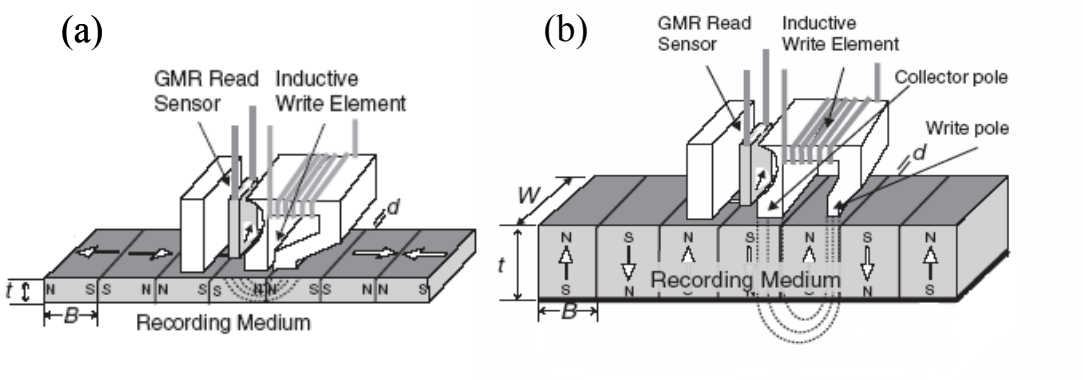

Fig. 3.2 Schematic views of (a) longitudinal and (b) perpendicular magnetic recording [37].

In perpendicular recording the bit structure is more stable thatn in longitudinal recording. Therefore, the thermal stability of the magnetization in perpendicular recording is much better than in longitudinal recording [3]. Furthermore the digital recording pattern in the case of perpendicular media shows sharp and low-noise transitions, whereas in the case of longitudinal media zigzag noisy structures occur. Thus much more information per unit area can be stored effectively in a perpendicular medium than in a longitudinal one.

3.2.1 Longitudinal recording media

For longitudinal magnetic recording, a single magnetic storage layer is used such as a thin film of CoPtCrX (X = B, Ta). The film is grown on top of a complex underlayer structure used for forming proper crystallographic orientation and grain size distribution. A thin carbon overcoat layer is required to protect the medium from oxidation and physical damage in the case of a contacting head. An optimal longitudinal medium is composed of small isolated grains with narrow grain size distribution, and good in-plane crystallographic texture. The isolation is due to a chemical segregation of grain boundaries. Due to the thermal fluctuations the grain size in the medium cannot be smaller than about 50 nm [39, 40].

To improve the thermal stability of longitudinal recording media, antiferromagnetically coupled media (AFC media) have been suggested [41]. In these media, two ferromagnetic layers are coupled antiferromagnetically through a non-ferromagnetic layer.

Whereas in a single layer magnetic recording medium, the energy barrier for magnetization reversal of a written bit can be reduced by the demagnetization field of a neighboring bit, in AFC medium the exchange coupling between two ferromagnetic layers reduces the demagnetization

field and therefore enhances the stability of the recording bit. Fig. 3.3 represents a schematic view of an AFC film.

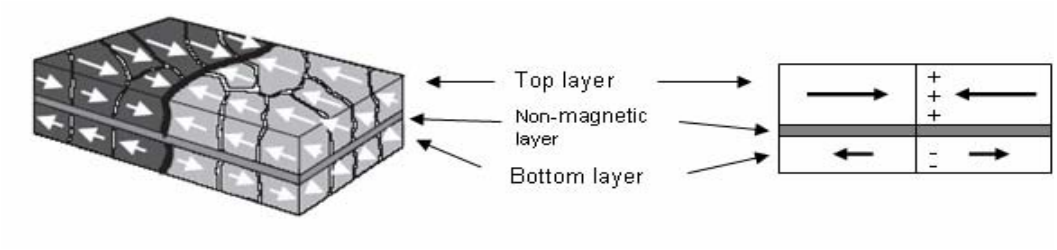

Fig. 3.3 Schematic representation of a longitudinal AFC media [37].

3.2.2 Perpendicular recording media

In perpendicular magnetic recording the easy axis of the magnetic layer is perpendicular to the film plane. The basic requirements for an applicable perpendicular recording medium are grains with uniaxial anisotropy perpendicular to the film plane resulting in large coercivity and large remanences equal to the saturation polarization and therefore in hysteresis loops of great squareness. This ensures a large stability of the recorded bits and a proper reading of the stored data. In the case of conventional thin films the shape anisotropy is dominant and magnetization perpendicular to the film plane is harder than that parallel to the film due to the large demagnetization field in the perpendicular direction. Thus a material proposed as a perpendicular medium should have another anisotropy source by which it can overcome the large magnetostatic energy along the perpendicular direction. In the case of grains with uniaxial axis perpendicular to the film plane the magnetization in the bit will not switch for decades unless an external magnetic field is applied by the writing head.

For perpendicular recording, three types of thin film media are suggested, i.e. multilayer [42-44], Co-Cr-Pt-X (hcp structure) [45] and FePt or CoPt media with $L1_0$ structure [46, 47].

Each of them has a perpendicular uniaxial anisotropy. Fig. 3.4 shows the cross section of the three types of perpendicular media.

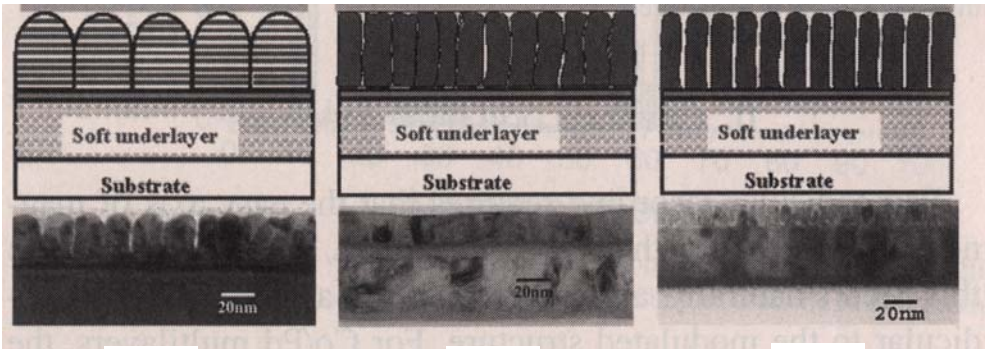

(a) **(b)** **(c)**

Fig. 3.4 Cross section microstructures of three different types of perpendicular media: (a) Multilayer media (Co/Pd), (b) CoCrPt alloy media and (c) $L1_0$ granular alloy media (FePt, or CoPt) [48].

The multilayer films are composed of magnetic Co layers which are alternating with layers of non-magnetic transition metals such as Pd or Pt. Due to the interfacial anisotropy, Co/Pt and Co/Pd multilayers exhibit uniaxial anisotropies of 0.65 - 0.85 MJ/m^3, resulting in coercivities in perpendicular direction up to 0.7 ~ 0.8 T [49]. By adding additional Pd or Pt layers leading to a repeating sequence of Co/Pt/Pd/Pt, the anisotropy becomes larger. However, using such multilayer films the hysteresis loops lose a little of their squareness. This is caused by exchange interaction between columnar grains in the multilayer films and generates the undesirable recording noise.

The CoCrPt-X alloys have the origin of their large anisotropy in their typical hcp structure with uniaxial *c*-axis. The elemental Cr in these alloys segregates at grain boundaries and weakens the intergranular exchange interaction. For CoCrPtTa alloys a coercivity of 2.6 kOe and a squareness of 0.98 are reported [50]. The coercivity values of CoCrPt-X alloys in general are below 3 kOe which may not lead to larger storage densities than 50 $Gbit/inch^2$. Since the coercivity of Co alloys depends on the anisotropy energy due to the structural arrangement of magnetic Co atoms, heat treatment with Cr as additives results only in microstructural changes such as large grain sizes or a change of the composition of the grain boundary [51, 52]. Thus the coercivity can be increased only by adding other elements to make a chemical bonding with Co.

In contrast to the hcp Co alloys, chemically ordered alloys (e.g. $L1_0$-FePt and $L1_0$-CoPt) have a large uniaxial anisotropy by themselves that induces a high coercivity. The continuous FePt films deposited on MgO substrates were reported to have a coercivity of 5 kOe [47]. As the phase transformation from the chemically disordered to the ordered phase requires high temperatures

over 700 ºC, thin films deposited at low temperatures do not have the ordered $L1_0$-structure. Consequently, these films should be deposited at high temperatures or, annealed after deposition. The high temperature process may induce the formation of large grains which lead to a deterioration of the magnetic properties.

There are still open questions concerning the phase transformation to the ordered $L1_0$-phase as well as the intrinsic magnetic properties and the magnetization behavior of ordered $L1_0$ alloys. As the Fe-Pt system has been found to be a promising candidate for ultra-high density data storage it will be used in this thesis to answer the open questions.

4. $L1_0$-FePt and $L1_0$-FePd alloys

4.1 FePt alloy

4.1.1 Crystal structure

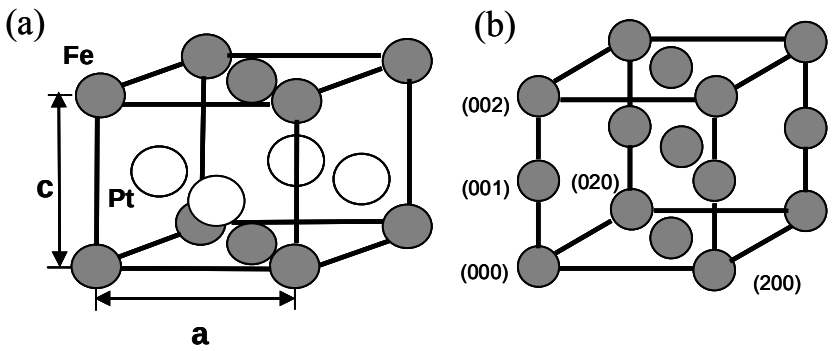

Fig. 4.1 The unit cell (a) and reciprocal lattice (b) of $L1_0$ FePt.

The crystal structure of the $L1_0$-FePt phase is presented in Fig. 4.1. A four-fold rotational symmetry is existing along the [001] axis. Accordingly, the alloy has a tetragonal unit cell, in which the Fe and Pt atoms occupy alternating (002) planes. The segregation of Fe and Pt atoms in alternating (002) planes causes the *c*-axis in the unit cell to be distinct from the *a*-axis, since the sizes of Fe and Pt atoms differ from each other. Due to the periodic arrangement of Fe and Pt atoms in the $L1_0$-phase, this alloy phase is called an ordered alloy and its lattice is called superlattice. In a reciprocal lattice space, ordered alloys have points with (001) index (Fig. 4.1b). The (001) index is unique in the reciprocal lattice of the ordered $L1_0$-phase, and does not occur in the cubic structure. The lattice constants in the tetragonal unit cell are a = 3.852 Å and c = 3.716 Å.

4.1.2 Phase diagram

The ordered $L1_0$-FePt alloy is formed by a disorder-order transformation. In the Fe-Pt binary phase diagram (Fig. 4.2) the transformation occurs at 1300 ºC. Although the ordered $L1_0$-FePt alloy is stable at low temperatures, the rate at which ordering occurs is so slow that it is impossible to prepare an ordered FePt alloy by processing at room temperature. Normally bulk $L1_0$-FePt can be obtained by preparing solution and subsequent annealing. The elemental mixture of a desired composition is heated above the disorder-order transformation temperature,

and then quenched to low temperature to achieve a solid solution. This solid solution alloy has to be annealed at elevated temperatures to induce long range atomic ordering.

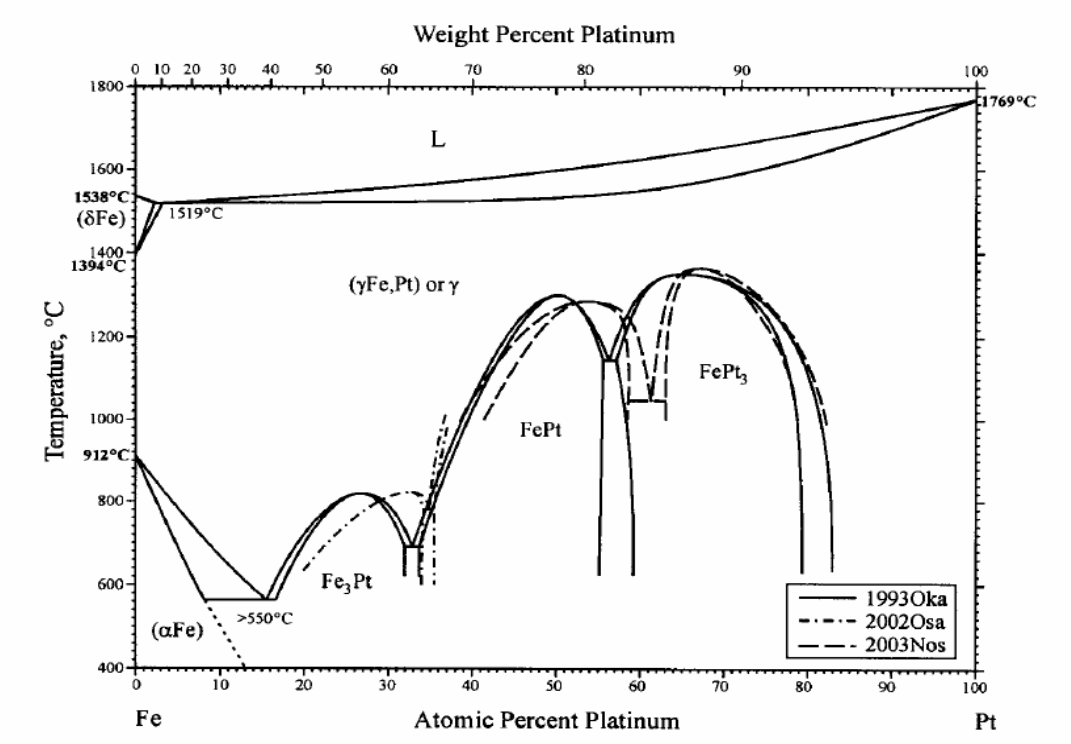

Fig. 4.2 Equilibrium phase diagram of the Fe-Pt system [53]

In the case of $L1_0$-FePt thin films, the solid solution phase is directly made during the film deposition process. The subsequent annealing is required for ordering. During the annealing process, grain growth and coalescence in the ordered phase may occur both degrading the magnetic properties of the film.

The degree of ordering in the alloy can be quantified by the ordering parameter *S*, which is given by

$$S = \frac{r_A - X_A}{1 - X_A} = \frac{r_B - X_B}{1 - X_B} \quad , \tag{4.1}$$

where X_A is the mole fraction of element A in the alloy and r_A is the probability that an A sublattice site is occupied by an A atom. The value of *S* is unity for a fully ordered alloy and becomes zero for a completely random distribution. The ordering parameter can be determined by analyzing the X-ray diffraction (XRD) spectra, which is described in Chapter 6.2.

4.1.3 Intrinsic magnetic properties

The ordered $L1_0$-FePt alloys have large magnetocrystalline anisotropy based on the large spin-orbit coupling in 5d electrons, and therefore are paid much attention for the application in ultra-high density magnetic recording media, or micro-electromechanical system (MEMS). Another advantage of these alloys is that they are chemically robust and oxidation-resistant. Table 4.1 summarizes the intrinsic magnetic properties of FePt and provides a comparison to other magnetic materials.

phase	symmetry	T_C [K]	J_s [T]	$\mu_0 H_A$ [T]	δ [nm]	D_c [nm]
Co	hexagonal	1390	1.81	0.76	14	68
CoPt	tetragonal	720	1.00	12.3	7.4	1000
FePt	tetragonal	750	1.43	11.5	6.3	560
FePd	tetragonal	760	1.39	3.5	11.5	330
Sm_2Co_{17}	rhombohedral	1190	1.22	6.5	8.6	490
$SmCo_5$	hexagonal	1020	1.07	39	3.6	1530
$Nd_2Fe_{14}B$	tetragonal	585	1.61	7.6	3.9	214

Table 4.1 Intrinsic magnetic properties of different magnetic materials (T_C: Curie temperature, J_s: spontaneous polarization, $\mu_0 H_A$: anisotropy field, δ : domain wall width, D_c : single-domain particle diameter) [54].

4.1.4 Thin films

4.1.4.1 Alignment of the tetragonal *c*-axis

For application of $L1_0$-FePt as magnetic recording media, the easy magnetization axis (tetragonal *c*-axis) needs to be aligned parallel or perpendicular to the film plane in a controlled way. By choosing a proper seed layer and substrate such as Pt and MgO single crystal, it is possible to control the *c*-axis to lie perpendicular or parallel to the film plane. Results from R. Farrow [6] indicate that the orientation of *c*-axis in epitaxially grown films is in-plane for a MgO (110) seed layer and out of plane for MgO (002). On the other hand, D.J Sellmyer [9, 13] showed that in nonepitaxial $L1_0$-films, the texture evolution during the annealing process is dependent on the composition and thickness of the films. By varying the composition of the films the lattice

parameters of the ordered tetragonal unit cell are modified. The film thickness and the lattice parameters have influence on the evolution of stress in thin films.
In order to control the *c*-axis of $L1_0$-FePt films, the selection of substrate, film composition, and film thickness are considered as controlling factors to reduce stresses during phase transformation from the disordered to the ordered state.

4.1.4.2 Enhanced coercivity by grain isolation

As shown by the eq. (2.19), the nucleation field of a magnetic particle assembly is decreased by exchange coupling between adjacent grains. If the grains in $L1_0$-FePt films are isolated from each other without any exchange coupling, magnetization reversal takes place by coherent rotation. Moreover, when the tetragonal easy axes are aligned in field direction, the coercivity will reach the ideal nucleation field of $2K_1/J_s$ in case of spherical particles. T. Shima et. al [55] have reported that $L1_0$-FePt films composed of single domain particles have coercivities of 7 T at room temperature. The films were deposited using dc sputtering with codeposition of Fe and Pt directly onto heated MgO (001) substrates. They observed a remarkable change in the film morphology with increasing film thickness. When the film thickness was larger than 45 nm, the film structure changed from isolated particles to a continuous morphology. It was suggested that in a deposition process for ultra-thin films, the island growth mode (Volmer-Weber mode) [56] is dominant and a particulate film is formed. However, due to the sluggish atomic mobility of Pt atoms the continuous film is obtained at low temperature. High temperatures over 700 ºC are required for $L1_0$-FePt films composed of isolated particles.
Another method to isolate grains is to add elements such as Au and Ag. Then the film structure changes from an interconnected network to completely isolated grains. It is reported [57] that the effect of Ag is greater than that of Au on grain isolation and coercivity enhancement. The coercivity of $(FePt)_{90}Ag_{10}$ film was found to be 2.5 T. In case of Ag and Au addition the isolated particle structure can be formed already at 520 ºC.

4.1.4.3 Coercivity mechanism

The coercivity of permanent magnets is generally due to two different mechanisms, nucleation and pinning as mentioned in Chapter 2.6. In case of particulate $L1_0$-FePt films, it was suggested that the high coercivities are resulting from the nucleation mechanism [58]. The epitaxially

grown particulate films were composed of single crystalline nanoparticles with no structural defects such as twins and grain boundaries inside the particles. After saturation, nucleation occurs at very large fields. Fig. 4.5 shows the hysteresis loops of a particulate $L1_0$-FePt film, in which the initial magnetization curve indicates a nucleation type behavior.

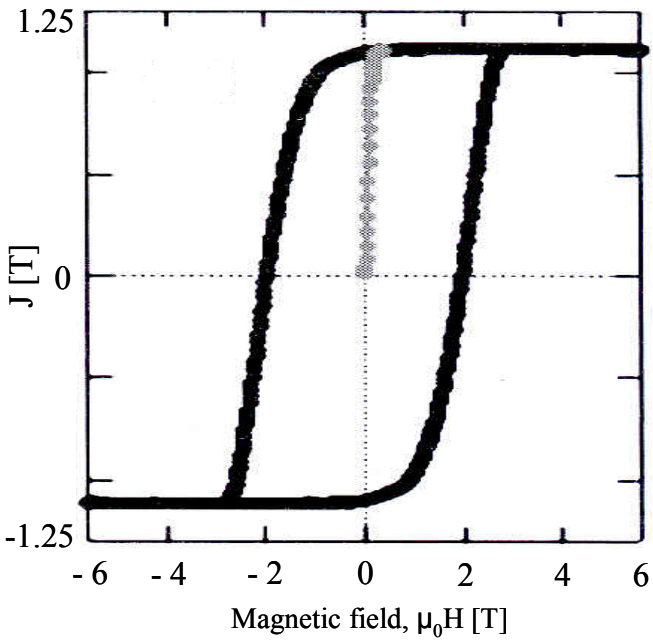

Fig. 4.3 Magnetization curve of a granular $L1_0$-FePt film with nominal thickness of 25 nm. The film was deposited onto heated MgO (001) single crystal substrates [58].

On the other hand, for the expitaxially grown continuous film on a Pt (001) buffer layer, the domain wall pinning mechanism was reported [59, 60]. Because of the lattice mismatch between substrate and film, tensile epitaxial strains occurred and were relaxed by the formation of microtwins. The domain walls in the continuous film may interact with these microtwins and were trapped along twin surfaces oriented to <110> directions. It was observed that confined bubble domains did not propagate further. Fig. 4.4 shows the confined bubble domains with rectangular regions of the microtwin surfaces.

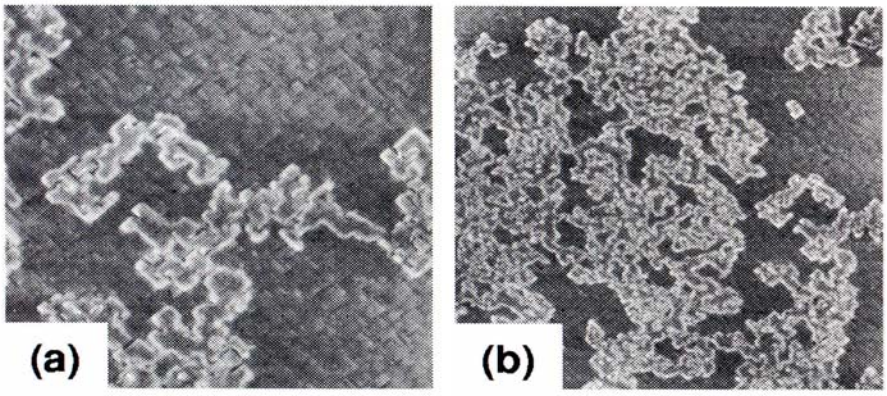

Fig. 4.4 (a) 8 μm × 8 μm , (b) 16 μm × 16 μm images obtained by Magnetic Force Microscopy (MFM). The images were taken in a partially reversed magnetization state ($J./J_s$ = 0.84). The white boundaries correspond to the magnetic domain walls.

4.2 FePd alloy

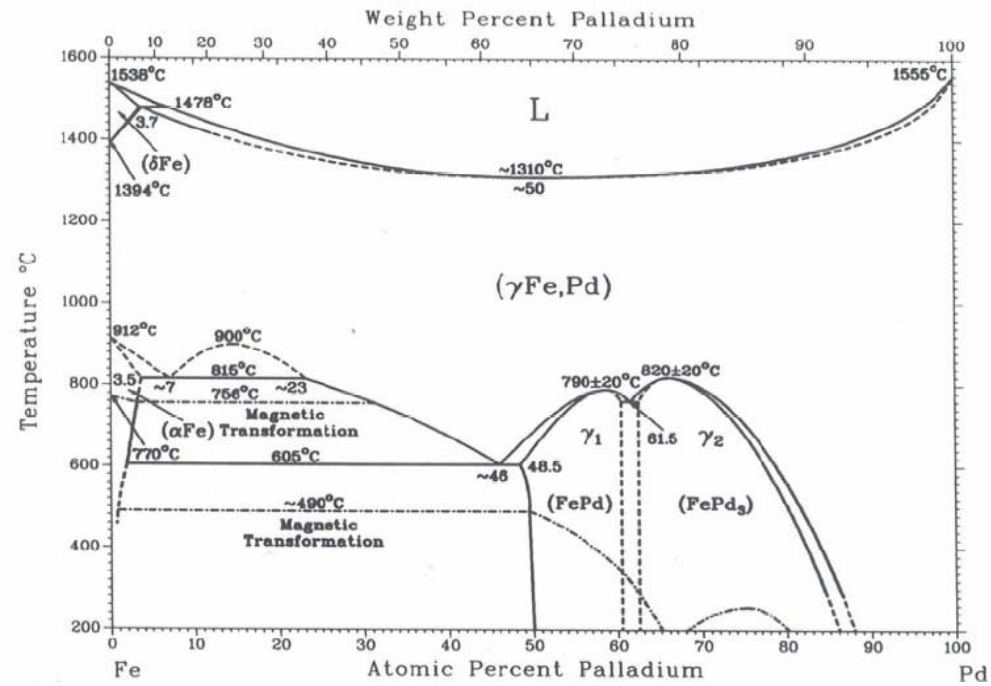

Fig. 4.5 Equilibrium phase diagram of the Fe-Pd system [53].

Fig. 4.5 shows the binary phase diagram of the Fe-Pd system. Similar to the Fe-Pt system, a disorder-order phase transformation occurs at 700º C, which is a lower temperature compared to the FePt system. The FePd ordered alloy shows also the $L1_0$ tetragonal structure. The lattice

constants are a = 3.852 Å and c = 3.723 Å. The tetragonal distortion causes the uniaxial anisotropy as in the case of the $L1_0$-FePt. However, the anisotropy constant and resulting coercivity are lower than those of the $L1_0$-FePt alloy (Table 4.1).

5. Experimental methods

5.1 Ion beam sputtering

The $L1_0$-FePt and $L1_0$-FePd films were prepared by heat-treating multilayer precursors which were composed of very thin elemental Fe and Pt, or Fe and Pd layers, respectively. The idea of synthesizing the $L1_0$-phase from multilayers stems from the fact that alternating layers of Fe/Pt and Fe/Pd multilayer films imitate the crystal structure of the $L1_0$-phase alloy, which has a face-centered-tetragonal (fct) unit cell composed of parallel Fe and Pt/Pd atomic planes perpendicular to the *c*-axis. The common difficulties in growing films of the $L1_0$-phase are high transformation temperatures, and the alignment of the crystallographic *c*-axes of the individual grains. By introducing the multilayer precursor, it is expected to reduce the annealing temperature, and align the *c*-axes more easily. The multilayer precursors were deposited by ion beam sputtering using a radio frequency plasma ion source.

The ion beam sputtering process is based on the bombardment of a selected target material by an ion beam having sufficient energy to remove surface atoms from the target. A film of the desired material was formed in vacuum atmosphere by collecting the ejected atoms on the surface of a substrate. Following aspects of our ion beam sputtering are different from other sputtering processes [61, 62]:

1) The directionality of the beam allows a precise control of the incidence angle of the beam on the target, and the deposition angle on the substrate.
2) Beams with narrow energy band can be used to study the sputter yield and deposition process in dependence of the ion energy.
3) Four Targets can be mounted on a cubic target holder at the same time.

For ion beam sputtering, firstly, inert gas is injected into the ion gun which is in the glow discharge plasma state. Inert gas ions are generated by collision processes involving charge exchange as well as energy and momentum loss. Then the ions are extracted from the plasma and accelerated towards a target by the voltage on the acceleration grids. The target should be attached to a water-cooled Cu plate to dissipate the heat created by the ion bombardment and to prevent melting or outgassing of the target. The substrate is placed directly opposite to the target.

The process variables for ion beam sputtering are the ion energy, the ion flux and the system pressure. For depositing Fe/Pt multilayers by sputtering, the system base pressure is about 2 ×

10^{-8} torr. In the ion gun, the radio frequency (RF) power generates an Ar plasma and ions are accelerated by focusing optics. The Ar ions are accelerated on the sputter target at 1000 V at an angle of about 45º. The Ar pressure is maintained in the range of 2 ~ 3 × 10^{-4} torr by a flow-controller. Two rectangular targets of Fe and Pt of size 7 cm × 7 cm are mounted on a cube which can be rotated by a stepping motor. The layer thickness is monitored by a quartz-crystal oscillator which is placed near to the substrate. The thickness monitor, the controller for the stepping motor and the beam shutter are all interfaced to a computer. When the multilayer is deposited, the computer sends the material parameters to the thickness monitor, and opens the beam shutter. When the desired thickness is reached, the beam shutter is closed, and the stepping motor is rotated to a new position to take another target. The RF power applied to the ion gun is kept constant during the whole sputtering process. The equipment set up for ion beam sputtering is schematically illustrated in Fig. 5.1.

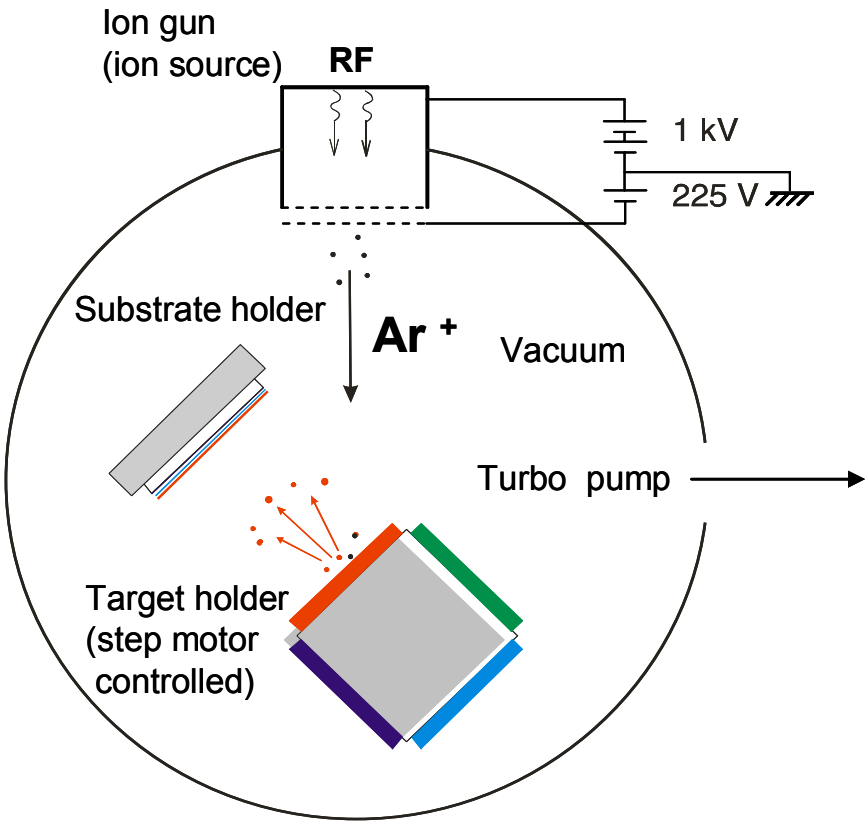

Fig. 5.1 Schematic illustration of ion-beam sputtering.

5.2 Characterization of the microstructure

5.2.1 Bragg X-ray diffractometer

With a X-ray diffractometer of Bragg-Brentano geometry the phases of the film can be analyzed. In the diffractometer essentially monochromatic radiation is used and the detector for measuring the diffracted beam from the specimen is placed on a circle centered on the specimen axis. The diffraction angle θ, the wavelength of the X-ray λ and the distances between lattice planes d are related by the Bragg law

$$n\lambda = 2d\sin\theta . \tag{5.1}$$

By comparing the measured diffraction angles with the reference data [63, 64], the phases of a specimen can be analyzed. A Siemens D-5000 diffractometer with monochromatic Cu-K_α radiation (λ = 1.5406 Å) and a secondary monochrometer to avoid fluorescence from Fe was used for the X-ray diffraction experiments.

5.2.2 Pole figure measurements

The pole figure is a representation of the orientation distribution of a crystal lattice. A pole figure is measured by X-ray diffraction with a special goniometer setup. The goniometer should have rotating 5-axes. Two of them are used to set the Bragg angle choosing a specific crystallographic plane of θ - 2θ. The third axis tilts the specimen plane with respect to the focusing plane. The fourth and fifth axes are to rotate the specimen about its normal and to oscillate the specimen under the beam, respectively (angle φ and ψ in Fig. 5.2). Fig. 5.2 presents the pole figure angles to describe the diffraction geometry.

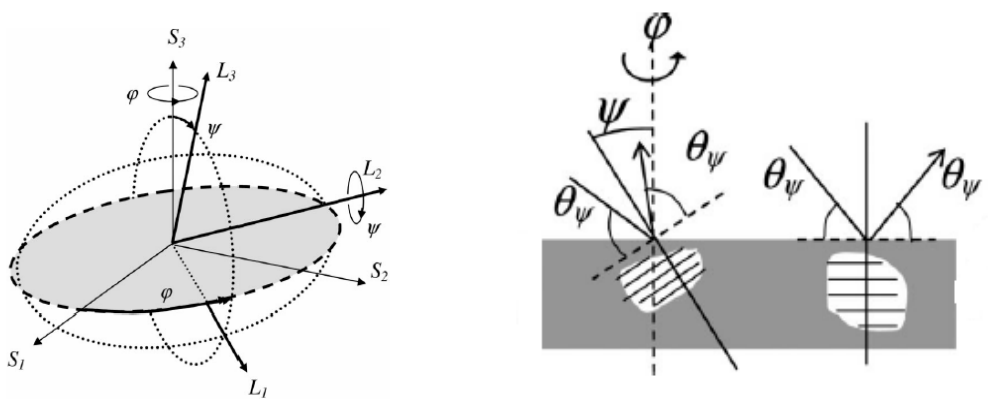

Fig. 5.2 (a) Definition of angles φ and ψ for the pole figure measurements.

(b) Schematic diagram of the grain orientation and the pole figure angles φ and ψ [65].

5.2.3 Transmission electron microscopy (TEM)

A transmission electron microscope (TEM) is used to perform chemical and crystallographic analyses in material sciences.

A conventional TEM is composed of electron gun, magnetic lenses, several apertures, the sample holder, and detectors. The electron gun generates an electron beam with a uniform current density by thermal ejection or field emission. A thin specimen is irradiated by the beam. Some electrons in the beam directly transmit the specimen, others are interacting with atoms of the specimen by scattering, diffraction, and absorption. The interference of these transmitted and interacting beams makes a contrast in the image plane of a TEM. The TEM used for our experiments is a JEOL 4000FX (400 kV) with 1.9 Å resolution, and ARM (Atomic resolution microscopy). The ray diagrams of the microscope are shown in Fig. 5.3.

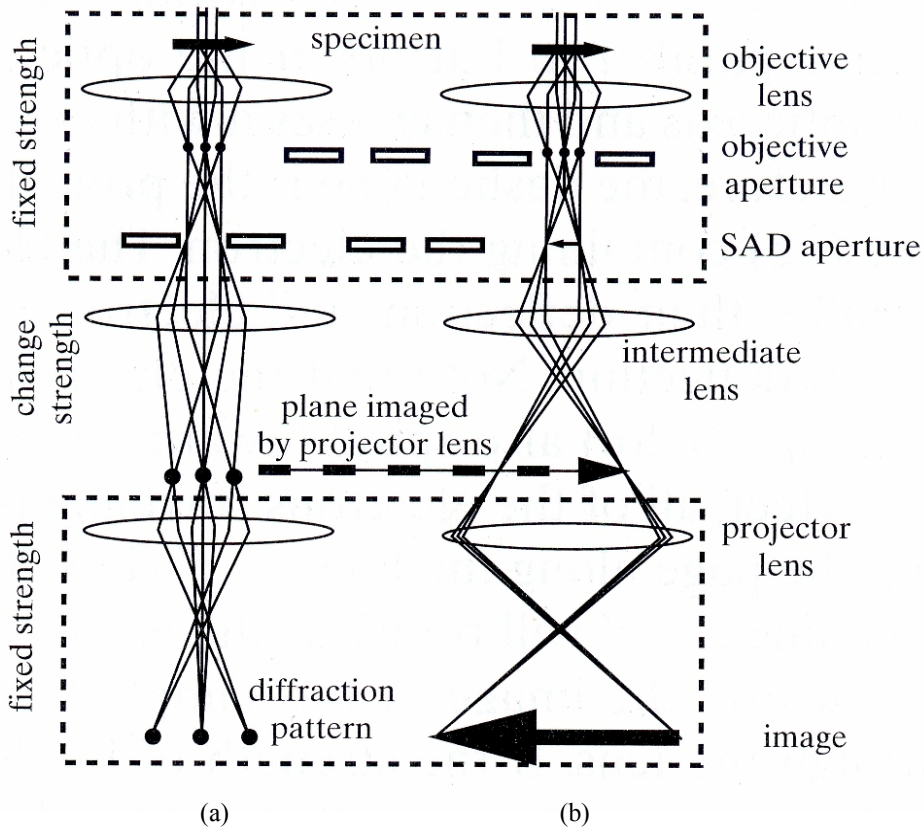

Fig. 5.3 Ray diagram of TEM for (a) the diffraction pattern, (b) imaging the sample [66].

To observe a microstructure in TEM experiments, the imaging and diffraction mode are useful. The imaging mode in which small areas of the specimen are magnified can be carried out by adjusting the object plane of the intermediate lens to the image plane of the objective lens. In the diffraction mode, the intermediate lens is adjusted to focus on the back focal plane of the objective lens, and the back focal plane acts as the object plane for the intermediate lens. One can switch between the imaging and diffraction mode by changing the strength of the intermediate lens.

To investigate the phase transformation mechanism, in-situ TEM experiments are performed. The in-situ TEM (atomic resolution microscope, ARM with accelerating voltage of 1250 KeV) is composed of a heating stage, a temperature controller, a charge-coupled device (CCD) camera and a video tape recording (VTR) system. The static image and motion pictures can be recorded during heating or cooling the specimen.

5.2.3.1. Imaging mode

In the imaging mode there exist three important TEM imaging modes which are the bright-field, the dark-field, and the high-resolution mode (Fig. 5.4). For the bright-field image (BF), the objective aperture is placed on the back focal point of the objective lens so that the diffracted beams are blocked and only transmitted beams are allowed to pass. In this case the thickness variation and scattering difference form the image contrast. Regions of the specimen which are thicker or denser scatter electrons more strongly and appear darker in the image. The difference in crystallographic directions of the specimen grains also makes a contrast in the bright field image. In grains oriented parallel to zone axes a large number of beams are diffracted which makes therefore grains appear dark in the bright-field image.

In the dark-field image the transmitted beam is excluded, and one or more diffracted beams are chosen to form an image contrast by moving the object aperture or by tilting the beam direction. By selecting spots in the diffraction pattern, the dark-field image gives information about the size or shape of specific grains.

The high-resolution image can be obtained using a large size objective aperture. The aperture selects both kinds of beams, the transmitted and the diffracted one. The image is formed by the interference of all beams. If the point resolution of the microscope is high enough and the specimen is aligned along a zone axis, the lattice images of the specimen are visible. The

HRTEM method is used for analyzing complex microstructures on an atomic scale such as phase-interfaces, oxide films, and multilayer films.

5.2.3.2 Diffraction mode

When the electrons travel into the crystalline specimen, the specimen diffracts the electrons in a direction following Bragg's law. Because the objective lens focuses parallel beams, diffraction results in a diffraction pattern in the back focal plane of the object lens. The diffraction pattern on the TEM screen represents the intercept between the Ewald sphere and the reciprocal lattice (Fig. 5.5). Therefore, the electron diffraction is a valuable tool for the crystallographic analyses. Furthermore, diffraction from selected regions of the specimen can be obtained by inserting the selected area diffraction (SAD) aperture into the image plane of the objective lens.

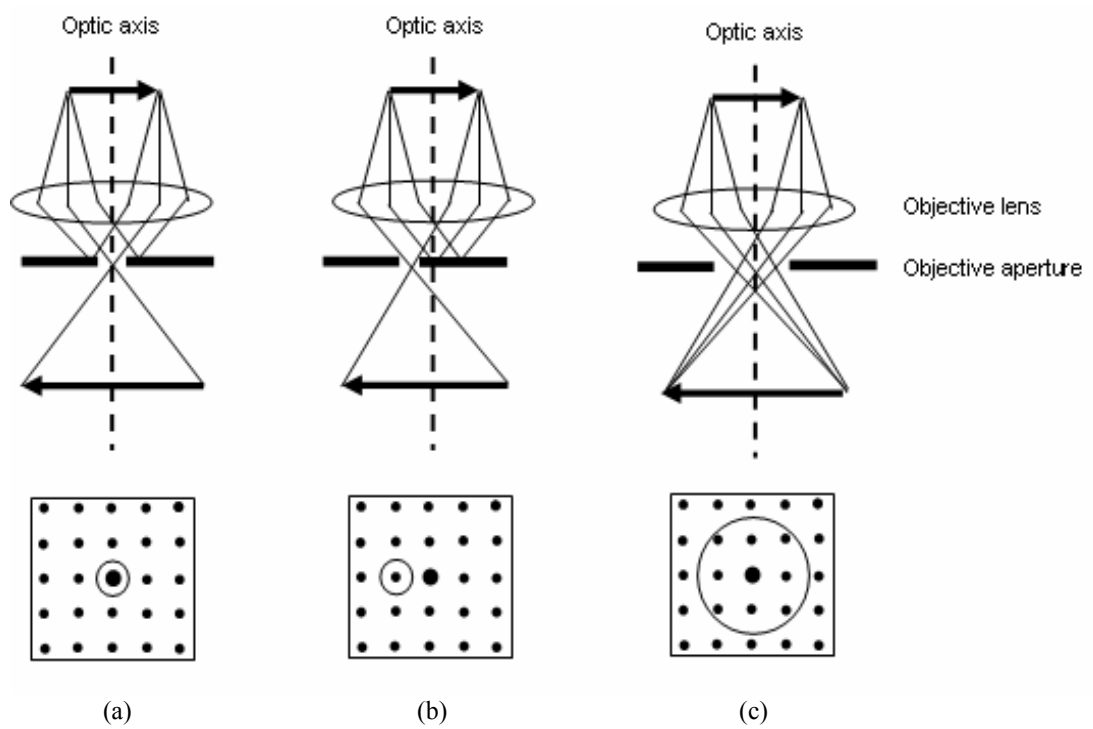

Fig. 5.4 Types of TEM imaging modes: (a) Bright-field image, (b) Dark-field image, (c) High-resolution image (lattice image).

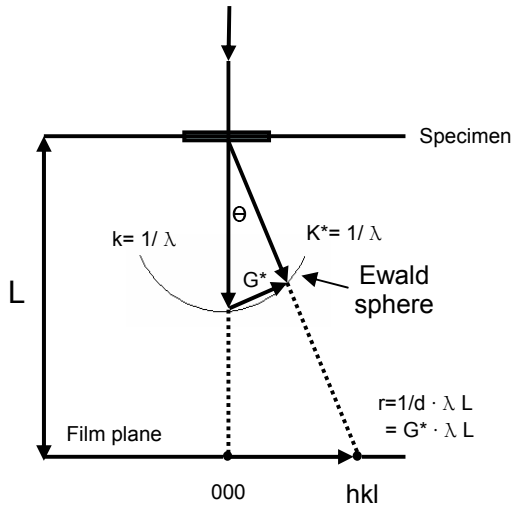

Fig. 5.5 Electron diffraction in the TEM; the diffraction pattern includes the planes of the reciprocal lattice. Each point in the pattern can be indexed by the crystallographic planes (*hkl*).

5.3. Characterization of the magnetic properties

The magnetic hysteresis loop and temperature dependence of the magnetization have been investigated by the SQUID (Superconducting Quantum Interference Device) magnetometer. In the SQUID magnetometer, the SQUID sensor detects a very small magnetic field (10^{-8} emu), converting the change of the magnetic flux into the oscillation of a voltage signal [67]. The SQUID magnetometer used in the experiments is a MPMS XL from Quantum Design. The MPMS system consists of the probe, the SQUID assembly, the dewar, and the electronic control system. The probe allows magnetic measurements by using a superconducting electromagnet giving fields up to 7 T. The temperature control system in the probe allows temperature variations from 1.5 K to 350 K with the precision of 0.1 K. In the SQUID assembly, the connected input coil and pick up loop are installed under the SQUID sensor and a sample is moved through the pick up loop by a stepper motor. The movement of a sample can cause a change of the magnetic flux in the pick up loop. This makes the current flow into the input coil, producing a flux change in the SQUID sensor. The sample is mounted on a plastic straw and attached on the sample load which is brought into the position in the SQUID assembly in the dewar.

The dewar has a helium reservoir. The liquid helium is used for cooling both the superconducting electromagnet and the sample space.

The electronic system controls the movement of the sample, the magnetic field and the temperature. The magnetic moment of a specimen can be determined from the measured SQUID voltages.

6. Evaluation methods

6.1 X-ray diffraction from multilayer structures

Generally, the condition for diffraction from a crystalline specimen is simply expressed by Bragg's law

$|\boldsymbol{Q}| = 2\, k_i \sin\theta$, ($\boldsymbol{Q}$: reciprocal the reciprocal lattice vector)

$\boldsymbol{Q} = h\, \boldsymbol{a}^* + k\, \boldsymbol{b}^* + l\, \boldsymbol{c}^*$ (h, k, l : integers).

However, as a multilayer structure is considered as a one-dimensional system in the direction perpendicular to the substrate, only the $\boldsymbol{c}^*$ component in reciprocal vector components is meaningful. Therefore,

$$|\boldsymbol{Q}| = l\, \boldsymbol{c}^* = l\ (2\pi/\Lambda) = 2\, k_i \sin\theta = 2k_i \frac{n}{2} \cdot \frac{\lambda_x}{\Lambda} \tag{6.1}$$

Eq. (6.1) is the Bragg equation for the multilayer structure. Here, Λ is the modulation period in the multilayer structure which is represented as $\Lambda = d_A + d_B$ (d_A , d_B are the thicknesses of the elemental A and B layer). The value of λ_x is the wavelength of the X-ray radiation. This unique diffraction condition for multilayer structures results from the interfaces between two elemental layers, and gives additional peak positions which are not seen in a normal diffraction pattern of elemental layers. Since these peaks appear near the normal Bragg diffraction peaks, they are called "satellite peaks". With the assumption of perfect interfaces in multilayer films, the angular position of the diffraction peak is simply indexed by the modulation period Λ. However, the real interfaces of the films are not sharp but diffusive. The roughness of diffusive interfaces can be described by the value of d^*, which is defined as

$$d^* = \frac{\Lambda}{(N_A + N_B)} .$$

N_A and N_B are the number of atomic planes of element A and B in the film. By considering the interface roughness d^*, eq. (6.1) is rewritten as [68]

$$2\frac{\sin\theta_n}{\lambda_x} = \frac{1}{d^*} \pm \frac{n}{\Lambda} \tag{6.2}$$

By eq. (6.2), the positions of the satellite peaks are indexed by the integral number n in the case of a multilayer structure.

6.2 Degree of structural ordering to the $L1_0$-phase

Above the transition temperature (T ≈ 1300 ºC), the Fe and Pt atoms of FePt alloys are arranged randomly on the atomic sites of a fcc lattice. With the assumption of a perfect disorder, the probability that a particular site is occupied by a Fe atom is ½ , which is also the probability for a Pt atom. Below the transition temperature, the Fe and Pt atomic positions are arranged into alternating stacks of Pt and Fe atomic planes of a fct lattice. Therefore, the change in atomic positions necessarily causes a change in XRD spectral lines. The diffraction lines from the patterns of both disordered and ordered phases are called fundamental lines, and the extra lines which appear in the pattern of an ordered alloy are called superlattice lines. The presence of the superlattice peak is a direct evidence of the ordering transformation. In FePt alloys the fundamental lines appear on the spectrum positions obtained for fcc lattice which has unmixed (*hkl*) indices (all odd or even). However, the superlattice lines can occur in 2θ positions in which the indices (*hkl*) are mixed. The scattering parameters for the intensity of fundamental lines is described by [69, 70]

$$F_{Fundamental} = 4 \cdot (\frac{1}{2} f_{Fe} + \frac{1}{2} f_{Pt}) = 2 f_{Fe} + 2 f_{Pt} \tag{6.3}$$

and for the intensity of superlattice lines [69, 70]

$$F_{Superlattice} = 4 \cdot S(x_{Fe} - x_{Pt}) \tag{6.4}$$

where f_{Fe} and f_{Pt} are the atomic scattering factors, and x_{Fe} and x_{Pt} are the atomic ratios of each elements. The parameter S in eq. (6.4) can be used to quantify the degree of ordering to the $L1_0$ structure in the alloy, and is therefore called ordering parameter. This structural ordering parameter S has the same meaning as the parameter mentioned in Chapter 4.1.2. According to eq. (6.3) and eq. (6.4) the ordering parameter is obtained as the intensity ratio of the superlattice to the fundamental peak

$$\frac{I_{(001),Superlattice}}{I_{(002),Fundamental}} = \left[\frac{4 \cdot S \cdot (x_{Fe} f_{Fe} - x_{Pt} f_{Pt})}{2 f_{Fe} + 2 f_{Pt}} \right]^2 \cdot A \quad . \tag{6.5}$$

The constant A in eq. (6.5) is originated from the background intensity of the instrument. In order to eliminate A and calculate the more precise value of the ordering parameter S, we can take the intensity ratios of $R_{Meas.}$ and $R_{Cal.}$ as following

$$R_{Cal.} = \left[\frac{I_{(001),Superlattice}}{I_{(002),Fundamental}} \right]_{Cal.} = \left[\frac{2(x_{Fe} f_{Fe} - x_{Pt} f_{Pt})}{2(f_{Fe} + f_{Pt})} \right]^2 \cdot A \ . \tag{6.6}$$

Here, the ordering parameter S is assumed to unity as a perfect ordered alloy. $R_{Meas.}$ is

$$R_{Meas.} = \left[\frac{I_{(001),Superlattice}}{I_{(002),Fundamental}} \right]_{Meas.} = \left[\frac{4 \cdot S \cdot (x_{Fe} f_{Fe} - x_{Pt} f_{Pt})}{2(f_{Fe} + f_{Pt})} \right]^2 \cdot A \tag{6.7}$$

Finally the ordering parameter S is obtained by

$$S = \left(\frac{R_{Meas.}}{R_{Cal.}} \right)^{\frac{1}{2}} \ . \tag{6.8}$$

In this experiment, integrated intensities of $I_{(001)}$ and $I_{(002)}$ from the XRD spectra of $L1_0$-FePt films are chosen for the superlattice and fundamental diffractions, respectively.

6.3 Film thickness by XRR

The determination of the spontaneous polarization J_s of a magnetic thin film magnet requires the exact value of the volume of the deposited film. The volume of the film can be calculated from the thickness and the size of the substrate (5 mm × 5 mm). The thickness of the film has been measured by X-ray reflectivity (XRR).

When the X-rays hit the surface of a thin film under a very small angle, i.e. grazing incidence conditions, most of the rays are reflected from the film surface. The profile of reflected intensity with respect to the incidence angle contains information about the film thickness and density. Fig. 6.1 is a typical result of a XRR experiment.

In the XRR experiments, the density of film can be related to the δ value in the refractive index n according to [71]

$n = 1 - \delta + i\beta$ with $\delta = \frac{r_0 N_a}{2\pi}\lambda^2 \frac{\rho}{A}(Z + f')$ and $\beta = \frac{\mu\lambda}{4\pi}$

(r_0 : radius of electron, N_a: Avogadro's number, λ: X-ray wavelength, A: atomic mass, $Z + f'$: atomic scattering factor, μ: absorption coefficient).

In the case of a total reflection of X-rays, no absorption occurs and the β value is ignored. By Snell's law the refractive index and incidence angle θ are related as $n_1 \cos\theta_1 = n_2 \cos\theta_2$, where for total reflection $n_1 = 1$, and $\cos\theta_2 = 1$ and $\cos\theta_1 = n_2 = 1 - \delta$ hold.

For a very small angle, the following condition holds

$$\sin^2 x = \frac{1 - \cos 2x}{2} = x^2 . \tag{6.9.a}$$

If $2x = \theta_1$ then the condition writes

$$\cos\theta_1 = 1 - \frac{\theta_1^2}{2} = 1 - \delta . \tag{6.9b}$$

Therefore, θ_1 is given by

$$\theta_1 = \sqrt{2\delta} = \lambda\left(\frac{N_a r_0 \rho (Z + f')}{\pi A}\right)^{1/2} . \tag{6.9c}$$

With eq. (6.9) and measuring θ_1 (the critical angle for total reflection) the density of the film can be determined. The critical angle θ_1 is characterized by the abrupt decrease in the reflective intensity. The value of the angle θ_1 is obtained by fitting the experimental data.

On the other hand, as the incidence angle increases over the critical angle, θ_1, X-rays penetrate inside the film and there are reflections from the top and the bottom of the film. Due to the path difference between these rays, the reflected rays lead to interference fringes in the intensity profile which are dependent on the incidence angle, and not on the optical or acoustic properties of the material. The angular dependence of the mth interference maximum with a path difference of $\Delta = m\lambda$ is expressed as

$$\theta_m^2 = m^2 \frac{\lambda^2}{4d^2} + 2\delta = m^2 \frac{\lambda^2}{4d^2} + \theta_1^2 \tag{6.10}$$

with X-ray wave length λ, integer parameter m and film thickness d.

Therefore, the film thickness is given by

$$d = \frac{\lambda}{2} \frac{1}{\sqrt{\theta_{m+1}^2 - \theta_1^2} - \sqrt{\theta_m^2 - \theta_1^2}} = \frac{\lambda}{2} \frac{1}{\theta_{m+1} - \theta_m} \qquad \text{for } \theta_m >> \theta_1 \ . \tag{6.11}$$

The thickness is often determined with a precision better than 1 Å for measurements of interference fringes in a bigger angular range.

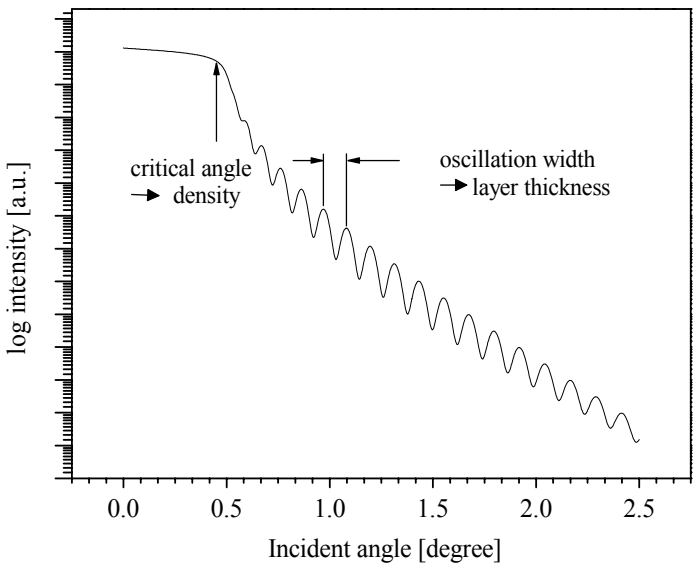

Fig. 6.1 Typical result of a XRR measurement.

6.4 Correcting the hysteresis loop

6.4.1 Diamagnetism of the substrate

The $L1_0$-FePt ordered films in all experiments were deposited on MgO (001) single crystal substrates. Since the MgO substrate is diamagnetic, the raw data measured in the SQUID magnetometer includes the diamagnetic contribution of the MgO substrate. To obtain the spontaneous polarization of the $L1_0$-FePt film the diamagnetic moment has to be subtracted from the raw magnetic moment.

The diamagnetic susceptibility is given by

$$\chi_d = \frac{N_v \mu_m}{H} \ . \tag{6.12}$$

The diamagnetic moment of a substance is independent of temperature and depends linearly on the applied magnetic field. Therefore, the correction for the diamagnetism has been carried out by subtracting a straight line with a slope calculated from the high field region of the hysteresis loop. Fig. 6.2 shows the raw hysteresis loop and the corrected loop.

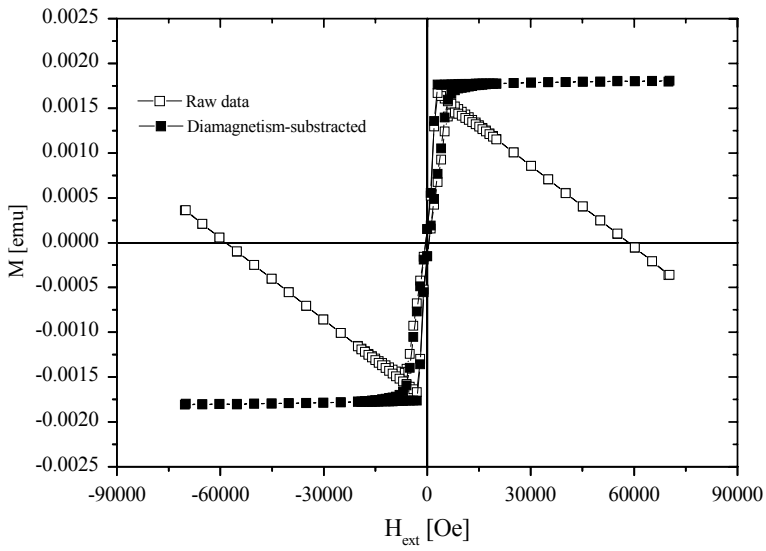

Fig. 6.2 Correction of the diamagnetism of the substrate for the hysteresis loop of a $L1_0$-$Pt_{40}Fe_{60}$ thin film.

6.4.2 Demagnetization factor

For measurements of the magnetization behavior of a thin film perpendicular to the film plane, the external field $\mu_0 \boldsymbol{H}_{ext}$ must be corrected due to the demagnetization effect of the specimen. The internal field $\mu_0 \boldsymbol{H}_{int}$ is obtained by subtracting the demagnetization field ($N \cdot \boldsymbol{J}$) from the external field ($\mu_0 \boldsymbol{H}_{ext}$)

$$\mu_0 \boldsymbol{H}_{int} = \mu_0 \boldsymbol{H}_{ext} - N \cdot \boldsymbol{J} \ . \tag{6.13}$$

Here, N is the demagnetization factor which depends on the shape of the specimen. The internal field is the actual field which acts on the polarization of the specimen. The calculation of the demagnetization factor is a complicated procedure except for some special cases, as for ellipsoidal and spherical shape. For infinitely extended thin films the demagnetization factor

parallel and perpendicular to the film direction is given by $N_{//} = 0$ and $N_{\perp} = 1$. When the hsyetersis loop of a textured film with uniaxial *c*-axis perpendicular to the film plane (Fig. 6.3) is corrected with the appropriate demagnetization factor, the shape would be a more or less perfect rectangle. For the hysteresis loop in Fig. 6.4 a demagnetization factor of $N_{\perp} = 0.25$ is determined. The deviation of the $N_{\perp}$-value from the hypothetical one ($N_{\perp} = 1.00$) originates from the complex behavior of the stray field at sharp edges in the case of rectangular thin films.

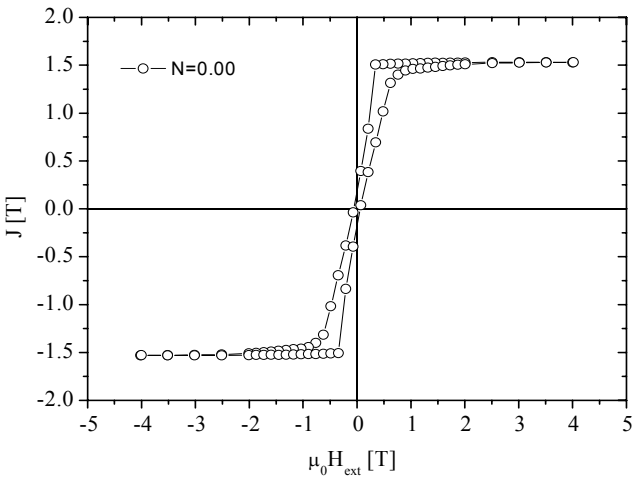

Fig. 6.3 Hysteresis loop of a $L1_0$-$Pt_{40}Fe_{60}$ film without demagnetization correction.

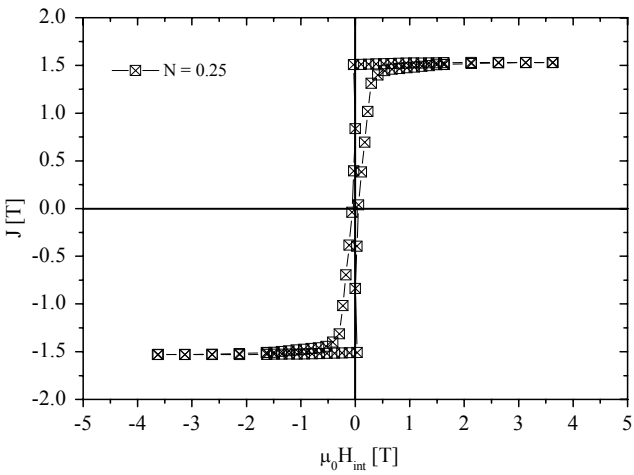

Fig. 6.4 Corrected loop of the $L1_0$-$Pt_{40}Fe_{60}$ film of Fig. 6.3 for $N = 0.25$.

6.5 Intrinsic magnetic properties

6.5.1 Saturation polarization, J_s

The saturation polarization J_s can be evaluated from the approach to saturation of ferromagnetic materials. According to Chapter 2.6, the extrapolation of a plot of J over $1/(\mu_0 H)^2$ to the y-axis results in the value of the saturation polarization J_s. An example of for such a plot is shown in Fig. 6.5.

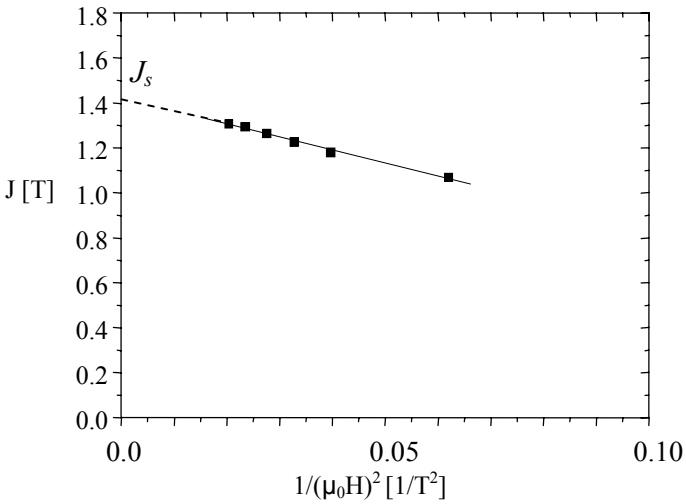

Fig. 6.5 Extrapolation plot to obtain the saturation polarization of a $L1_0$-FePt film.

6.5.2 Magnetocrystalline anisotropy constant K_1

By the Sucksmith-Thomson relation [72], the magnetocrystalline anisotropy constant K_1 is evaluated using the susceptibility χ of the initial magnetization curve where the magnetic field is applied perpendicular to the easy axis of a specimen. The anisotropy constant is given by

$$\chi = \frac{J_S^2}{2K_1} \quad . \tag{6.14}$$

This relation is valid only for a single crystal specimen. However, for a polycrystalline magnet with misoriented grains the equation can be modified to[73]

$$\chi = \frac{J_S^2}{2K_1}(1 - \frac{1}{6}\delta\theta_0^2) , \tag{6.15}$$

where the misorientation angle is assumed to follow a Gaussian distribution, and $\delta\theta_0$ is the standard deviation. Another method for obtaining K_1 is to simulate the demagnetization curve and fit the experimental curve to it. For $L1_0$-FePt alloy films with isotropic magnetization behavior, the magnetization curves with certain K_1 and J_s values are simulated with the program developed by Köhler [74]. From the matching of the simulated loop with the measured loop K_1 can be evaluated.

6.5.3 Exchange constant *A*

The temperature dependence of the exchange constant *A* can be evaluated using the Bloch's $T^{3/2}$-law for thermally excited spin waves. The temperature dependence of $J_s(T)$ is given by the relation

$$J_s(T) = J_{s0}\left(1-\left(\frac{T}{T_0}\right)^{3/2}\right) . \qquad (6.16)$$

By plotting J_s(T) versus $(T/T_0)^{3/2}$ J_{so} and T_0 can be determined by extrapolation to the axes (Fig. 6.6).

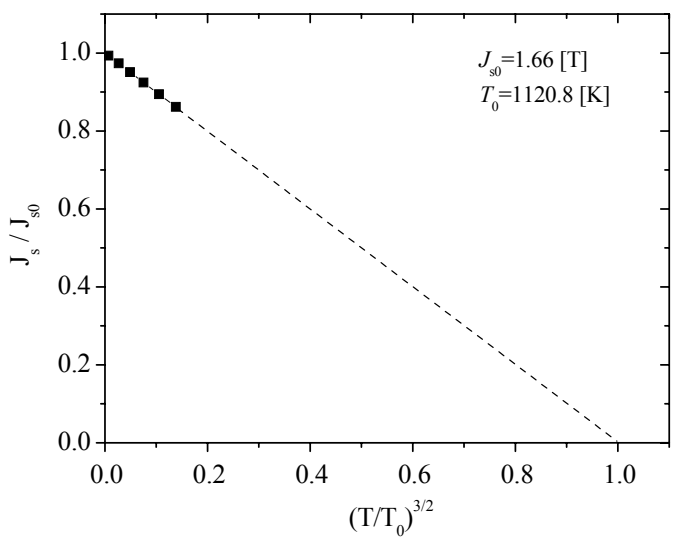

Fig. 6.6 Plot of Bloch $T^{3/2}$-law for $L1_0$-$Fe_{50}Pt_{50}$ film to determine J_{s0} and T_0.

The characteristic temperature T_0 is related to the spin wave stiffness constant D_{sp} by

$$T_0 = \left(\frac{M_{s0}}{0.117\mu_B} \right)^{2/3} \frac{D_{sp}}{k_B} . \tag{6.17}$$

From eq. (6.17) the temperature dependence of the exchange constant A can be obtained from the relation [32]

$$A(T) = \frac{M_s(T) D_{sp}}{2g\mu_B} . \tag{6.18}$$

The value of μ_B is 9.27×10^{-24} [Am^2]. The Landé g-factor is assumed to be 2.0 in case of $L1_0$-FePt alloys.

6.6 Microstructural parameters

The microstructural parameters in eq. (2.19) are analyzed for an isotropic magnet by

$$\frac{\mu_0 H_c(T)}{J_s(T)} = \alpha_K \alpha_{ex} \left(\frac{\mu_0 K_1(T)}{J_s(T)^2} \right) - N_{eff} \tag{6.19}$$

and for an anisotropic magnet by

$$\frac{\mu_0 H_c(T)}{J_s(T)} = \alpha_K \alpha_\phi \left(\frac{2\mu_0 K_1(T)}{J_s(T)^2} \right) - N_{eff} . \tag{6.20}$$

When the values for the coercivity, spontaneous polarization, and anisotropy constant are known for different temperatures, $\mu_0 H_c(T)/J_s(T)$ versus $\mu_0 K_1(T)/J_s(T)^2$ or $\mu_0 2K_1(T)/J_s(T)^2$ plots are possible. From the slope and y-axis-intersection of the obtained straight line the microstructural parameters α_{ex}, α_K and the effective demagnetization factor N_{eff} can be obtained.

7. Results: $L1_0$-FePd films

7.1 Ordered $L1_0$-FePd films on quartz substrates

$L1_0$-FePd alloy films have been prepared by annealing the multilayer structure as shown in Fig. 7.1. From the XRD diffraction spectra in Fig. 7.2 it was found that the as –deposited multilayer films were composed of Fe (110) and Pd (111) planes. The heat-treatments were performed at 500 ºC for 60 min in two different atmospheres of high vacuum (below 1.0×10^{-6} torr) and H_2 gas (2 bar). After annealing, the multilayer films had transformed into the ordered $L1_0$-FePd phase with (111) textured polycrystalline structure. The X-ray diffraction spectra of the heat-treated films showed the (111) diffraction peaks of the ordered $L1_0$-FePd alloy with a lattice spacing of d_{111} = 2.198 Å.

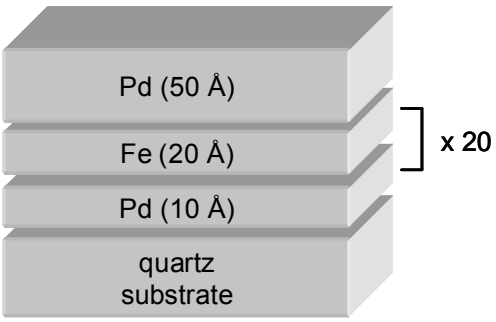

Fig. 7.1 Fe/Pd multilayer structure for preparing ordered $L1_0$-FePd alloy films.

The magnetic hysteresis loops (Fig. 7.3) were measured at 40 K using a SQUID magnetometer with the external field applied parallel to the film plane. The as-deposited Fe/Pd multilayer had a very small coercive field of only 50 Oe, which is typical for thin Fe layers. After annealing treatments in both high vacuum and hydrogen atmosphere the coercivity was drastically increased due to the formation of ordered $L1_0$-FePd. Although the X-ray diffraction patterns showed no difference between annealing in hydrogen and vacuum atmosphere, the magnetization behavior was different. The hysteresis loops of films heat-treated in hydrogen and in high vacuum showed a round and square shape, respectively.

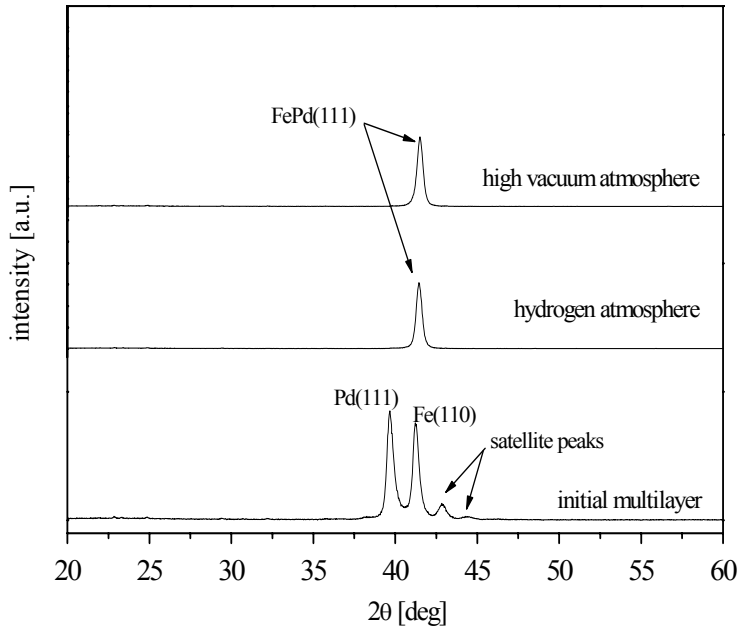

Fig. 7.2 X-ray diffraction spectra of the Fe/Pd multilayers shown in Fig. 7.1 after annealing at 500 ºC for 240 min in high vacuum and hydrogen atmosphere.

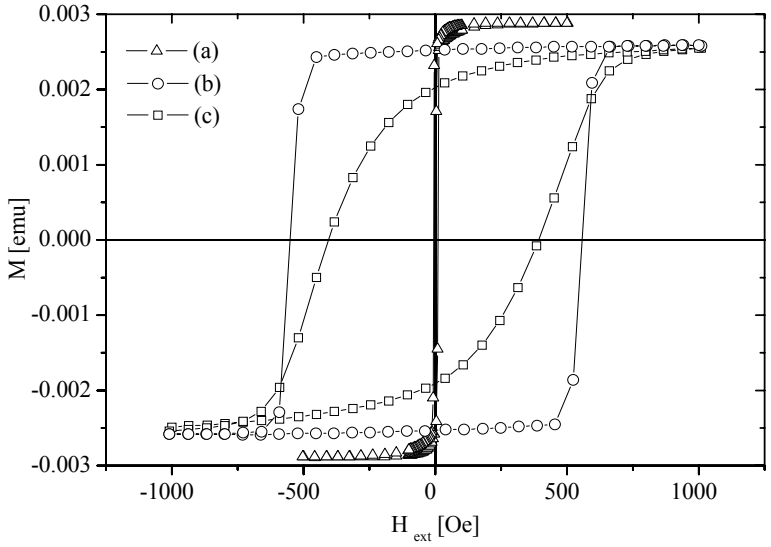

Fig. 7.3 The magnetic hysteresis loops measured at 40 K of a (Pd 50 Å / (Fe 20 Å / Pd 10 Å) × 20) multilayer on a quartz substrate (a) and ordered $L1_0$-FePd films obtained after annealing at 500 ºC for 60 min in both hydrogen (b) and vacuum atmosphere (c). The external field was applied parallel to the film plane.

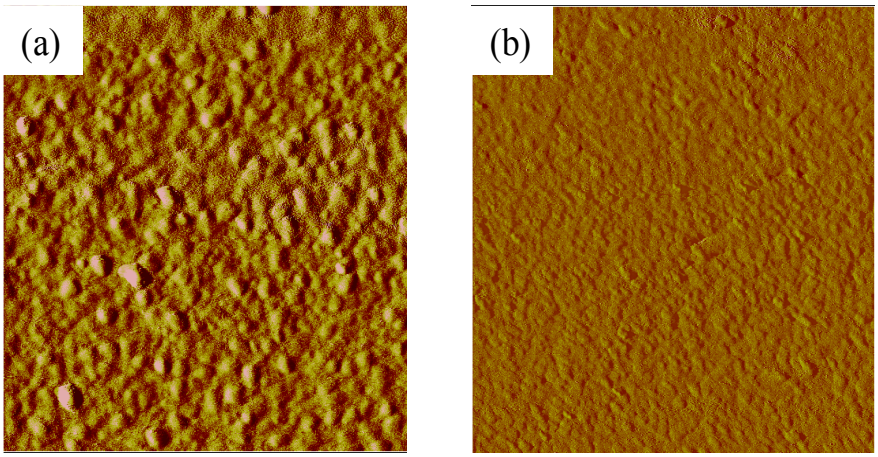

Fig. 7.4 AFM scan images (5 μm × 5 μm) of the $L1_0$-films annealed in hydrogen (a) and vacuum (b) atmospheres.

According to the atomic force microscopy (AFM) scan images of Fig. 7.4, the morphology of the film annealed in hydrogen atmosphere shows larger grains than the morphology of the film annealed in vacuum atmosphere. The difference is due to the fact that during the heat treatment the hydrogen gas can reduce the oxide inclusions in grain boundaries of the film and anomalous grain growth takes place. A similar anomalous grain growth in hydrogen atmosphere was also observed in Ni films by Wagner and Müller [75]. The coarse grains make a rough film surface and therefore nucleation becomes much easier. This is the reason of the smaller coercive field of the film heat-treated in hydrogen.

7.2 Ordered $L1_0$-FePd films on MgO substrates

Ordered $L1_0$-FePd films were also prepared from Fe/Pd multilayers on MgO substrates. However, another multilayer stacking sequence was used on the MgO substrate compared to that on quartz. The stacking sequence started with Fe on the MgO substrate and the final layer was Pd. The thick Pd cover layer in Fig. 7.1 was not used. The multilayer was annealed at 500 ºC for 30 min in Ar atmosphere, and the magnetization behavior was investigated.

The hysteresis loops measured at 40 K are shown in Fig. 7.5. From the magnetization behavior, it becomes clear that the film is easier magnetized with the external field perpendicular to the film plane, i.e. the out-of plane direction is a preferred orientation due to the chemical ordering to $L1_0$-FePd. The perpendicular alignment of the *c*-axis is obtained by using the single crystalline

MgO (001) substrates since the (001) surface of MgO favors epitaxial growth of $L1_0$-FePd with the c-axis aligned in the out-of-plane direction.

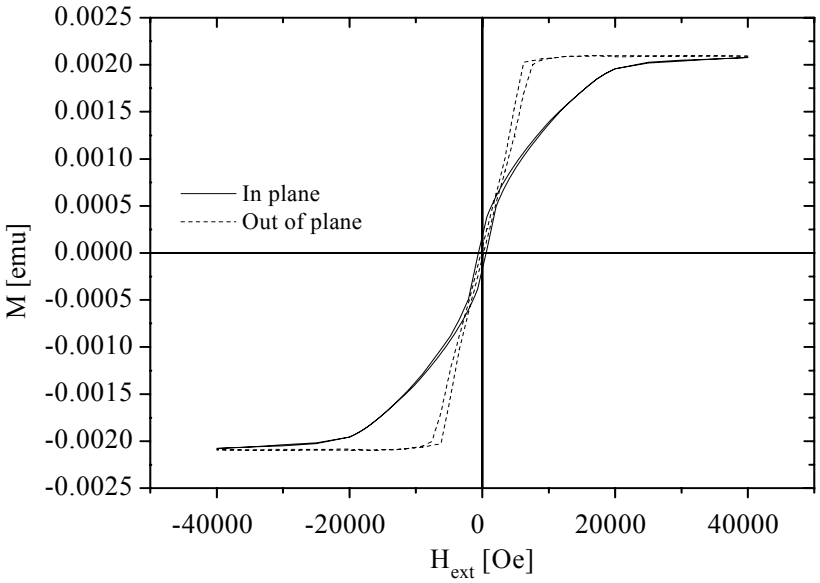

Fig. 7.5 Magnetic hysteresis loops measured at 40 K for a $L1_0$-FePd film on a MgO (001) substrate after annealing at 500 ºC for 30 min in Ar atmosphere (precursor: (Pd 10 Å / Fe 20 Å) × 20 / MgO). The external field was applied parallel and perpendicular to the film plane.

.

8. Results: $L1_0$-FePt films

The $L1_0$-phase of FePt possesses with K_1=6.6 MJ/m^3, a much higher anisotropy constant than $L1_0$-FePd (K_1=1.8 MJ/m^3). Owing to the small K_1 value, the $L1_0$-FePd films showed only moderate coercivities for fields applied perpendicular to the film plane. Therefore to increase the coercivity the Pd layers in Fe/Pd multilayer on MgO substrates of Chapter 7.2 were replaced in the following by Pt layers. The $L1_0$-FePt films have been also prepared from the Fe/Pt multilayer precursors.

8.1 Fe/Pt multilayers

The $L1_0$-FePt alloy films were prepared by heat treating multilayer precursors which were composed of very thin elemental Fe and Pt layers. The idea of synthesizing the ordered $L1_0$-phase from multilayers stems from the fact that alternating layers of Fe and Pt imitate the crystal structure of the $L1_0$-phase, which has a face-centered-tetragonal (fct) unit cell composed of parallel Fe and Pt atomic planes perpendicular to its *c*-axis. Common problems in growing $L1_0$-FePt alloy films are a high transformation temperature, and the alignment of the crystallographic *c*-axes of the individual grains. By introducing the multilayer precursor, it is expected to reduce the transformation temperature, and align the *c*-axes more easily. These multilayer precursors were deposited by ion beam sputtering. After preparation the films were analyzed by XRD and TEM and the magnetic properties were characterized by a SQUID magnetometer.

8.1.1 Preparation of Fe/Pt multilayers

Fig. 8.1 shows the Fe/Pt multilayer precursor used to produce a $L1_0$-FePt film. The composition of the $L1_0$-FePt alloy is controlled by changing the elemental layer thicknesses in the precursor. The details of the Fe/Pt multilayers of different total thicknesses are summarized in Table 8.1. The total thickness of the thinnest Fe/Pt multilayer was 7.5 nm.

Fig. 8.1 Fe/Pt multilayer design for producing $L1_0$-FePt film after post-annealing.

Specimen number	Nominal composition	Individual layer thickness		Number of iterations [X]	Total Thickness [nm]
		Pt [Å]	Fe [Å]		
1	$Fe_{60}Pt_{40}$	14	16	18	54
2	$Fe_{57}Pt_{43}$	14	14	19	53
3	$Fe_{54}Pt_{46}$	14	13	20	54
4	$Fe_{50}Pt_{50}$	14	11	21	52
5	$Fe_{53}Pt_{47}$	16	14	9	27
6	$Fe_{60}Pt_{40}$	56	64	5	60
7	$Fe_{60}Pt_{40}$	14	16	9	27
8	$Fe_{60}Pt_{40}$	14	16	5	15
9	$Fe_{60}Pt_{40}$	7	8	5	7.5

Table 8.1 Fe/Pt multilayer precursors for producing $L1_0$-FePt monolayers of different nominal compositions and total thicknesses.

The substrate for the multilayer is a MgO (001) polished single crystal which is cleaned before it is brought into the sputter chamber. The deposition rates for Fe and Pt are 2.8 Å/min.

8.1.2 Structure of Fe/Pt multilayers

The structure of the multilayer films was investigated by X-ray diffraction. The results are shown in Fig. 8.2 and Fig. 8.3. In Fig. 8.2, typical oscillatory satellite peaks resulting from the superlattice structures in (Pt 14 Å/Fe 16 Å) ×18 and (Pt 14Å/Fe 14Å)×19 multilayers can be seen with the strong intensities of the MgO (001) substrate, and the Pt (002) plane peaks. With decreasing superlattice period Λ, i.e. with decreasing thickness of a Fe-Pt bilayer stack, peaks from Fe (110), Pt (002), MgO (001) and superlattice interfaces become visible in the X-ray spectra (Fig. 8.3). In the case of thicker bilayer stacks (Fig. 8.2) the Fe (110) peak is partly overlapped by other peaks.

For the calculation of the angular peak position eq. (6.2) is used and the lattice spacings of the constituent layers are set to be a_{Fe} = 2.030 Å and a_{Pt} = 1.960 Å which are the planar distances of Fe (110) and Pt (002), respectively. The wave length of the used X-ray is 1.5406 Å (Cu- K_α). The position of some peaks cannot be determined because the range of angles is overlapping

with the angles of the Pt (002) and Fe (110) peaks. However, the θ_2 and θ_3 peaks can be clearly seen and are characterized for different values of the superlattice period Λ. The angular positions of θ_2 and θ_3, the superlattice period Λ and the d^* values are listed in Table 8.2.

Sample	θ_2 [deg]		θ_3 [deg]		Λ [Å]	d* [Å]
	Exp.	Cal.	Exp.	Cal.		
(Pt 14 Å / Fe16 Å) × 18	53.8	51.8	56.9	55.1	30.0	1.99
(Pt 14 Å / Fe 14 Å) ×19	52.8	52.4	56.0	55.9	28.0	1.99
(Pt 14 Å / Fe 13 Å) × 20	51.9	52.6	54.8	56.4	27.0	1.99
(Pt 14 Å / Fe 11 Å) × 21	51.2	53.1	-	57.1	25.0	1.99

Table 8.2 X-ray analysis of Fe/Pt multilayers. θ_2 and θ_3 are representing the angular peak positions of the superlattice diffraction. Λ and d^* are obtained from the individual layer thicknesses. The experimental and calculated angular position values are compared with each other.

The calculated peak positions obtained from eq. (6.2) are compared to those of the experimental spectra. The first approximation shows agreement between the experimental and calculated peak position. However, a more detailed analysis reveals differences in the peak positions. The differences are due to the accuracy of the X-ray machine and the intermixing of the interfaces. The positions of the superlattice peaks depend on the thickness of the individual layers. The multilayer structure of the grown films was confirmed by these results, and no ordered $L1_0$-FePt peaks were observed in the X-ray results before annealing.

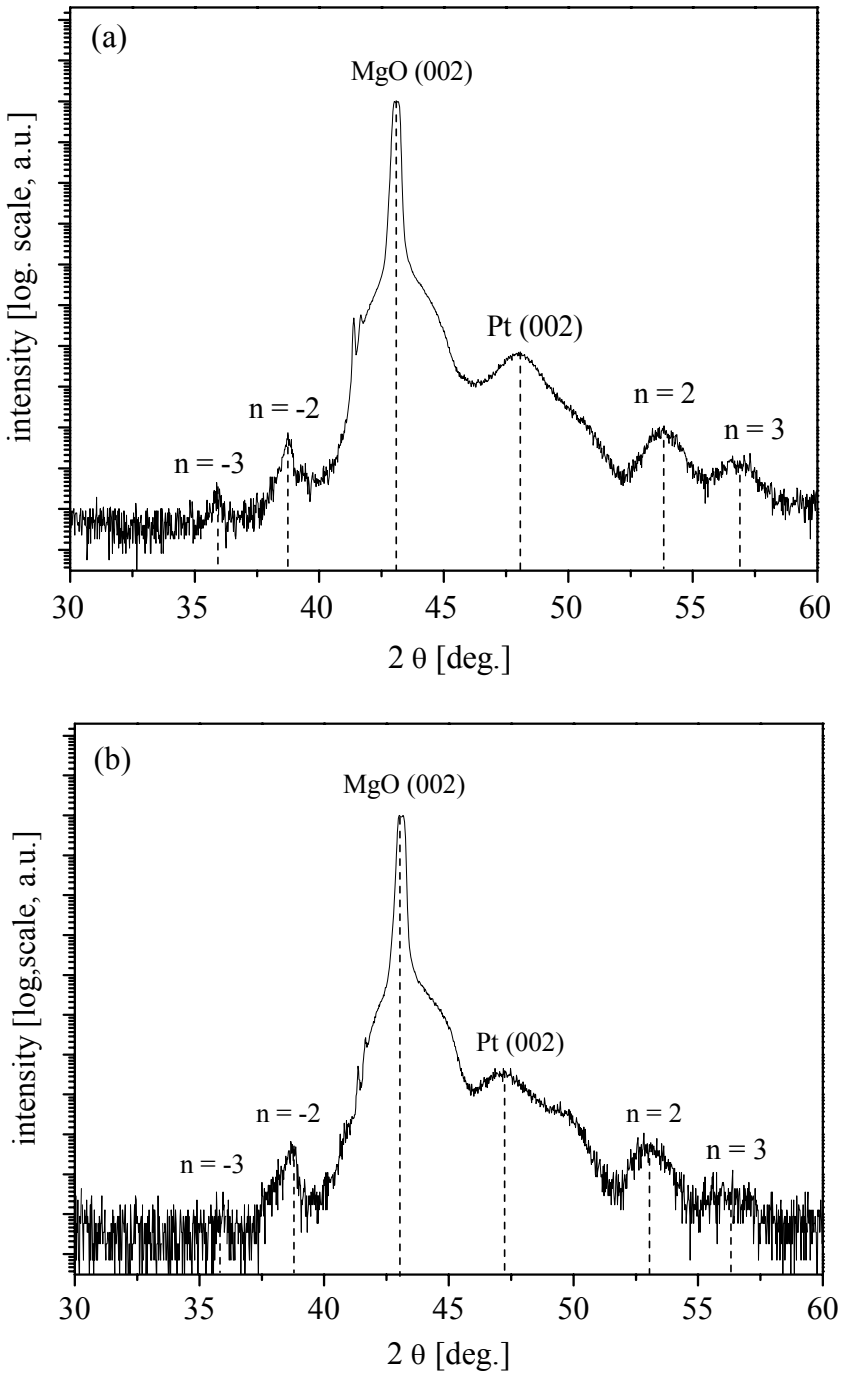

Fig. 8.2 High-angle X-ray diffraction spectra of Fe/Pt multilayers: (a) (Pt14Å/Fe16Å)×18/MgO, and (b) (Pt14Å/Fe14Å)×19/MgO. These mutilayers result in the films of nominal compositions of $Fe_{60}Pt_{40}$ and $Fe_{57}Pt_{43}$, respectively.

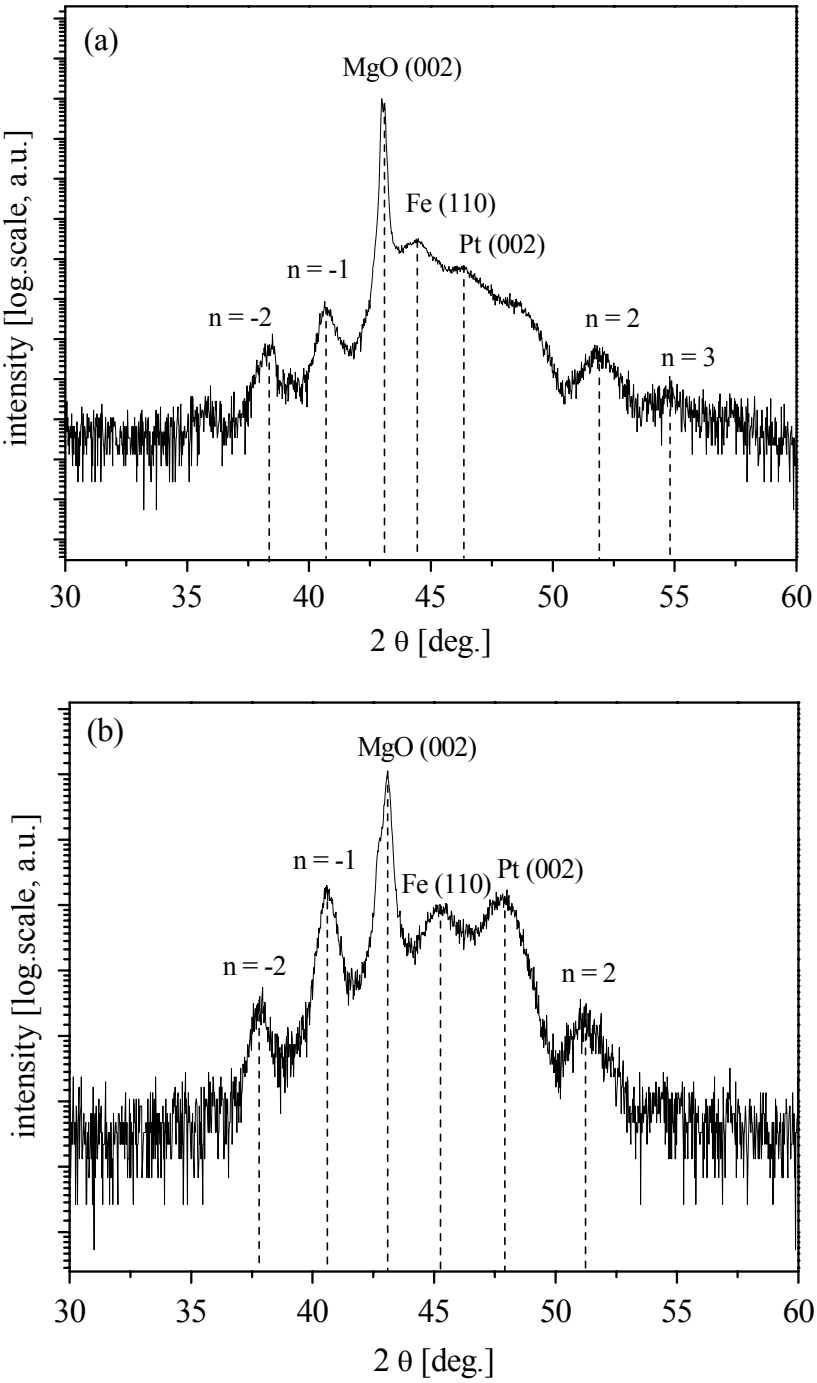

Fig.8.3 High-angle X-ray diffraction spectra of Fe/Pt multilayers: (a) (Pt 14Å/Fe 13Å)×20/MgO, and (b) (Pt 14Å/Fe 11Å)×21/MgO. These mutilayers result in the films of nominal compositions of $Fe_{54}Pt_{46}$ and $Fe_{50}Pt_{50}$, respectively.

8.1.3 TEM investigation of the multilayer structure

Fig. 8.4 shows the TEM image of a (Pt 56Å / Fe 64Å) × 5 multilayer cross-section on a MgO substrate. The TEM lamella has been prepared by focused ion beam (FIB). The multilayer is covered by a Pt layer to protect the lamella during preparation with the ion beam. The TEM image clearly shows the multilayer structure of the film and shows the individual thicknesses of the Fe and Pt layer. The Fourier transformation of a region in the figure demonstrates the crystallographic directions for the elemental bcc Fe and fcc Pt layers. The orientation relationship between Fe and Pt layers is Fe (110) // Pt (001) , i.e. the Fe (110) and Pt (001) planes are parallel to the MgO substrate. The nearest neighbor atomic distances in Fe (001), Fe (110) and MgO (002) planes are 2.86 Å, 2.47 Å, and 2.10 Å, respectively. Because of the large lattice mismatch of Fe (002) and MgO (002) planes, the growth of Fe (110) planes is preferred to the epitaxial growth of Fe (002) for relaxing the in-plane strain during film deposition. The Pt layer following the Fe (110) planes grown with (002) orientation. As the Fe layers seem to be thinner than the Pt layers, intermixing between Fe and Pt has already started at the interfaces. Each elemental layer has been grown as a single crystal without grain boundaries.

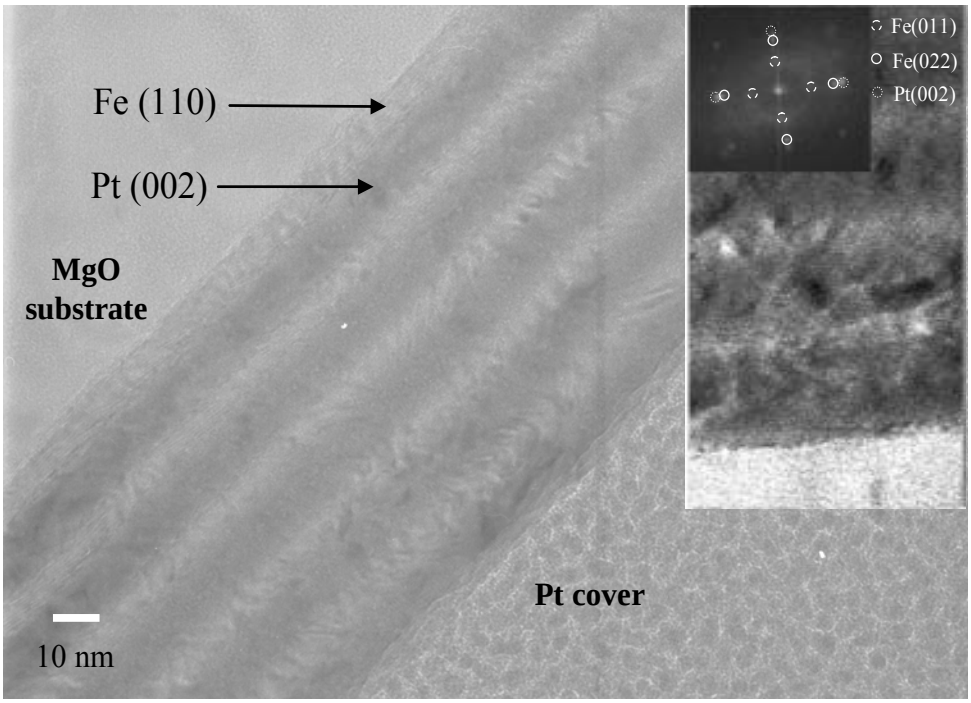

Fig. 8.4 TEM bright-field image and the Fourier transform (inset) of a (Pt 56Å / Fe 64Å)×5 multilayer on a MgO (001) substrate. This multilayer will result after annealing in the nominal composition of $Fe_{60}Pt_{40}$.

In the case of thinner individual layer thicknesses, as shown in Fig. 8.5 for a (Pt 14Å / Fe 16 Å) × 21 multilayer on MgO, the multilayer contains grains and severe intermixing between Fe and Pt layers occurring already in the as deposited state.

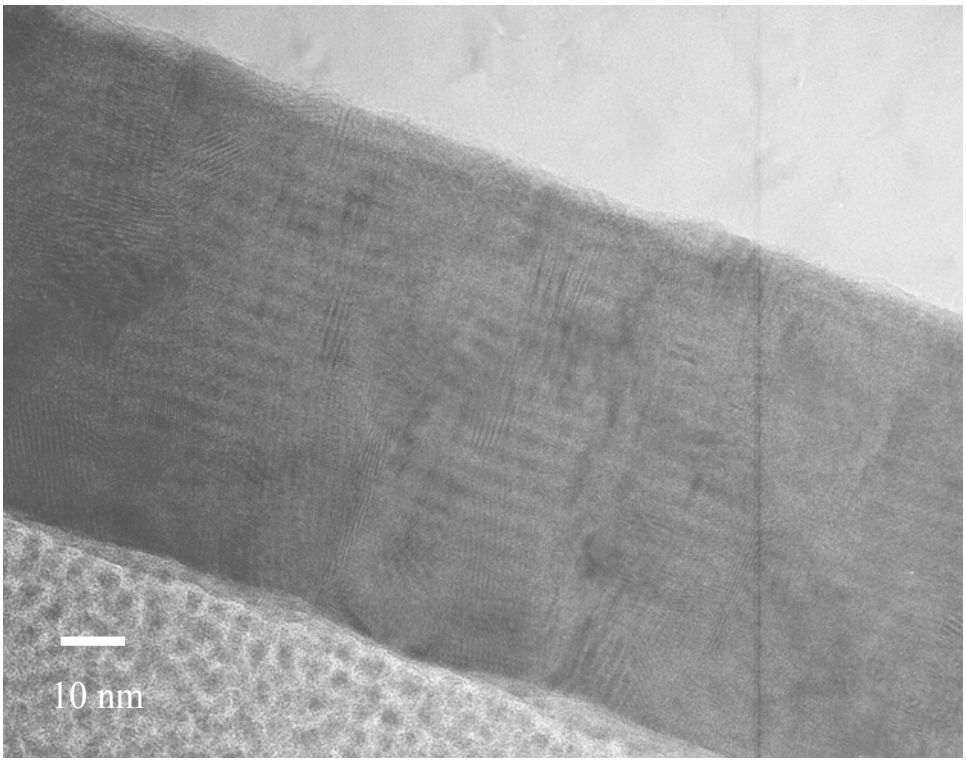

Fig. 8.5 TEM bright field image of a (Pt 14 Å / Fe 11 Å) × 21 multilayer on a MgO (001) substrate. This multilayer will result in the film of the nominal composition of $Fe_{60}Pt_{40}$.

8.1.4. Magnetic properties of the multilayers

In Fig. 8.6 the hysteresis loops measured at 40 K of the two different Fe/Pt multilayers before annealing are presented. The (Pt 56Å / Fe 64Å) × 5 / MgO multilayer (Fig. 8.6a) shows a typical soft magnetic behavior resulting from the Fe layers. The out-of-plane loop where the field is applied perpendicular to the film plane shows a slope caused by the demagnetization field due to the large shape anisotropy. The (Pt 14Å / Fe 11Å) × 21 / MgO multilayer (Fig. 8.6.b) shows a similar magnetization behavior. In this case also the shape anisotropy is dominant. The magnetic anisotropy of the multilayers does not depend on the elemental layer thicknesses.

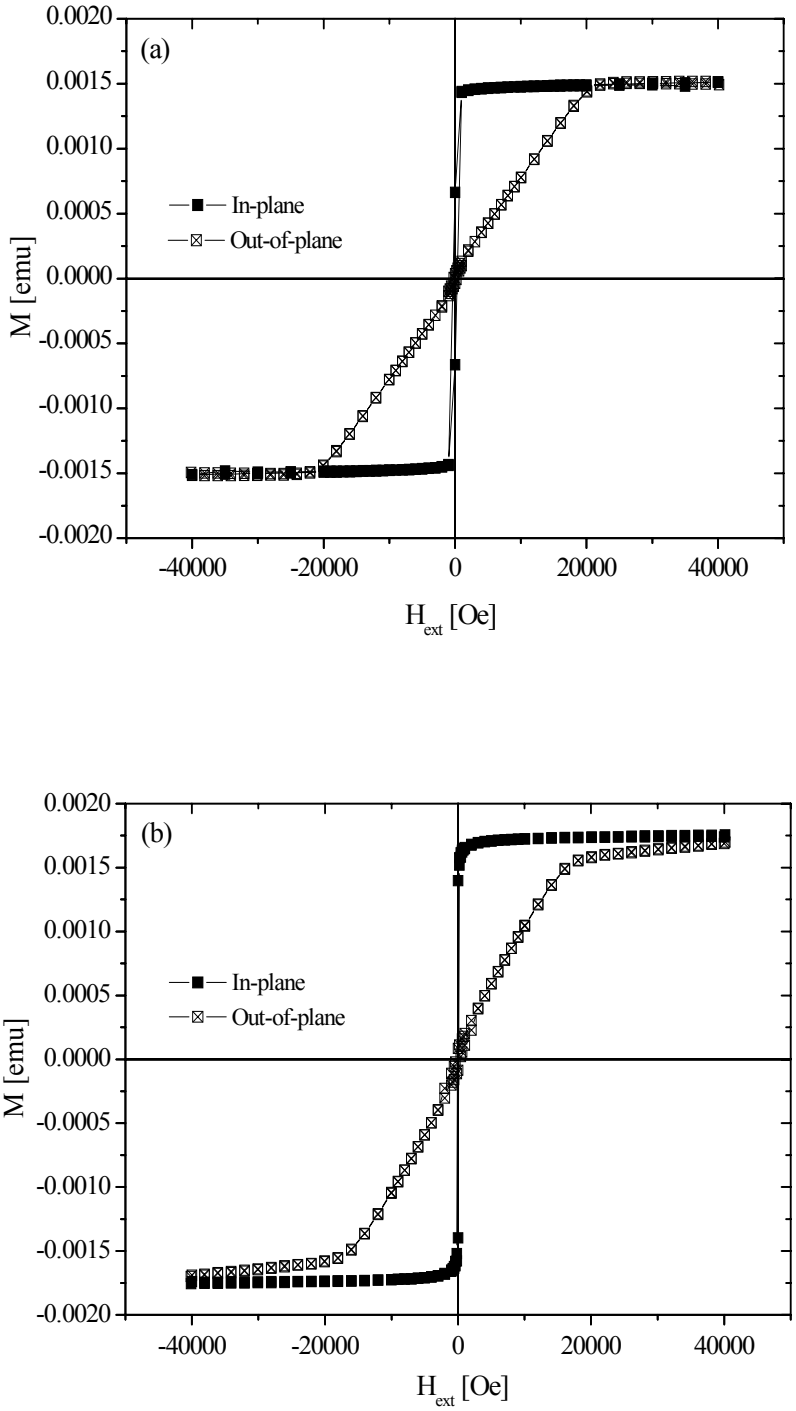

Fig. 8.6 Hysteresis loops measured at 40 K : (a) (Pt 54 Å / Fe 64 Å) × 5 / MgO multilayer and (b) (Pt 14 Å / Fe 11 Å) × 21 / MgO multilayer. These mutilayers result in the films of nominal compositions of $Fe_{54}Pt_{46}$ and $Fe_{50}Pt_{50}$, respectively.

8.2 $L1_0$-FePt monolayers

By heat-treating the multilayer precursor films ordered $L1_0$-FePt films were produced. The films had different elemental layer thicknesses to control the final composition. The different $L1_0$-FePt monolayers which have been produced are listed in Table 8.3. The annealing conditions are also shown in the table. Depending on the nominal composition the degree of texture can be changed from isotropic to epitaxial behavior.

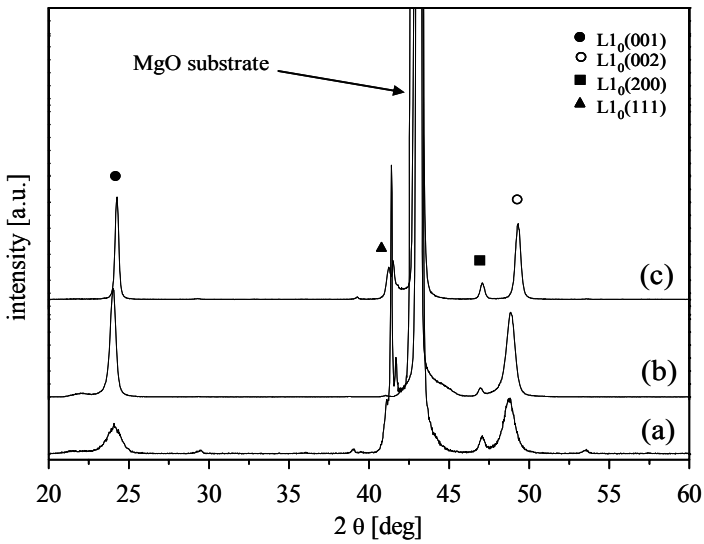

Fig. 8.7 XRD results for the (Pt 14 Å / Fe 13 Å) × 20 on MgO substrate annealed for 240 min at different temperatures: (a) 600 ºC , (b) 700 ºC and (c) 800 ºC. This multilayer will result in the film of the nominal composition of $Fe_{54}Pt_{46}$.

In the experiments, the optimal annealing temperature for formation of the ordered $L1_0$-FePt ordered alloy from the Fe/Pt multilayers was found to be 700 ºC. Fig. 8.7 shows the X-ray results for the (Pt 14 Å / Fe 13 Å) × 20 multilayers on a MgO (001) substrate annealed for 240 min at different temperatures. After annealing at 600º C only a weak (001) superlattice peak is visible. By increasing the annealing temperature to 700 ºC the XRD profiles exhibit a strong (001) superlattice peak. The existence of the strong (001) superlattice peak indicates the complete phase transition into the fct ordered alloy. When the annealing temperature is 800 ºC, the (200) peak intensity from grains with the tetragonal *c*-axes aligned in-plane direction becomes larger. This change is due to the grain growth after formation of orderd $L1_0$-FePt phase.

The growth of grains oriented in the (200) plane is not desirable for a perpendicular magnetic anisotropy of $L1_0$-FePt films, and therefore the annealing treatments of all multilayer films were performed at 700 ºC.

Nominal composition	Annealing temperature [º C]	Annealing time [min.]	Measured composition	Nominal thickness [nm]	Measured thickness [nm]	Degree of texture
$Fe_{50}Pt_{50}$	700	120	-	52	72.5	isotropic
$Fe_{50}Pt_{50}$	700	240	$Pt_{53.1}Fe_{46.9}$	52	-	isotropic
$Fe_{50}Pt_{50}$	700	660	$Pt_{53.7}Fe_{46.3}$	52	65.5	isotropic
$Fe_{57}Pt_{43}$	700	120	-	53	-	partially anisotropic
$Fe_{57}Pt_{43}$	700	240	$Pt_{43.6}Fe_{56.4}$	53	-	partially anisotropic
$Fe_{54}Pt_{46}$	700	120	-	54	-	partially anisotropic
$Fe_{54}Pt_{46}$	700	240	$Pt_{51.2}Fe_{48.8}$	54	-	partially anisotropic
$Fe_{60}Pt_{40}$	700	10	$Pt_{39.3}Fe_{60.7}$	54	62.49	epitaxial
$Fe_{60}Pt_{40}$	700	240	$Pt_{39.3}Fe_{60.7}$	54	64.38	epitaxial
$Fe_{60}Pt_{40}$	700	660	-	54	-	epitaxial
$Fe_{60}Pt_{40}$	700	1440	-	54	67.90	epitaxial
$Fe_{60}Pt_{40}$	700	10	-	60	-	epitaxial
$Fe_{60}Pt_{40}$	700	240	-	60	-	epitaxial
$Fe_{60}Pt_{40}$	700	10	-	27	-	epitaxial
$Fe_{60}Pt_{40}$	700	10	-	7.5	-	epitaxial
$Fe_{53}Pt_{47}$	700	10	-	27	34.5	epitaxial
$Fe_{53}Pt_{47}$	600	10	-	27	33.5	epitaxial
$Fe_{53}Pt_{47}$	700	10	-	15	19.7	epitaxial
$Fe_{53}Pt_{47}$	600	10	-	15	19.7	epitaxial

Table 8.3 $L1_0$-FePt monolayers which have been produced in this thesis. The compositions have been determined by energy dispersive X-ray analysis (EDX) and the thicknesses have been determined by X-ray reflectivity (XRR). Depending on the nominal composition the degree of texture can be changed from isotropic to epitaxial behavior.

8.2.1 Films with isotropic magnetization behavior

Films with nominal compositions of $Fe_{50}Pt_{50}$ show an isotropic behavior of the hysteresis loop, i.e. for fields applied parallel and perpendicular to the film plane, the hysteresis loops look similar. These isotropic magnetic properties are due to the formation of grains in the film with random orientation of the tetragonal *c*-axis. The polycrystalline film structure occurs already in the as-deposited state as presented in Chapter 8.1. By the annealing treatment these multilayer grains are transformed to ordered $L1_0$-FePt grains with different orientations of the easy axis. In this section, the results of the microstructural analysis of the films obtained by TEM and XRD, and the magnetic hysteresis loops measured by SQUID will be described. From the temperature dependence of the coercivity the microstructural parameters are determined.

8.2.1.1 Microstructure

The formation of the ordered $L1_0$-FePt phase in isotropic $Fe_{50}Pt_{50}$ films was investigated by in-situ TEM during heating the film. The initial state of the film is the polycrystalline multilayer structure shown in Fig. 8.5. Fig. 8.8a and Fig. 8.8b show the structural changes during heating up to 370 ºC and 620 ºC. Compared to the as deposited multilayers in Fig. 8.5 the multilayer structures in the grains disappear by heating the film up to 370 ºC. The high-resolution image clearly shows the grain boundaries. At the higher temperature of 620 ºC, in the grain boundary structure a triple junction point of three grains appears. (Fig. 8.8b).

Additional TEM investigations in cross sectional and planar view have been performed on the $L1_0$-$Fe_{50}Pt_{50}$ films which were heat-treated before the TEM investigation. The cross-sectional dark-field TEM image (Fig. 8.9) clearly shows an image contrast of grains which are extended over the whole thickness of the film (Fig. 8.9a). The diffraction pattern in Fig. 8.9b is related to the dark field image. Here the reciprocal lattice of the MgO substrate and the ordered $L1_0$-FePt alloy are indexed. The diffraction spots of the $L1_0$-FePt phase are not aligned along the spots resulting from the MgO substrate. This means that the $L1_0$-FePt film is not epitaxially grown, and grains with random orientation of the *c*-axis exist. Fig. 8.10a shows the planar TEM image in the bright-field mode from which the grain size distribution and grain shape can be analyzed. According to the grain-size distribution in Fig. 8.10b the average grain size is found to be 72.5 ± 26.1 nm. The grain shape is polyhedral and the grains show sharp edges.

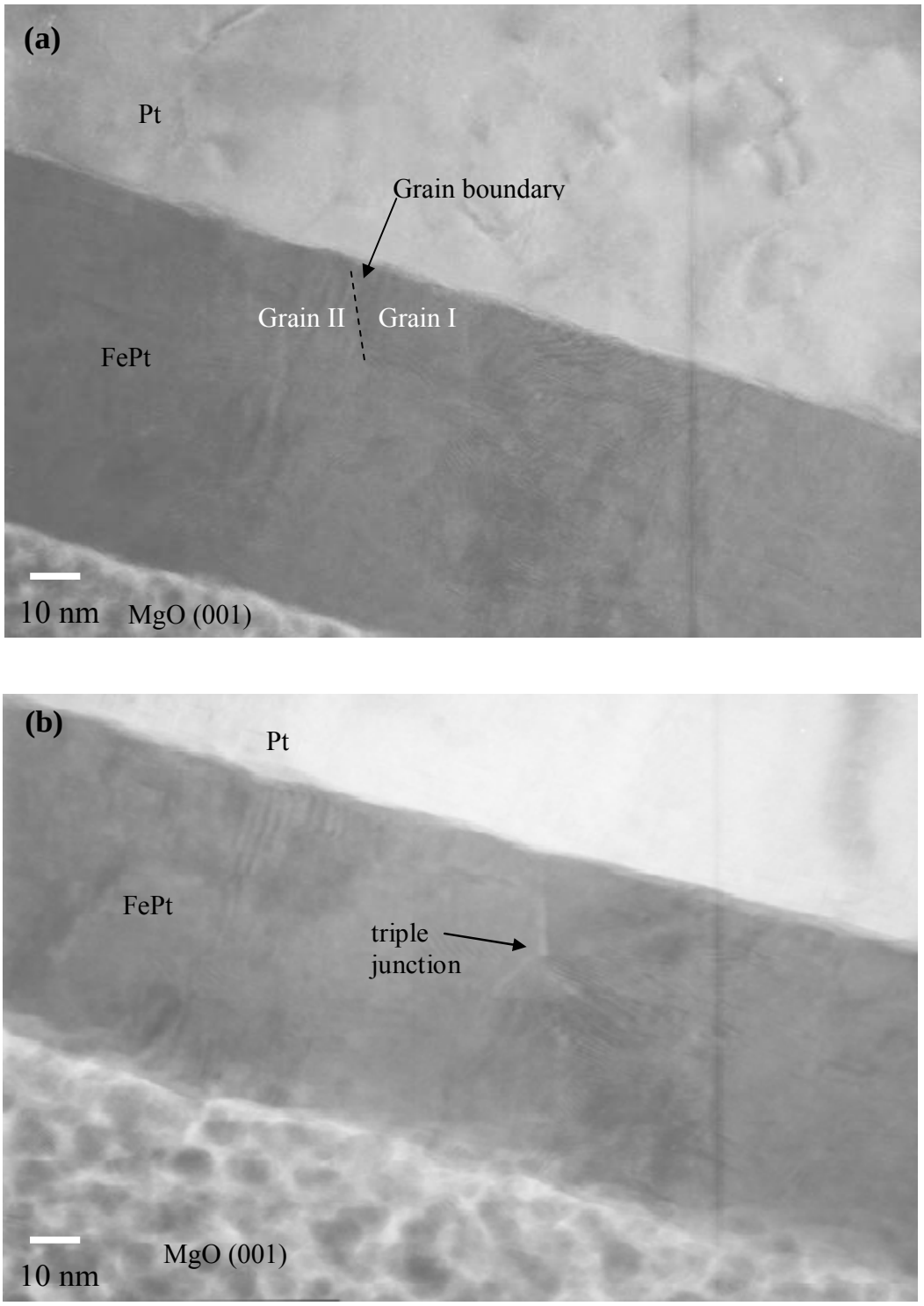

Fig 8.8 In-situ high resolution TEM of a (Pt 14 Å / Fe 11 Å)×21/MgO multilayer resulting in $L1_0$-$Fe_{50}Pt_{50}$ after heat treatment: (a) image after heating to 370 ºC, and (b) image after heating to 620 ºC. The arrow indicates a triple junction of grains.

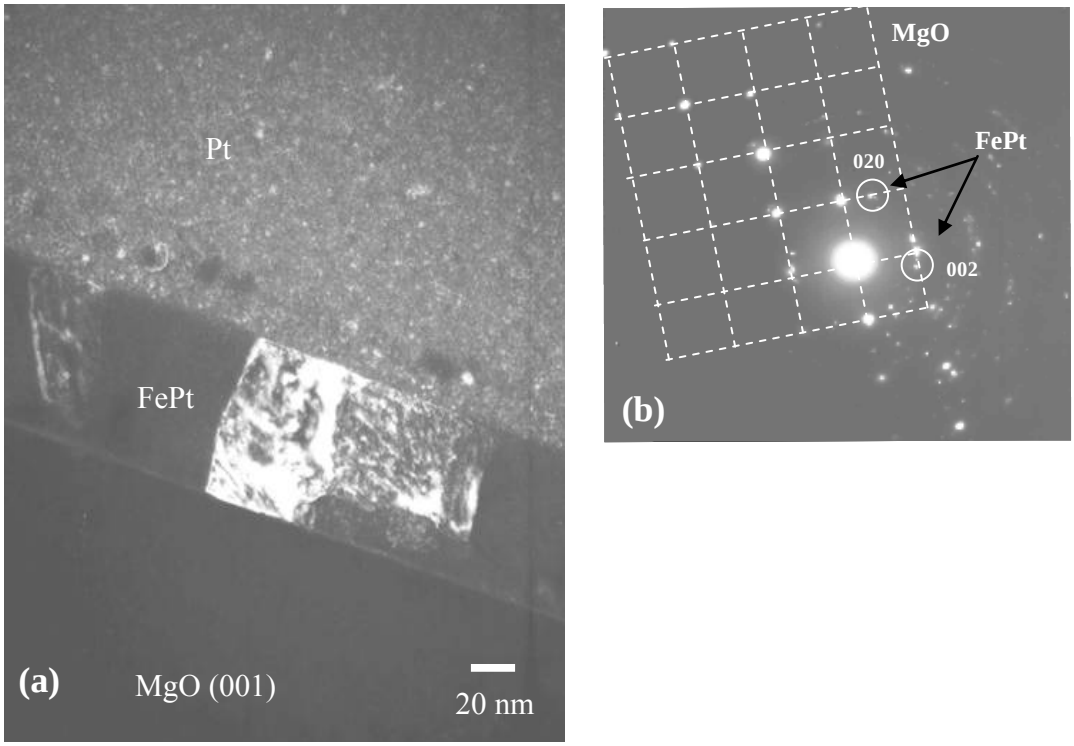

Fig 8.9 Cross sectional TEM view for a $L1_0$-$Fe_{50}Pt_{50}$ film heat-treated at 700 ºC for 120 min (precursor : (Pt 14 Å / Fe 11 Å)×21/MgO): (a) Dark-field image, (b) Selected-area diffraction pattern.

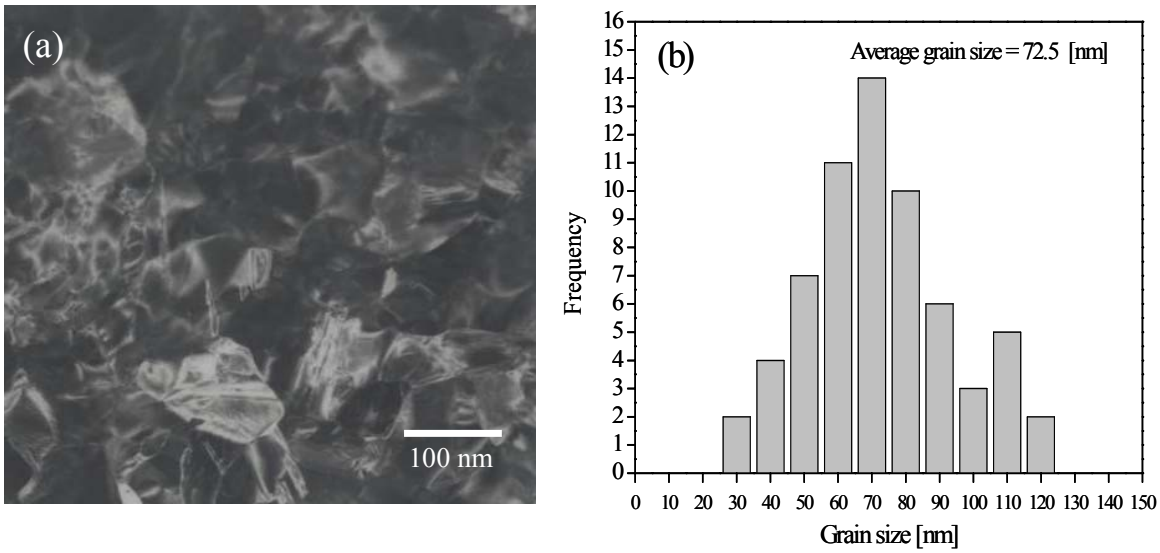

Fig 8.10 Planar TEM view of a $L1_0$-$Fe_{50}Pt_{50}$ film heat-treated at 700 ºC for 120 min (precursor: (Pt 14 Å / Fe 11 Å)×21/MgO): (a) Bright-field image, (b) Grain-size distribution of the grains of the bright-field image.

In Fig. 8.11 the X-ray diffraction spectrum and the contour plots of the pole figure intensity of the ordered $L1_0$-$Fe_{50}Pt_{50}$ film which has been investigated by TEM are shown. In Fig. 8.11a the diffraction peaks of $L1_0$-FePt (111) and (200) planes appear which confirms the polycrystalline film structure. In the light pole figure plot shown in Fig. 8.11b which results from the $L1_0$-FePt (001) diffraction peak of Fig. 8.11a the high intensity peaks of $L1_0$-FePt (200) planes are detected at an angle of 90º. In the right (201) pole figure of Fig. 8.11b, which has been obtained by rotating the goniometer by 64.8 º, the (001) and (111) peaks are visible.

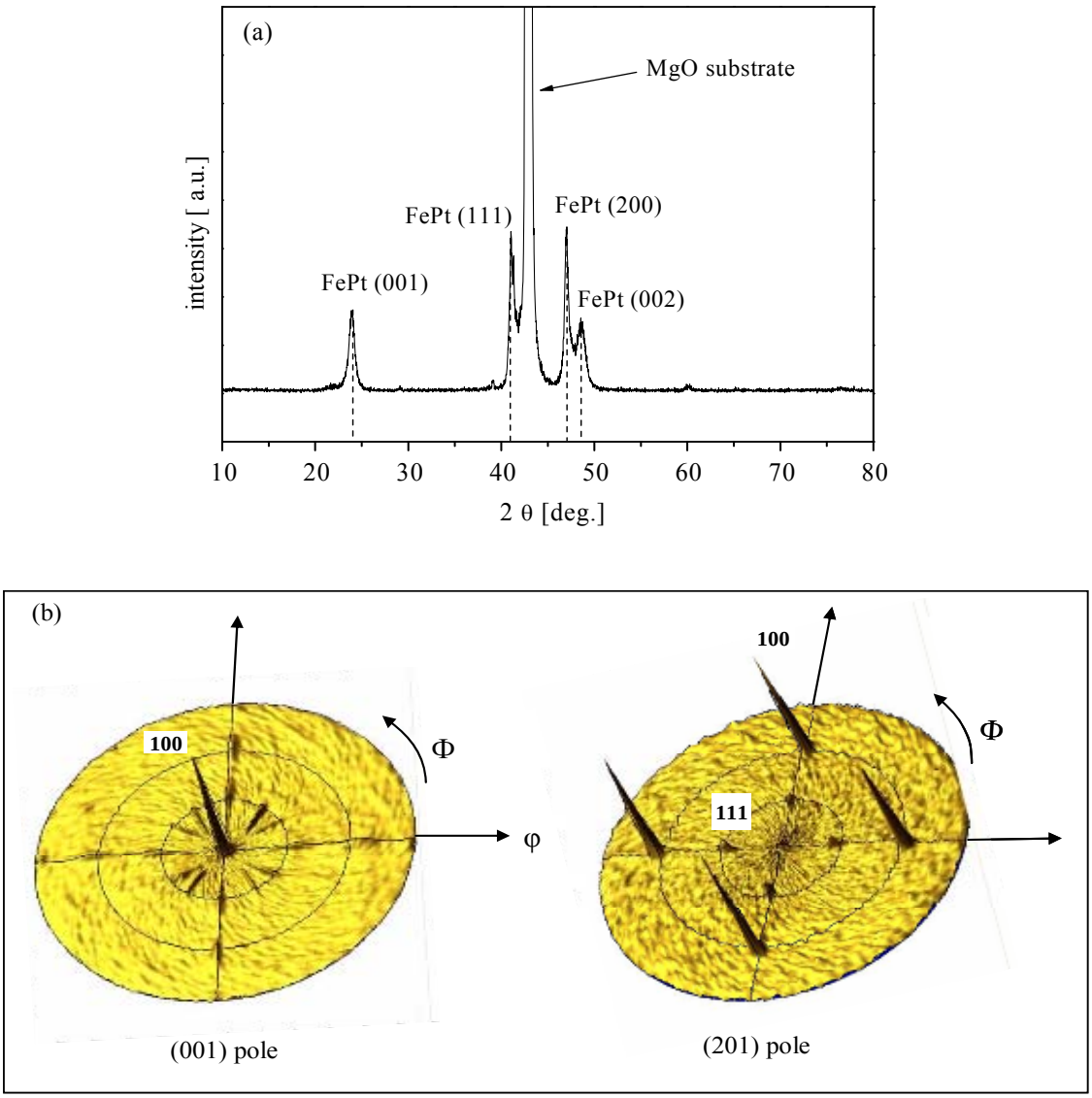

Fig. 8.11 XRD results for the $L1_0$-$Fe_{50}Pt_{50}$ film annealed at 700 °C for 120 min (precursor: (Pt 14 Å / Fe 11 Å)×21/MgO): (a) θ-2θ scan, (b) pole figure plots for (001) and (201) peaks.

8.2.1.2 Magnetic properties

The magnetic hysteresis loops with in and out-of-plane field direction show the isotropic magnetization behavior of the $L1_0$-$Fe_{50}Pt_{50}$ film (Fig. 8.12). After annealing at 700 °C for 120 min the elemental Fe and Pt layers were fully transformed into the ordered $L1_0$-phase with polycrystalline structure, in which the uniaxial tetragonal *c*-axes of the single-domain grains are randomly distributed. Therefore, the hysteresis loops measured at 40 K along in- and out-of-plane direction are nearly the same. The remanence amounts to approximately half of the saturation polarization and the large coercivity of $\mu_0 H_c$= 0.9 T can be attributed to the single-domain particles of the polycrystalline structure.

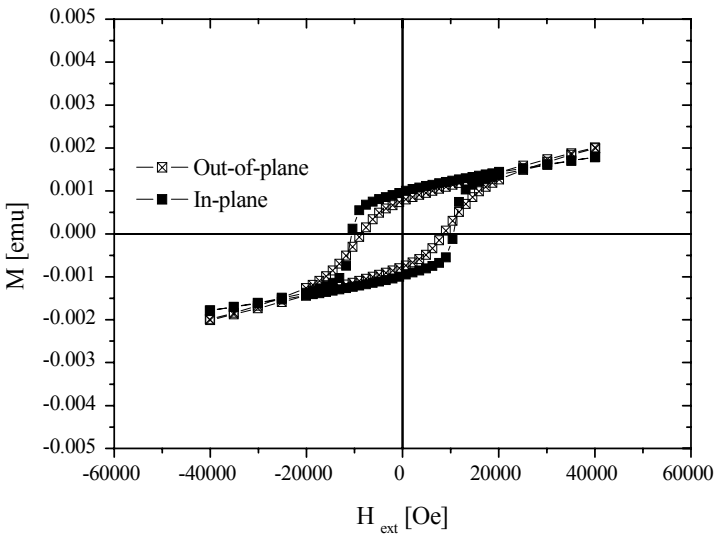

Fig. 8.12 Magnetic hysteresis loops measured at 40 K for a $L1_0$-$Fe_{50}Fe_{50}$ film after annealing at 700 °C for 120 min (precursor: (Pt 14 Å / Fe 11 Å)×21/MgO).

Fig. 8.13a and Fig. 8.13b show the hysteresis loops of the isotropic $L1_0$-$Fe_{50}Pt_{50}$ films after annealing at 700 ºC for 10 min and 240 min, respectively. With increasing annealing time the coercivity increases from 0.5 T (annealing time: 10 min) to 1.1 T (annealing time: 240 min). A further increase of the annealing time leads to a decrease of the coercivity. From Fig. 8.13 it becomes also obvious that for annealing times larger than 120 min the sample changes its fully isotropic behavior to a partially textured one.

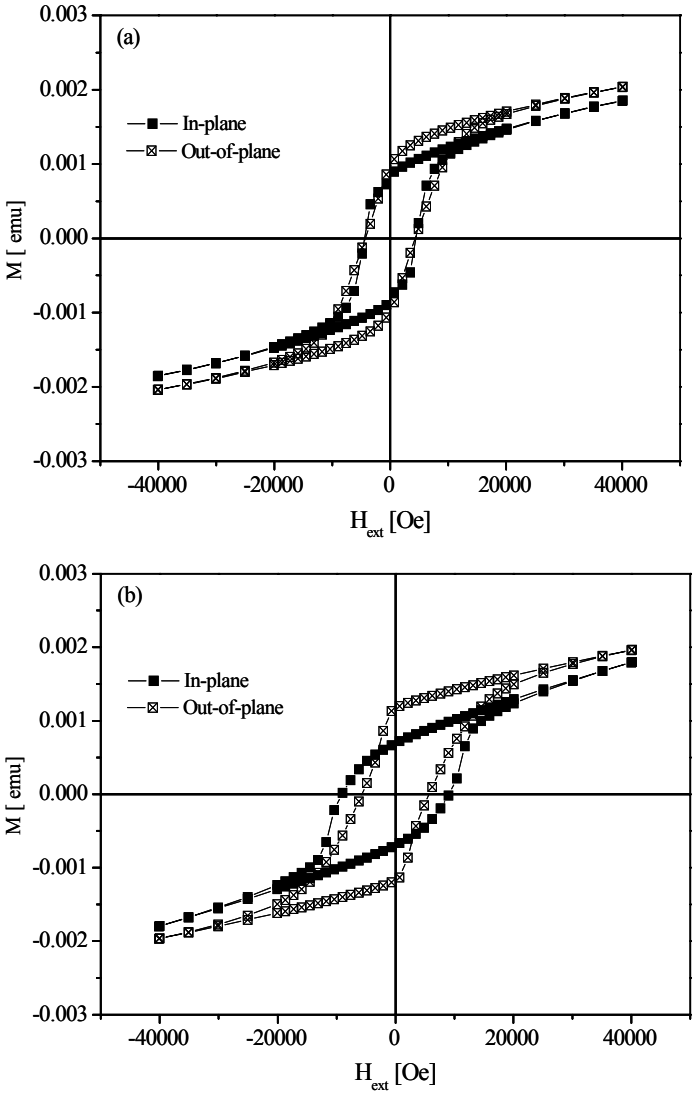

Fig. 8.13 Magnetic hysteresis loops measured at 40 K for a $L1_0$-$Fe_{50}Fe_{50}$ film (precursor: (Pt 14 Å / Fe 11 Å) ×21/MgO) after annealing at 700 °C: (a) for 10min, and (b) for 240 min.

8.2.1.3 Analysis of the coercivity mechanism with microstructural parameters

The microstructural parameters of the $L1_0$-$Fe_{50}Pt_{50}$ film annealed at 700 ºC for 120 min can be determined from the temperature dependence of the coercivity $\mu_0 H_c$. $\mu_0 H_c$ (T) is plotted in Fig. 8.14. For polycrystalline magnets with an isotropic magnetization behavior the temperature dependence of the coercivity is given by

$$\frac{\mu_0 H_c(T)}{J_s(T)} = \mu_0 \frac{K_1(T)}{J_s^2(T)} \cdot \alpha - N_{eff} \,. \tag{8.1}$$

The microstructural parameters α and N_{eff} provide quantitative information about the influence of the microstructure on the coercive field $\mu_0 H_c$ as described in Chapter 2. To determine the microstructural parameters from eq. (8.1) the temperature dependence of the intrinsic magnetic properties J_s(T) and K_1(T) must be known. J_s(T) and K_1(T) can be determined from the hysteresis loops measured at different temperatures. The determination of $J_s(T)$ requires the exact volume of a ferromagnetic film. Thus the volume of the $L1_0$-$Fe_{50}Pt_{50}$ film was determined by measuring the thickness of the film using by X-ray reflectometry. Fig. 8.15 shows the reflectivity spectrum measured at small angles in comparison with the fitted spectrum.

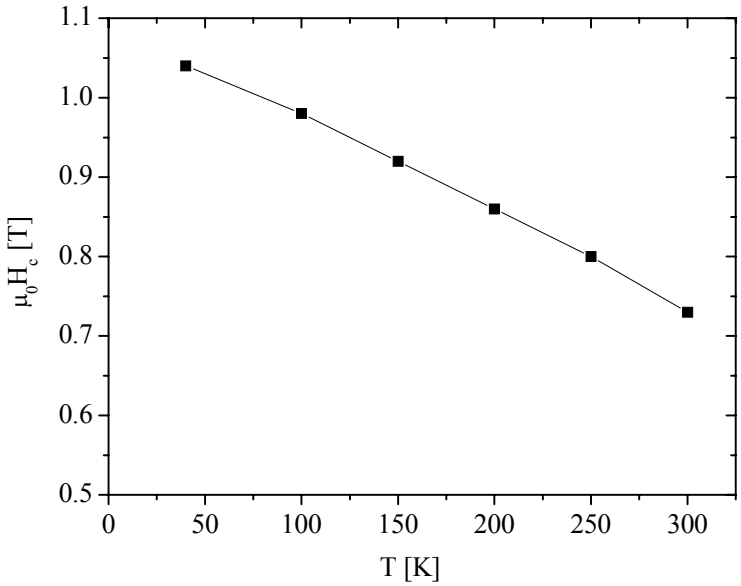

Fig. 8.14 Temperature dependence of $\mu_0 H_c$ for the isotropic $L1_0$-$Fe_{50}Pt_{50}$ film annealed at 700 ºC for 120 min (precursor : (Pt 14Å / Fe 11Å) × 21 / MgO).

The fitting parameters yield the density and thickness of the alloy film layer. The measured thickness and density of the $L1_0$-$Fe_{50}Pt_{50}$ film with isotropic magnetization behavior are 65.5 nm and 13.8 g/cm^3, respectively.

It is rather difficult to correct the diamagnetism of the MgO (001) substrate exactly since the MgO is very hygroscopic so that the absorbed water in MgO during sample handling can change

the diamagnetic susceptibility of MgO. Therefore the room temperature spontaneous polarization value of the stoichiometric $L1_0$-$Fe_{50}Pt_{50}$ alloy has been assumed to be equal to the literature value of J_s = 1.43 T [5]. Under this assumption the diamagnetism of MgO which is temperature independent could be determined. The determined value of 3.90×10^{-9} has been subtracted from the hysteresis loops measured at 300 K and 250 K to receive J_s at 250 K. By means of J_s (300 K) and J_s (250 K), and the Bloch $T^{3/2}$ law in eq. (6.16) a linear plot of J_s versus $T^{(2/3)}$ is obtained as shown in Fig. 8.16 which can be extrapolated to low temperatures. From the extrapolation of the linear plot the J_s values at lower temperatures (200 K, 150K, 100K, and 40K) are received.

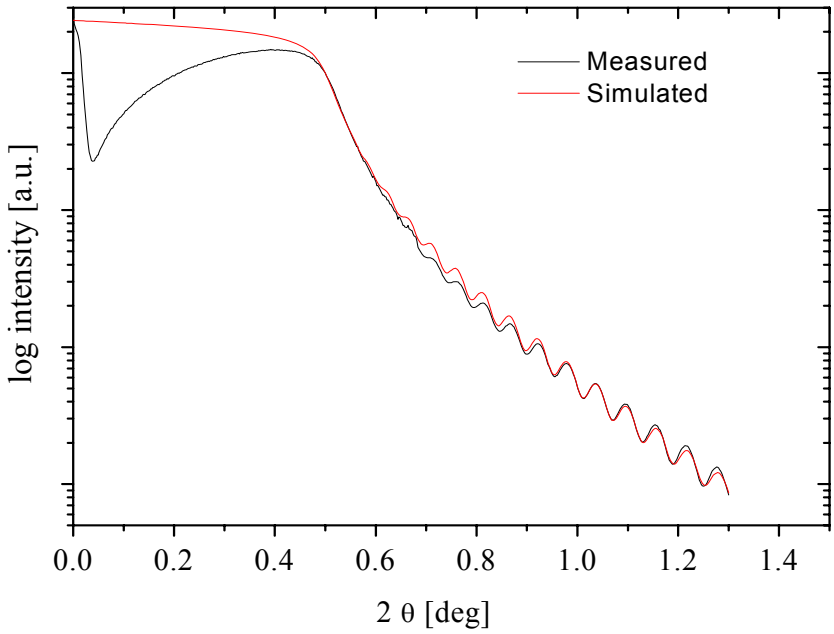

Fig. 8.15 X-ray reflectivity spectrum of a $L1_0$-$Fe_{50}Pt_{50}$ film after annealing at 700 ºC (precursor: (Pt 14 Å / Fe 11 Å)×21/MgO).

The values of $K_1(T)$ were obtained by fitting the measured hysteresis loops for the two different temperatures (300 K and 250 K) to the calculated loops using the program developed by Köhler [32]. Fig. 8.17 shows the result of the fit using the measured hysteresis loop at 300 K and a K_1 value of 4.60 MJ/m^3 as a fitting parameter.

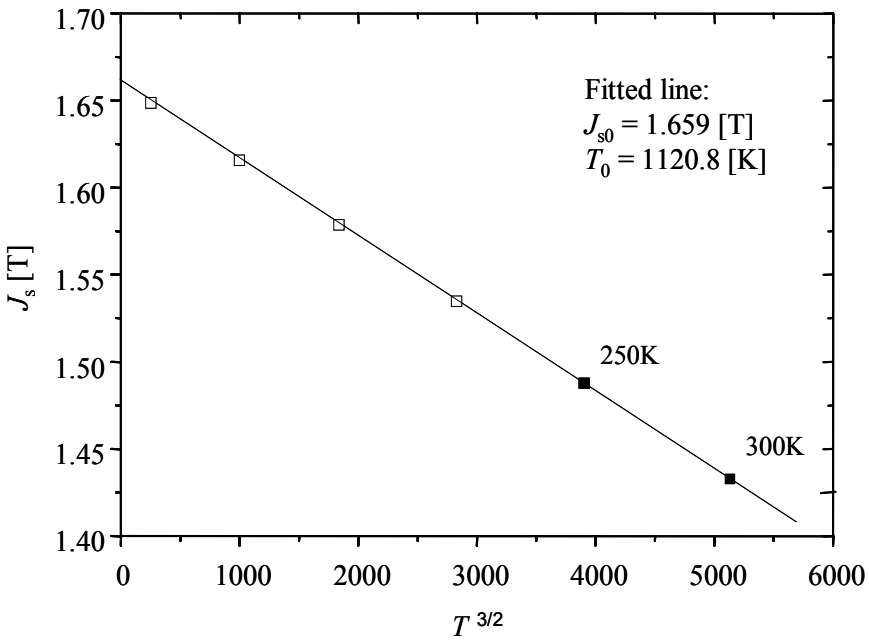

Fig. 8.16 Linear plot of J_s versus $T^{3/2}$ for the $L1_0$-$Fe_{50}Pt_{50}$ film. J_s has been measured at 250 K and 300 K (filled squares).

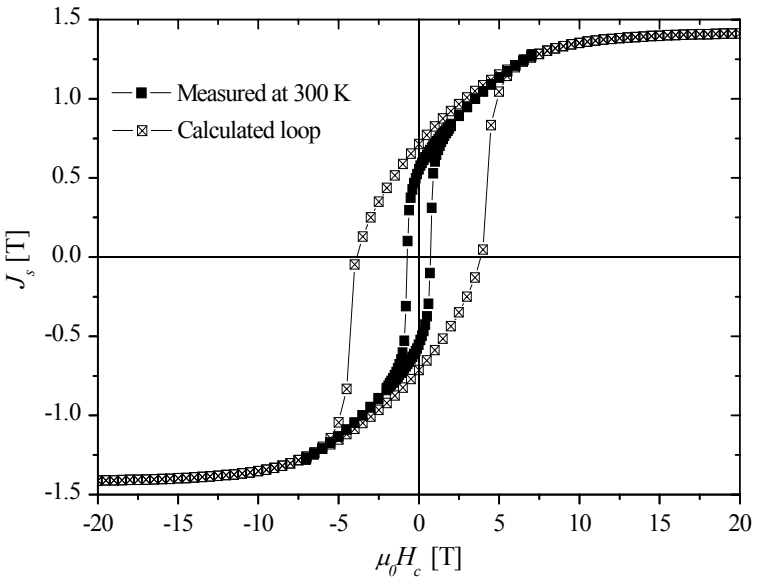

Fig. 8.17 Result of fitting the hysteresis loop of the isotropic $L1_0$-$Fe_{50}Pt_{50}$ film measured at 300 K, with $K_1 = 4.60$ and $J_s = 1.43$ as fitting parameters.

By the same procedure a K_1 value of K_1 = 5.13 MJ/m^3 is obtained for T = 250 K. Within the framework of thermal fluctuations of magnetic moments, where the temperature dependences of K_1 and J_s are expressed as [76]

$$\frac{K_1(T)}{K_1(0)} = \left[\frac{J_s(T)}{J_s(0)}\right]^m, \tag{8.2a}$$

and by taking the logarithm, eq. (8.2a) becomes

$$\text{Log } K_1(\text{T}) = \text{m} \cdot \text{Log } J_s(\text{T}) + \text{const.} \tag{8.2b}$$

Under the assumption that eq. (8.2b) is valid, Log K_1 is plotted versus Log J_s in Fig. 8.18 for T = 250 K and T = 300 K and the resulting line with slope m = 2.88 and y-axis intersection 0.21392 is extended to lower temperatures to obtain the anisotropy constants.

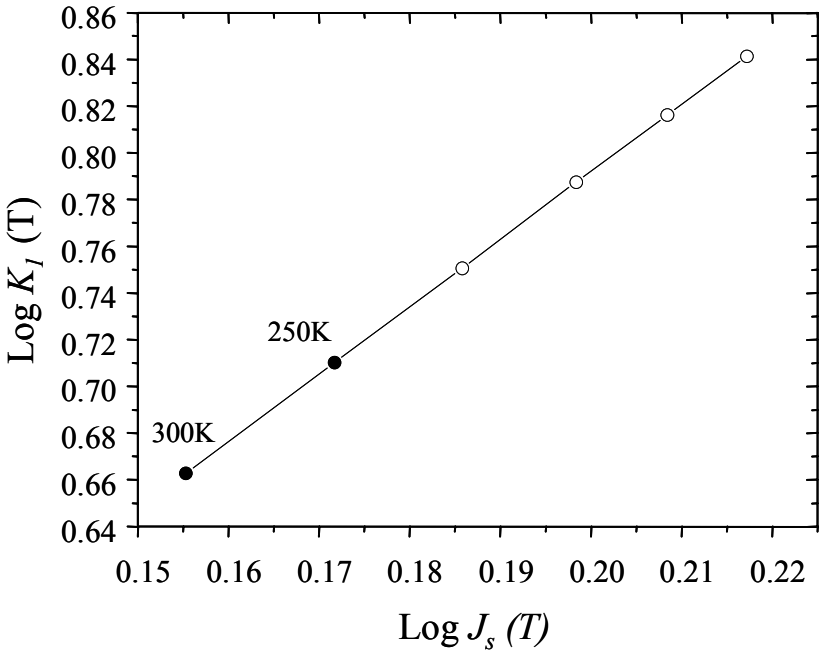

Fig. 8.18 The log-log plot of $K_1(T)$ versus $J_s(T)$ for the isotropic $L1_0$-$Fe_{50}Pt_{50}$ alloy film annealed at 700 ºC for 120 min (precursor: (Pt 14 Å/ Fe 11 Å) × 21 / MgO).

The results obtained for the temperature dependence of $J_s(T)$ and $K_1(T)$ are plotted in Fig. 8.19 and Fig. 8.20 for the isoptropic $L1_0$-$Fe_{50}Pt_{50}$ film annealed at 700 ºC for 120 min.

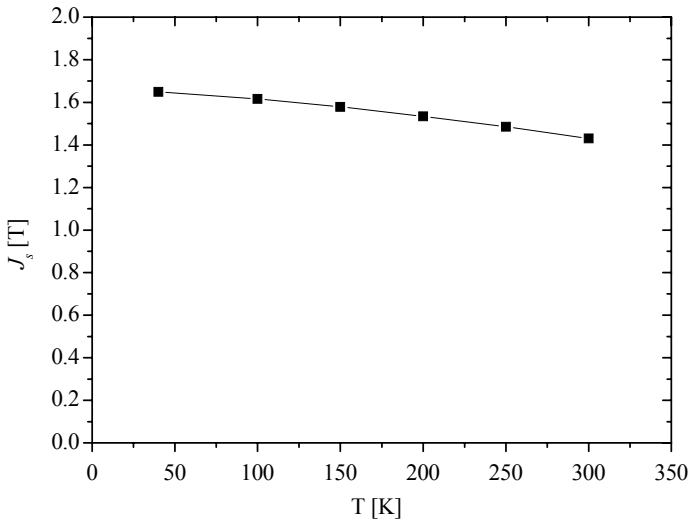

Fig. 8.19 Temperature dependence of J_s for the isotropic $L1_0$-$Fe_{50}Pt_{50}$ film annealed at 700 ºC for 120 min (precursor : (Pt 14Å / Fe 11Å) × 21 / MgO).

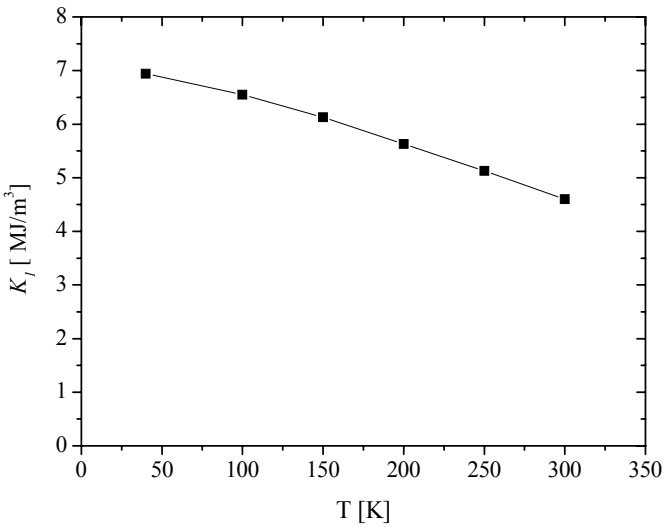

Fig. 8.20 Temperature dependence of K_1 for the isotropic $L1_0$-$Fe_{50}Pt_{50}$ film annealed at 700 ºC for 120 min (precursor : (Pt 14Å / Fe 11Å) × 21 / MgO).

Additionally, the temperature dependence of the exchange constant *A(T)* was obtained from the relation in eq. (6.14) using the $J_s(T)$ values and T_0 = 1120.8 K determined in the above analyses. Fig. 8.21 represents the values of the exchange constant *A* as a function of the temperature.

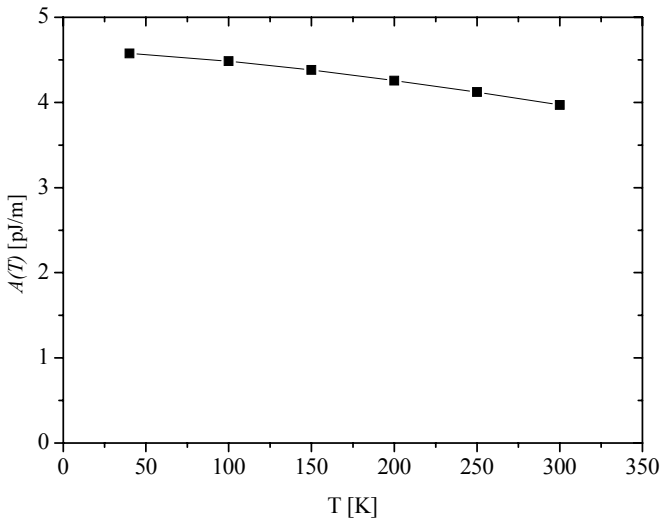

Fig . 8.21 Temperature dependence of the exchange constant A for the isotropic $L1_0$-$Fe_{50}Pt_{50}$ film annealed at 700 ºC for 120min (precursor : (Pt 14Å / Fe 11Å) × 21 / MgO).

Table 8.5 summarizes the temperature dependences of $\mu_0 H_c$ (Fig. 8.14) and of the intrinsic magnetic properties J_s, K_1, and A as well as $\mu_0 H_c/J_s^2$ and $\mu_0 H_c/J_s$ required for the determination of the microstructural parameters according to eq. (8.1).

T [K]	$\mu_0 H_c$ [T]	K_1 [MJ/m^3]	J_s [T]	$\mu_0 K_1/J_s^2$	$\mu_0 H_c/J_s$	A [pJ/m]
40	1.04	6.94	1.65	3.21	0.631	4.58
100	0.98	6.55	1.62	3.16	0.606	4.49
150	0.92	6.13	1.57	3.09	0.583	4.38
200	0.86	5.63	1.53	3.01	0.560	4.26
250	0.80	5.13	1.48	2.93	0.539	4.12
300	0.73	4.60	1.43	2.83	0.510	3.97

Table 8.5 Temperature dependence of $\mu_0 H_c$, K_1, J_s, A, $\mu_0 K_1/J_s^2$ and $\mu_0 H_c/J_s$ for the isotropic $L1_0$-$Fe_{50}Pt_{50}$ film annealed at 700 ºC for 120 min (precursor: (Pt 14 Å / Fe 11 Å) × 21 / MgO).

With the temperature dependences of $\mu_0 H_c$, J_s, and K_1 listed in Table 8.5 $\mu_0 H_c/J_s$ versus $\mu_0 K_1/J_s^2$ can be plotted as shown in Fig. 8.22 to determine the microstructural parameters from the slope and y-axis intersection of the obtained straight line.

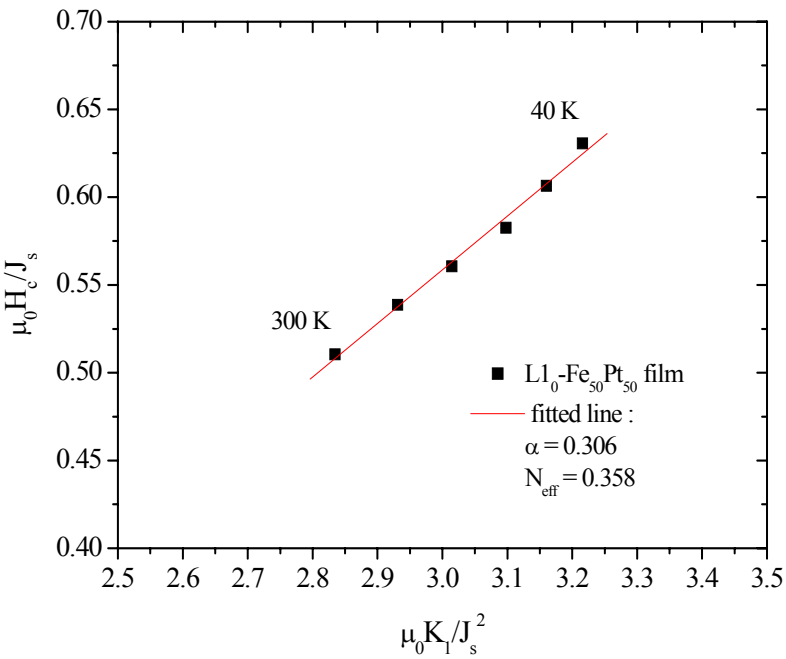

Fig 8.22 Microstructural parameters of the $L1_0$-$Fe_{50}Pt_{50}$ film with isotropic magnetization behavior.

The microstructural parameters obtained from the straight line in Fig 8.22 are α = 0.306 and N_{eff} =0.358. The value of α can be subdivided into α_K and α_{ex}. However, in case of the $L1_0$-FePt thin film, the α_K value is unknown, and the value of α = 0.306 has to be considered as a parameter including the effects of the structural defects (α_K) and the exchange coupling between neighboring grains (α_{ex}). N_{eff} = 0.358 is related to grains with sharp corners as shown in Fig 8.8 and Fig 8.9.

8.2.2 Partially anisotropic films

In Fig. 8.23 the hysteresis loops of the films with compositions of $Pt_{43}Fe_{57}$ (precursor: (Pt 14 Å / Fe 14 Å) × 19 / MgO) and $Pt_{46}Fe_{54}$ (precursor : Pt 14 Å / Fe 13 Å) × 20 / MgO) annealed at 700 °C for 240 min appear less isotropic compared to the films in Fig. 8.12 with composition

of $Pt_{50}Fe_{50}$ (precursor: (Pt 14 Å / Fe 14 Å) × 19 / MgO). From the X-ray diffraction spectrum in Fig 8.24 it was found that the peak intensities of (001) and (002) planes are stronger than those of (111) and (200) planes in $Pt_{46}Fe_{54}$ film. This means that the increased Fe content in the multilayers due to larger individual Fe layer thicknesses results in a microstructure with partly oriented grains on the MgO(001) substrate. With increasing Fe content the degree of texture increases.

8.2.3 Epitaxially grown anisotropic films

The multilayer films with nominal compositions of $Fe_{60}Pt_{40}$ of 60 nm thickness and $Fe_{53}Pt_{47}$ of 27 nm thickness indicate in the out of plane hysteresis loop a strong perpendicular magnetic anisotropy. This magnetic property is due to the alignment of the tetragonal c-axis along the direction perpendicular to the film plane. The multilayer stacks of the Fe and Pt layers are transformed into epitaxial films on a MgO(001) substrate by the annealing treatment. In this section the results of the microstructural characterization and the analyses for the magnetic properties will be described.

8.2.3.1 Microstructure

By heating (Pt 56 Å / Fe 64 Å) x 5 multilayer on a MgO (001) substrate in the in-situ TEM chamber, the formation mechanism of epitaxially grown $L1_0$–$Fe_{60}Pt_{40}$ was investigated (specimen number 5 in Table 8.1). The TEM image of the multilayer structure observed in the TEM at room temperature has been shown in Fig. 8.5. In Fig. 8.25 the cross-sectional views of the multilayer film are presented with increasing temperature from 380 ºC to 690 ºC. The MgO (001) substrate is visible at the bottom, and the polycrystalline Pt cover layer on top. With increasing temperature Fe atoms diffuse into the Pt layers. At 380 ºC small nuclei of the ordered $L1_0$-FePt phase are found in the Pt layers (Fig. 8.25a). The nuclei significantly grow in the Pt layers with consumption of Fe layers. No nuclei are found in the Fe layers during the in-situ annealing experiment. By holding the temperature at 380 ºC for one hour, the formation of the $L1_0$-phase results in additional spots in the Fourier transformed images in Fig. 8.25b. After heating up to 690 ºC a nearly complete intermixing of Fe and Pt and formation of $L1_0$-FePt has taken place. As the final microstructure of the film epitaxially grown layer without any grain boundaries was obtained.

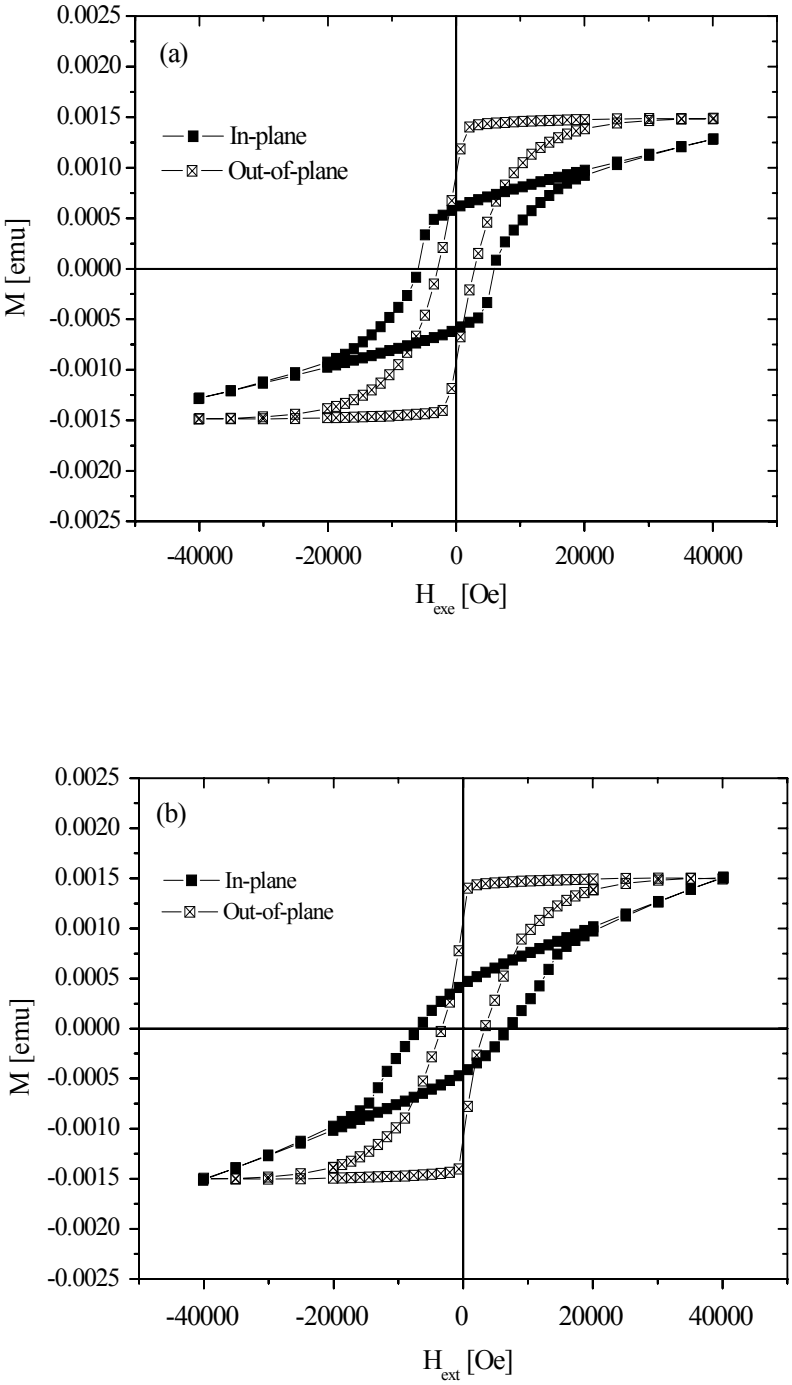

Fig. 8.23 Magnetic hysteresis loops measured at 40 K for ordered $L1_0$-FePt films after annealing at 700 °C for 240 min: (a) $Pt_{43}Fe_{57}$ film (precursor: (Pt 14 Å / Fe 13 Å)×20/ MgO) and (b) $Pt_{46}Fe_{54}$ film (precursor: (Pt 14 Å / Fe 11 Å)×21/ MgO).

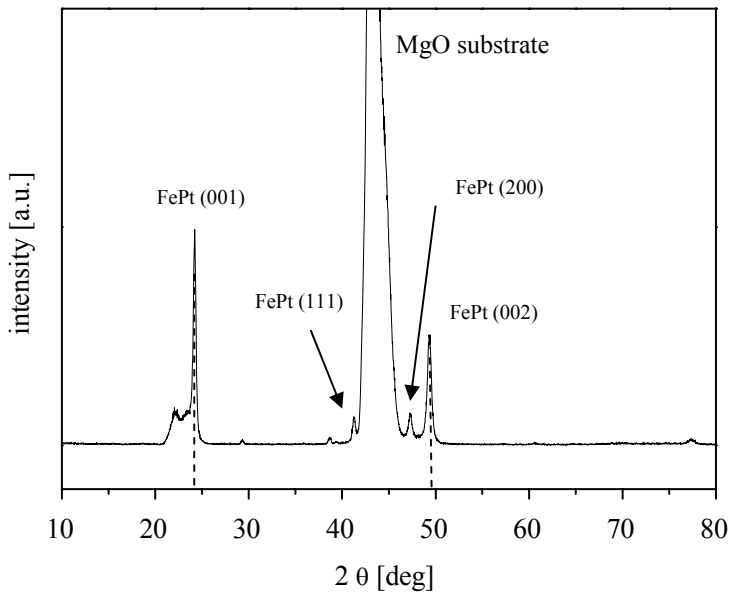

Fig. 8.24 X-ray diffraction spectrum (θ-2θ scan) of the$L1_0$-$Fe_{54}Pt_{46}$ film annealed at 700 ºC for 240 min (precursor: (Pt 14Å/ Fe 13Å) × 20 / MgO).

The cross-sectional TEM image of an epitaxially grown $L1_0$-$Fe_{53}Pt_{46}$ film of 15 nm thickness is shown in Fig. 8.26. The film has been prepared by annealing a (Pt 16 Å/ Fe 14 Å) × 5 multilayer grown on a MgO (001) substrate at 700 ºC for 10min. In the diffraction pattern of Fig. 8.26b the spots from $L1_0$-FePt are lying in array parallel to the spots resulting from the MgO substrate. The contrast in the film layer is due to the thickness effect of the TEM specimen. It was found that the film is an epitaxially grown single layer without misoriented grains.

The X-ray diffraction spectrum of the epitaxially grown $L1_0$-$Fe_{60}Pt_{40}$ film (precursor: (Pt 14 Å / Fe 16 Å) × 18 / MgO) with the nominal composition $Fe_{60}Pt_{40}$ is shown in Fig. 8.27a. The peaks appearing in the spectrum are FePt (001) and (002) and MgO (001). These peaks indicate the well-ordered $L1_0$-FePt structure of the epitaxially grown film with the *c*-axis aligned perpendicular to the film plane. To confirm the *c*-axis orientation of the $L1_0$- FePt film, pole figure measurements have been performed for two selected poles, (001) and (201). The two pole figure plots are shown in Fig. 8.27b, here only reflections from the (002) plane are visible, i.e. the multilayer film on MgO (001) has been successfully transformed into an ordered $L1_0$-$Fe_{60}Pt_{40}$ alloy film which is an epitaxially grown single layer.

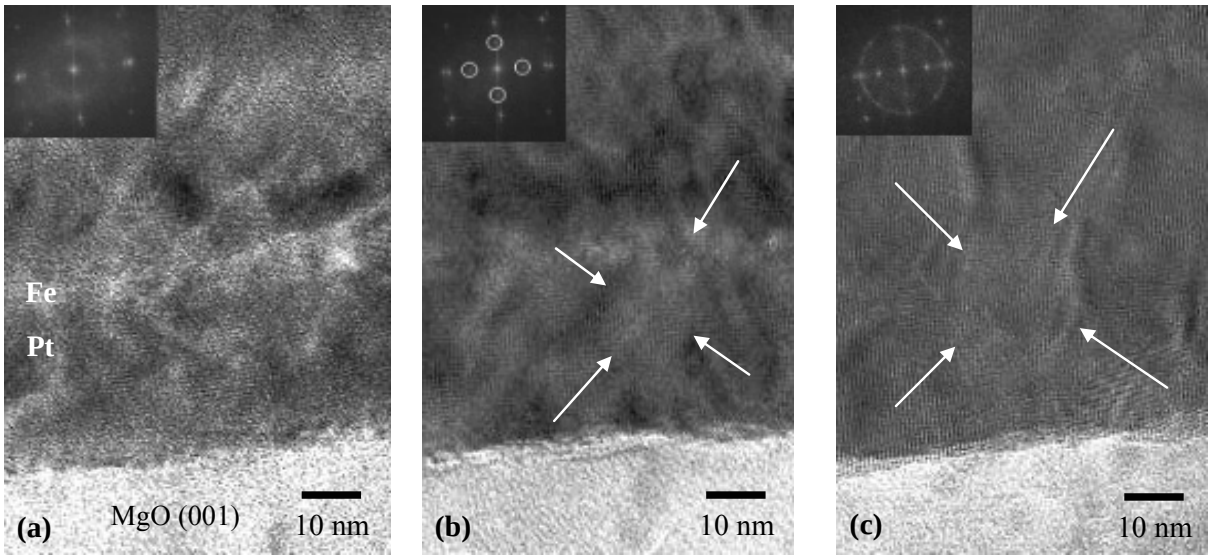

Fig. 8.25 Cross-sectional TEM images and Fourier transform of the images (inset) of the multilayer of (Pt 56 Å / Fe 64 Å) × 5 on MgO substrate during annealing at elevated temperature: (a) image at 380 ºC, (b) image at 380 ºC after one hour, (c) image at 690 ºC. The multilayers will finally result in a film of composition $Fe_{60}Pt_{40}$.

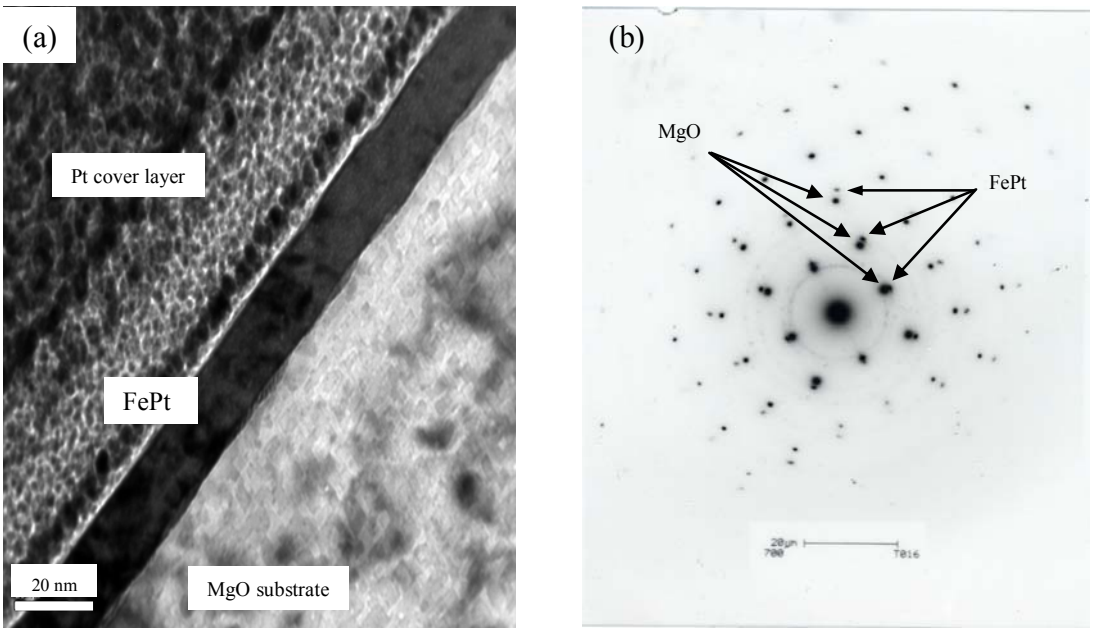

Fig. 8.26 Cross-sectional TEM image of a heat-treated (Pt 16Å/ Fe 14Å) × 5 multilayer at 700 ºC for 10 min :

(a) Bright-field image, (b) Selected-area diffraction pattern. This multilayer will finally result in the film of composition $Fe_{53}Pt_{47}$.

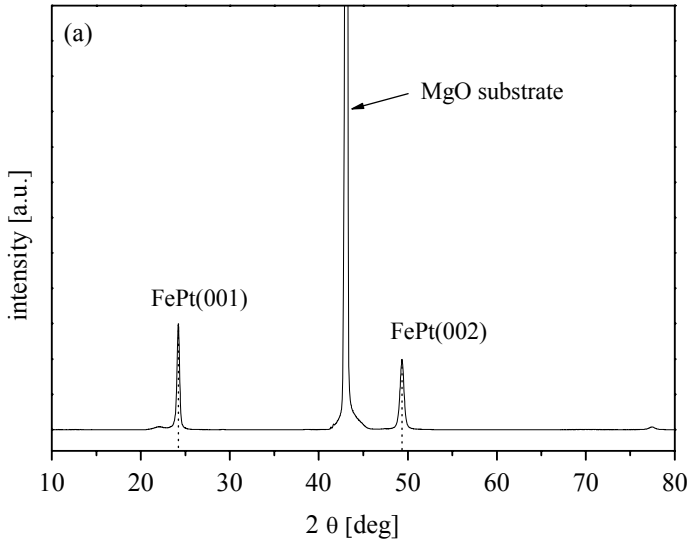

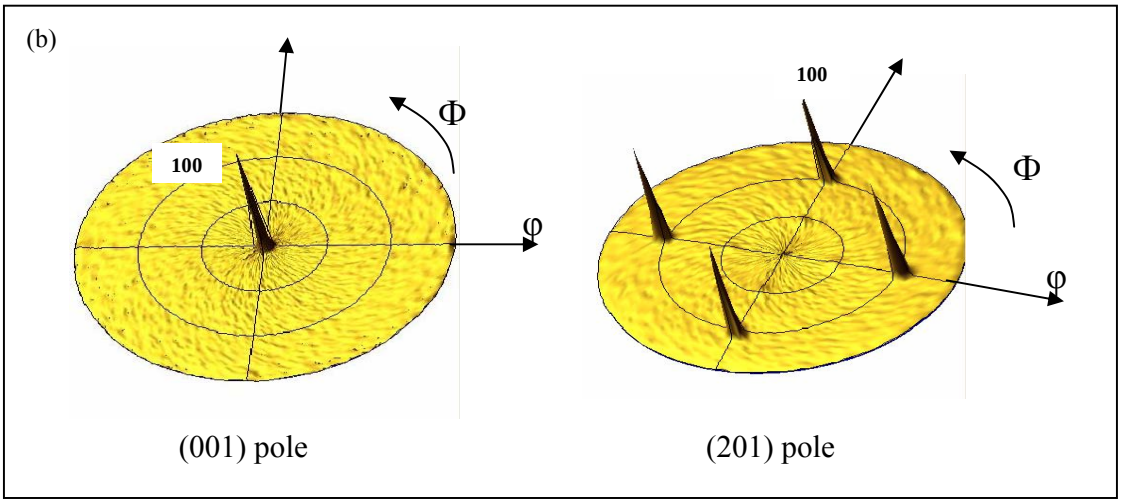

Fig. 8.27 XRD results for the $L1_0$-$Fe_{60}Pt_{40}$ film annealed at 700 °C for 120 min (precursor: (Pt 14 Å / Fe 16 Å)×18/MgO): (a) θ-2θ scan, (b) pole figure plots for (001) and (201) peaks.

8.2.3.2 Magnetic properties

The magnetic hysteresis loops of the epitaxially grown $L1_0$-$Fe_{53}Pt_{47}$ film (27 nm thickness) measured for an external field applied into the out-of-plane and in-plane direction are shown in Fig. 8.28. Clear differences between the out-of-plane and in-plane loops exist. In the out-of-plane loop the saturation is reached for an applied field of 1.2 T. By decreasing the applied field from 4 T the magnetization of the film remains saturated until the remanence is reached. In

contrast, the in-plane hysteresis loop exhibits a hard magnetic behavior and the magnetization cannot be saturated even in the 4 T field. The sudden drop of the magnetization in the out-of-plane loop is related to the spontaneous nucleation of domain walls parallel to the magnetic easy axis which is perpendicular to the film surface. The domains nucleate randomly and grow asymmetrically when the external field is reduced from the saturation field. The Kerr microscope images in Fig. 8.29 of the ordered $L1_0$-FePt alloy film show worm-like domains, which were observed in a similar form in FeTb films with a perpendicular magnetic anisotropy [77]. With increasing field the number of reversed domains increases.

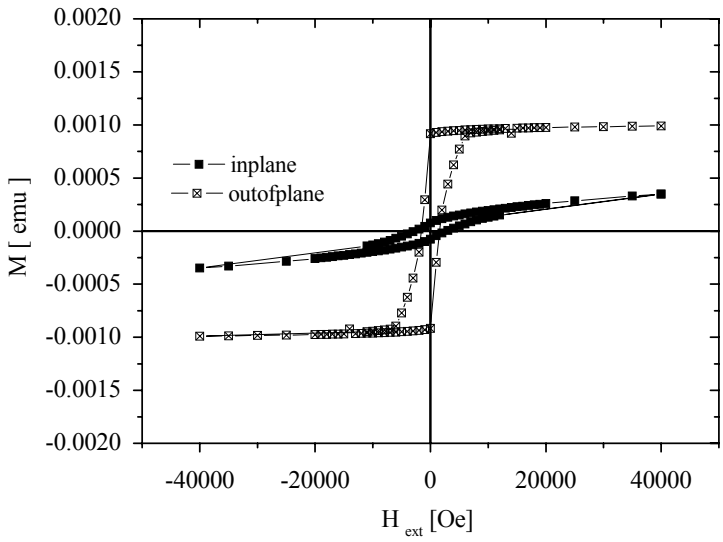

Fig. 8.28 Magnetic hysteresis loops measured at 40 K of the 27 nm thick $L1_0$-$Fe_{53}Pt_{47}$ film after annealing at 700 °C for 10 min (precursor: (Pt 16 Å / Fe 14 Å)×9/MgO).

For the 54 nm thick $L1_0$-$Fe_{60}Pt_{40}$ films, after heat-treatments of (Pt 14 Å / Fe 16 Å) ×18 multilayers on a MgO substrate were performed for different durations of time, the magnetization behavior of each film was investigated. The magnetic hysteresis loops are shown in Fig. 8.30. For an annealing time of 120 min the magnetic hysteresis loop (Fig. 8.30a) shows a perpendicular magnetic anisotropy implying that the ordering transition was completed. By increasing the annealing time to 240 min, the hysteresis loops does not change any more (Fig. 8.30b). For even longer annealing times the in-plane hysteresis loop encloses a larger area, however, the perpendicular anisotropy becomes weaker (Fig. 8.30c).

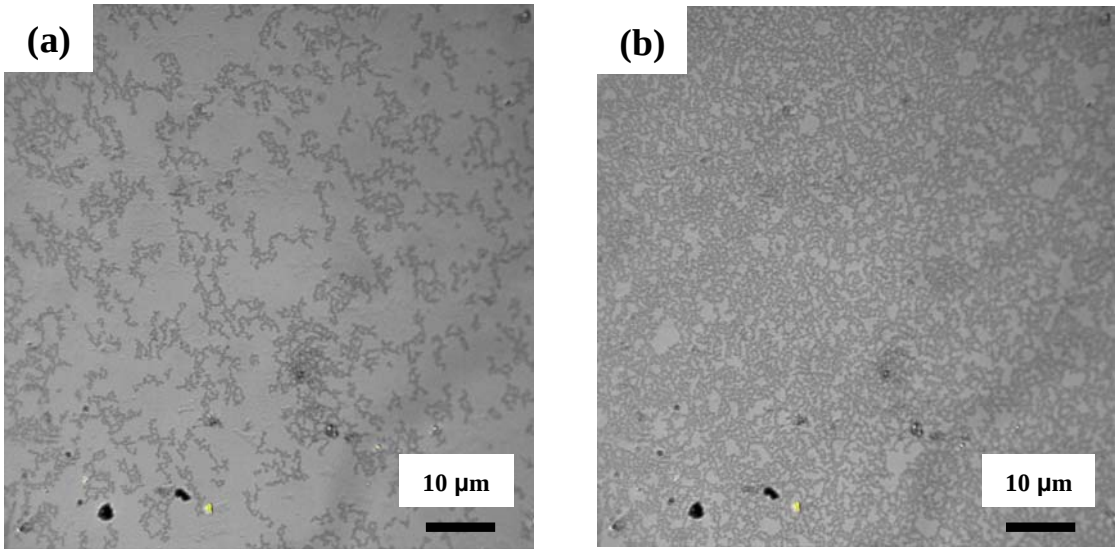

Fig. 8.29 Magneto-optical Kerr images of the $L1_0$-$Fe_{53}Pt_{47}$ film (27 nm thickness) of Fig. 8.28 for applied fields of -0.17 T (a) and -0.18 T (b) normal to the film surface.

8.2.3.3 Analysis of the coercivity mechanism with microstructural parameters

The temperature dependence of the coercivity of the epitaxially grown $L1_0$-$Fe_{60}Pt_{40}$ film of thickness 63.4 nm has been analyzed in a similar way as for the isotropic $L1_0$-$Fe_{50}Pt_{50}$ film.

The saturation of an epitaxially grown film is reached with an external field over 2 T applied along the out-of-plane direction. By substracting the linear region of the hysteresis loop in the high field region of 5 ~ 7 T, the correction of diamagnetism can be easily done, and the saturation polarization J_s is obtained.

The anisotropy constant K_1 values should have been determined by fitting the measured hysteresis loops to calculated ones. However, for a $L1_0$-FePt ordered film with anisotropic magnetization behavior, the saturation approach for fields applied along the hard axis is not possible since at 7 T no saturation is reached. 7 T is the maximum field of the SQUID magnetometer.

An alternative way to obtain K_1 is to measure the initial susceptibility of the virgin magnetization curve and use the following relation at different temperatures

$$\chi = \frac{J_S^2}{2K_1} \quad . \tag{8.4}$$

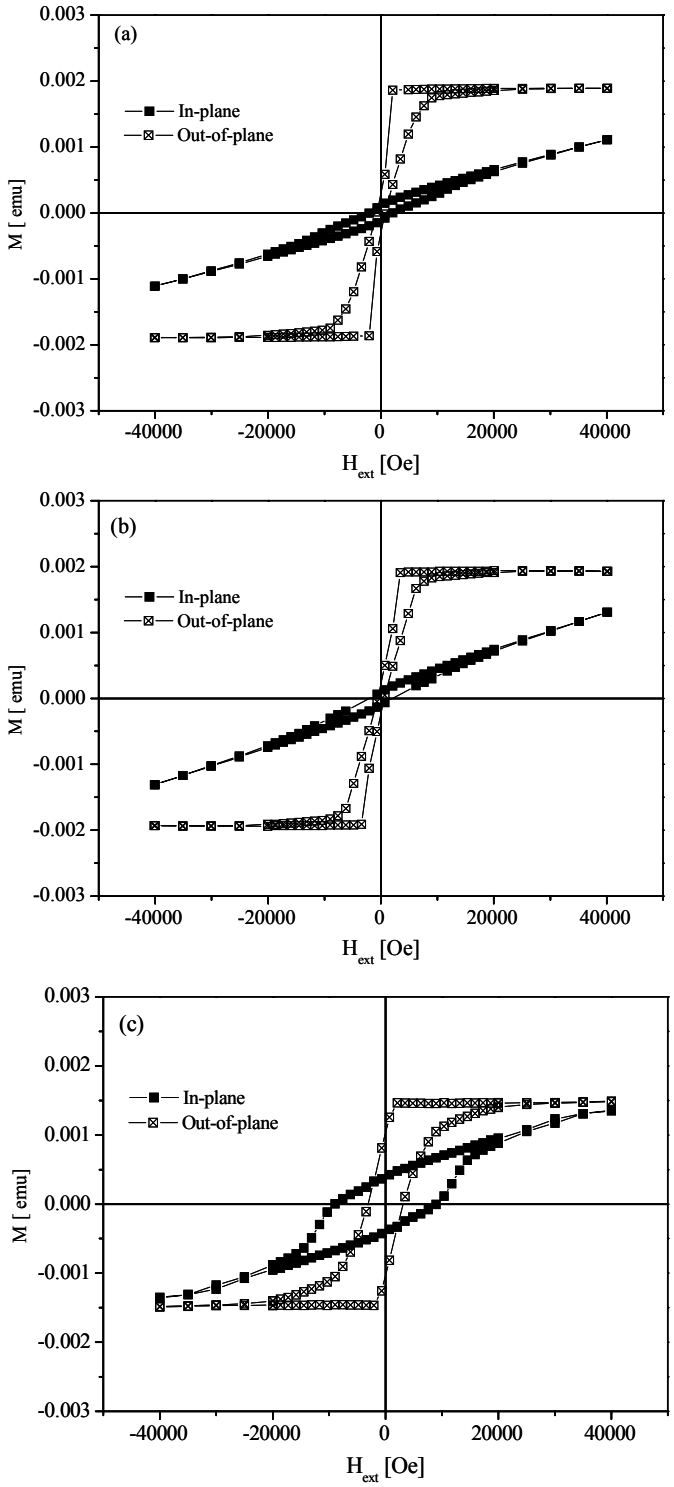

Fig 8.30 Magnetic hysteresis loops measured at 40 K of a $L1_0$-$Fe_{60}Pt_{40}$ film (precursor: (Pt 14 Å / Fe 16 Å)×18 / MgO) after annealing at 700 °C: (a) for 120 min (b) for 240 min and (c) for 660 min.

This method requires a demagnetized sample for each temperature of the measurement of the initial susceptibility. To demagnetize the $L1_0$-FePt film a thermal demagnetization by heating above T_C was chosen. Unfortunately this failed due to the gradual oxidation of the film during the heat-treatments. Therefore for a first approximation the same K_1 values were taken as determined for the isotropic $L1_0$-$Fe_{50}Pt_{50}$ sample. Again the K_1, J_s and coercivity $\mu_0 H_c$ at different temperatures were plotted using the linear relation for anisotropic magnets

$$\frac{\mu_0 H_c(T)}{J_s(T)} = \mu_0 \frac{2K_1(T)}{J_s^2(T)} \cdot \alpha - N_{eff} \,. \tag{8.5}$$

Table 8.6 lists all values used for plotting. The microstructural parameters obtained from Fig. 8.31 are α = 0.012 and N_{eff} = 0.0034.

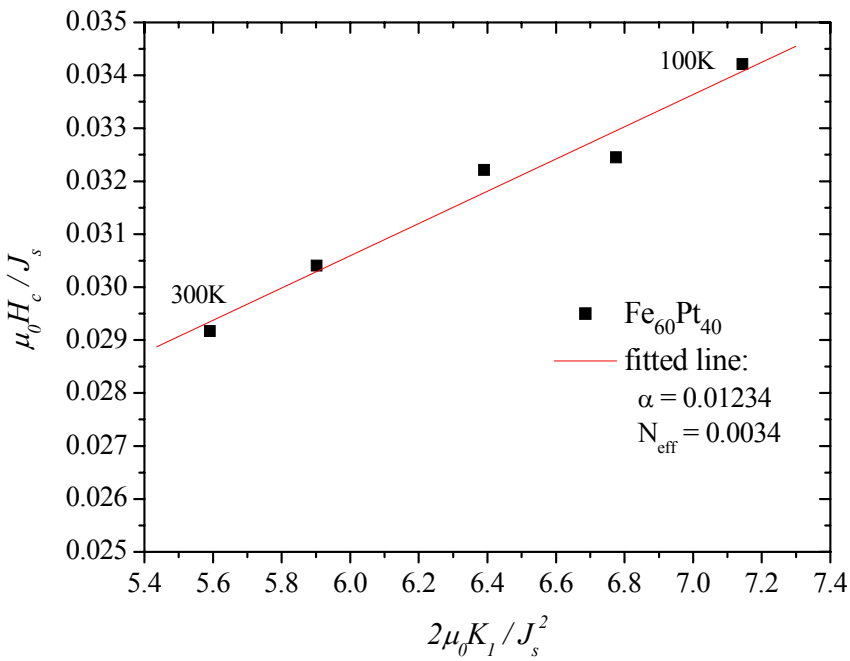

Fig. 8.31 Microstructural parameters of the epitaxially grown $L1_0$-$Fe_{60}Pt_{40}$ film with anisotropic magnetization behavior.

T [K]	$\mu_0 H_c$[T]	K_1 [MJ/m^3]	J_s [T]	$2\mu_0 K_1 / J_s^2$	$\mu_0 H_c / J_s$	A [pJ/m]
100	0.052	6.55	1.52	7.14	0.0342	7.60
150	0.049	6.13	1.51	6.77	0.0324	7.55
200	0.048	5.63	1.49	6.39	0.0322	7.46
250	0.045	5.13	1.48	5.90	0.0304	7.41
300	0.042	4.60	1.44	5.59	0.0291	7.21

Table 8.6 Values for determining the microstructural parameters of the $L1_0$-$Fe_{60}Pt_{40}$ film.

9. Discussion

9.1 Formation mechanism for the $L1_0$-phase

By in-situ TEM experiments the formation mechanism of the ordered $L1_0$-phase from Fe/Pt multilayers has been investigated during annealing.

9.1.1 Epitaxial $L1_0$-FePt films

As shown in Fig. 8.4 in the as-deposited multilayer Fe (110) planes and Pt (001) planes are oriented parallel to the MgO (001) substrate. If the temperature is increased Fe atoms start diffusing into the Pt layers. At 390 ºC nuclei of $L1_0$-FePt alloy are found in the Pt layers whereas in the shrinking Fe layers a formation of the ordered $L1_0$-phase does not occur. If the specimen is kept at 390 ºC for one hour the increasing volume fraction of $L1_0$-FePt results in additional spots in the Fourier transform of the image (see marked spots in the inset of Fig. 9.1a and Fig. 9.1b). These spots are used to create a Fourier-filtered image in which the locations of ordered $L1_0$-FePt appear as bright regions in Fig. 9.1a. With further heating up to 690 ºC the Fe/Pt multilayer structure is completely disappreaed by intermixing and the ordered $L1_0$-$Fe_{60}Pt_{40}$ phase is formed nearly completely (Fig. 9.1b).

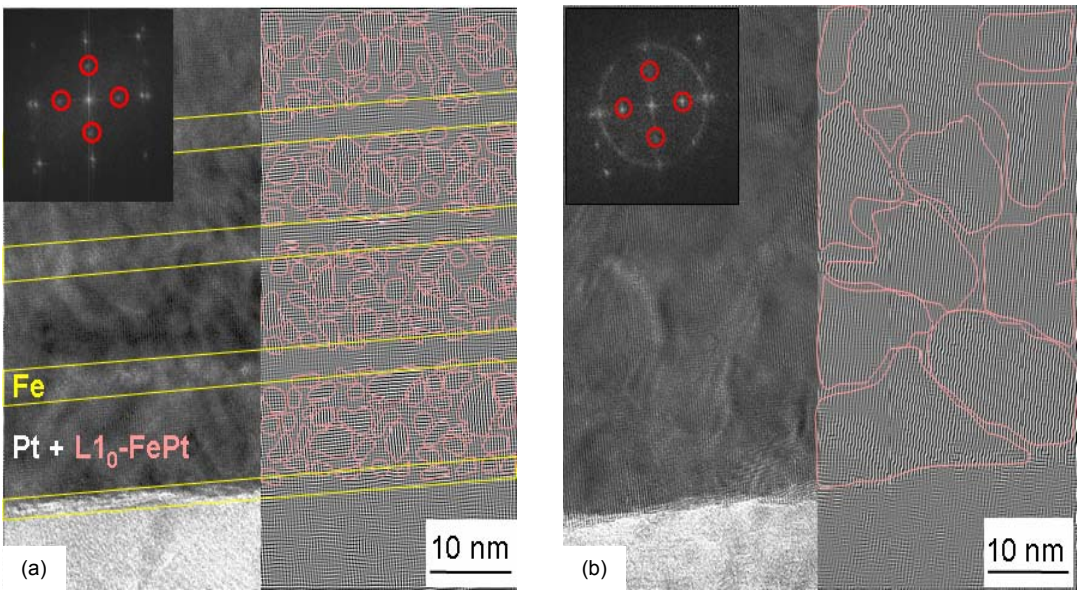

Fig. 9.1 High-resolution TEM images of (Pt 54 Å / Fe 64 Å)×5 multilayer grown on MgO (001) substrate: (a) after holding the temperature at 390 ºC for one hour and (b) at 690 ºC. The right part of each image is Fourier filtered. For the four filtered images the four spots (inset of each figure) resulting from $L1_0$-$Fe_{60}Pt_{40}$ are used. The regions of $L1_0$-FePt formation are marked in the Fourier filtered images.

This investigation shows for the first time that the transformation of the ordered $L1_0$ phase from Fe/Pt multilayers starts from small nuclei in the Pt layers with a consumption of the Fe layers.

9.1.2 Polycrystalline $L1_0$-FePt films

In contrast to the Fe/Pt multilayers used for epitaxial $Fe_{60}Pt_{40}$ films, the Fe/Pt multilayers which transform into a polycrystalline film during annealing contained already grains and grain boundaries in the as-deposited state. The difference in the as-deposited multilayer structure between $Fe_{50}Pt_{50}$ and $Fe_{60}Pt_{40}$ films is due to the thinner Fe layers in $Fe_{50}Pt_{50}$ films. To achieve polycrystalline films the Fe layers in the $Fe_{50}Pt_{50}$ film are expected to be deposited as very thin layers of about 11 Å. Due to the high enthalpy of mixing between elemental Fe and Pt and the higher diffusivity of Fe atoms, the thin Fe layer of a Fe-Pt bilayer on MgO will not remain a single crystalline layer and grains are formed in the Fe layer. Subsequent multilayer stacks then also grow as grains on these initial grains. Therefore the multilayer has already grain structure after deposition as shown in Fig. 8.5.

9.2 Influence of composition on the $L1_0$-FePt alloy film

9.2.1 Formation of epitaxially grown films

During the formation of the $L1_0$-FePt ordered phase from Fe-Pt multilayers, the strain relaxation is an important factor to control the final structure of the ordered alloy film.

The strain may originate from various sources such as the different thermal expansion between substrate and film, the residual stress of the as-deposited multilayer, the volume shrinkage during phase transformation, grain growth during the annealing process and the lattice mismatch between substrate and film layer [78, 79]. In case of $L1_0$-FePt film growth, the major strain source is the misfit strain between the MgO substrate and the ordered $L1_0$-FePt phase. The other strain sources can be neglected. The thermal expansion coefficient of MgO and the $L1_0$-FePt ordered phase is nearly the same[15]. Thus the thermally induced stress during heating and cooling is negligible. The residual stress of the as-deposited film is relaxed in the interfaces between elemental Fe and Pt layers of multilayer structure. The strain of volume shrinkage during the phase transition from fcc FePt alloy (lattice parameter a = 3.816 Å) to the fct (lattice parameters a = 3.853 Å, c = 3.736 Å) is smaller than the strain from the lattice misfit resulting from the $L1_0$-FePt film and MgO substrate (lattice parameter a = 4.217 Å). Therefore, at the final

step of the ordered alloy film formation, the kind of relaxation mechanism of the misfit strain mainly favors the evolution of epitaxially grown films. For a film thickness of about 54 nm and with increasing Fe content in the nominal composition of the film, the perpendicular alignment of the tetragonal *c*-axis is improved and finally for the $Fe_{60}Pt_{40}$ nominal composition an epitaxially grown film is obtained with the uniaxial *c*-axis perpendicular to the film plane (Table 8.2 and Fig 9.1). When the lattice parameters were experimentally determined from X-ray diffraction for the epitaxially grown $Fe_{60}Pt_{40}$ film, the value of a = 3.882 Å is larger than the value for a stoichiometric bulk $L1_0$-FePt alloy, a = 3.853 Å, indicating that the misfit strain elongated the *a*-axis in the in-plane direction.

On the other hand, the lattice parameter of the $Fe_{50}Pt_{50}$ film is a = 3.863 Å, which is similar to the bulk value. In this case the *a*-axis of the film layer does not expand but grains are formed. In case of the 54 nm thick film, Fe-rich $L1_0$-FePt films seem to reduce their strain energy by elongation of the *a*-axis in the in-plane direction, which favors the formation of epitaxially grown films on the MgO substrate. However, for 27 nm thick films of the nominal composition of $Fe_{53}Pt_{47}$, an epitaxially grown $L1_0$-$Fe_{50}Pt_{50}$ film is also formed by annealing at 700 ºC. From these facts it seems that the epitaxial growth of the $L1_0$-FePt films is preferred not only by Fe-rich composition but also thinner film thicknesses.

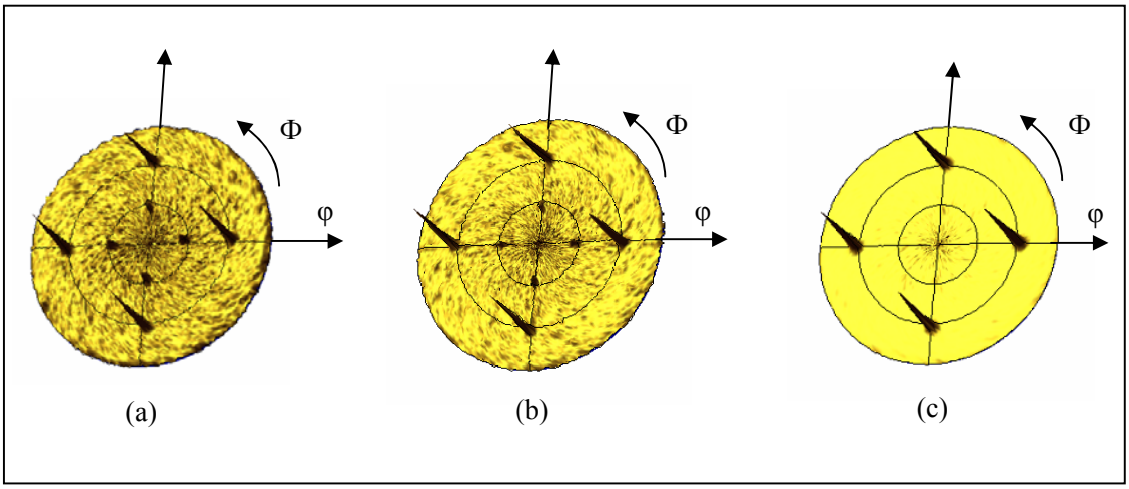

Fig. 9.1 X-ray pole figures for (201) peak of $L1_0$-FePt alloy films of different compositions: (a) $Fe_{50}Pt_{50}$, (b) $Fe_{57}Pt_{43}$, and (c) $Fe_{60}Pt_{40}$.

9.2.2 Amount of $L1_0$-phase formation

By analyzing the X-ray diffraction peaks of $L1_0$-FePt films, the ordering parameter was evaluated as mentioned in Chapter 6. Table 9.1 presents the values of the ordering parameter for three different compositions. The ordering parameter shows the highest value for the measured composition of $Fe_{49.5}Pt_{50.5}$. Although this is approximately the stoichiometric composition, the ordering parameter is still less than 1.0. This is due to the fact that the alloy film has a polycrystalline structure and the diffraction peak intensities ($I_{(001)}$ and $I_{(002)}$) which are needed to calculate the ordering parameter are varying from the ideal value of a single crystal due to the diffuse scattering in the grain boundaries. The ordering parameter of the epitaxially grown $Fe_{60}Pt_{40}$ film is 0.730, which is much lower than the ideal value of 1.0. This means that there are many vacancies or substitutional atoms in the ordered crystal lattice caused by the excess amount of Fe atoms. The ordering parameter of the film containing much more Pt is also less than that for the film of $Fe_{49.5}Pt_{50.5}$ composition which besides vacancies or substitutional atoms may be due to the fact that the composition is close to the phase boundary for the $L1_0$-phase, and disordered regions may exist.

Nominal composition	Measured composition	Ordering parameter
$Fe_{60}Pt_{40}$	$Fe_{59.9}Pt_{40.1}$	0.730
$Fe_{57}Pt_{43}$	$Fe_{49.5}Pt_{50.5}$	0.796
$Fe_{50}Pt_{50}$	$Fe_{46.1}Pt_{53.9}$	0.671

Table 9.1 Ordering parameters for $L1_0$-FePt films of various compositions.

9.2.3 Magnetic properties

As the $L1_0$-FePt film structure varies with composition and individual layer thickness, the magnetic properties sensitively depend on the composition. In the case of film thicknesses of about 54 nm, especially the films which contain more Fe are epitaxially grown films, showing a perpendicular magnetic anisotropy in the hysteresis loops (Fig. 8.30a). With decreasing Fe content, the magnetic properties change and show larger in-plane coercivities as presented in Fig. 8.13 and Fig. 8.23 for a film with randomly oriented grains and a partially anisotropic film, respectively. A higher Fe content results in a stronger perpendicular magnetic anisotropy, which

is due to a better alignment of the *c*-axis perpendicular to the film plane. The different structure between an epitaxially grown $L1_0$-FePt film and a polycrystalline film also affects the value of the coercivity $\mu_0 H_c$. Comparing the hysteresis loops between a polycrystalline and an epitaxial film of nearly the same thickness of about 60 nm shows that the coercivity value of the polycrystalline film $\mu_0 H_c$ = 1.1 T is much higher than for the epitaxial film, $\mu_0 H_c$ = 0.04 T. The reason for this is that the polycrystalline films contain small particles which are in the single domain state for which magnetization reversal takes place by the coherent rotation of the magnetic polarization J_s. By increasing the particle size over the critical particle size of the single domain state, domains are nucleated inside the particles and the coercivity decreases significantly. The polycrystalline film of $L1_0$-$Fe_{50}Pt_{50}$ composition is composed of grains whose average size is 72.5 nm (Fig. 8.10), which is much smaller than the critical size for the single domain state in $L1_0$-FePt, which is around 450 nm. On the other hand, the epitaxial film of $Fe_{60}Pt_{40}$ composition can be considered as one big grain. Therefore many reversed domains can be easily nucleated inside the film during demagnetization. The small coercivities of the epitaxial films are due to the multidomain state existing in large particles.

9.3. Influence of the film thickness for epitaxial films

measured composition	thickness [nm]	$\mu_0 H_c$ [T]
$Fe_{60}Pt_{40}$	7.5	0.28
$Fe_{50}Pt_{50}$	15	0.12
$Fe_{50}Pt_{50}$	27	0.08
$Fe_{60}Pt_{40}$	54	0.06

Table 9.2 Coercivities of $L1_0$-FePt films of two different compositions with different thicknesses. The coercivities were measured at 40 K.

Table 9.2 shows the coercive field $\mu_0 H_c$ of epitaxially grown films with different thicknesses. It is found that the coercivity increases with decreasing film thickness. This behavior can be explained by the thickness dependence of the effective demagnetization factor N_{eff}. According to eq. (2.19) the coercivity depends on the effective demagnetization factor

$$\mu_0 H_c = \mu_0 \frac{2K_1}{J_s}\alpha - N_{eff} J_s \ . \tag{2.19}$$

In case of an epitaxially grown single crystalline film, the effective demagnetization factor N_{eff} increases with increasing larger thickness due to the increasing surface roughness.

9.4 Microstructural parameters

By determining the microstructural parameters of epitaxially grown and polycrystalline $L1_0$-FePt films with similar thicknesses of 54 nm and 53 nm, respectively, the coercivity mechanism can be analyzed. For the $L1_0$-$Fe_{50}Pt_{50}$ film with a polycrystalline structure and isotropic magnetization behavior, the values of α and the N are 0.306 and 0.358, respectively. However, for the epitaxially grown $L1_0$-$Fe_{60}Pt_{40}$ film with perpendicular magnetic anisotropy, the value of α is 0.019 and N_{eff} is 0.0032. The value of α is directly related to the coercivity which is much larger for the polycrystalline films compared to the epitaxially grown films.

The value of N_{eff} is directly related to the grain shape in the films. In the case of polycrystalline films the large N_{eff} values result from polyhedral grains with sharp edges and corners which are present in isotropic $L1_0$-$Fe_{50}Pt_{50}$ films according to Fig. 8.10. The polyhedral grain shape results in enhanced stray fields at the edges and corners of the grains.

On the other hand, the α value of the epitaxial $L1_0$-$Fe_{60}Pt_{40}$ film (α = 0.01234) is very small and close to zero. This reflects the small coercivity of $\mu_0 H_c$=0.06 T which is due to the formation of small domains inside the films with no effective pinning centers which would prevent domain wall motion. The N_{eff} value is also close to zero and can be neglected compared to that of the $L1_0$-$Fe_{50}Pt_{50}$ film.

According to eq. (9.2) N_{eff} value of 5.50×10^{-5} is expected. The N_{eff} value determined from the temperature dependence of the coercivity was 3.2×10^{-3}. The higher value is due to enhanced stray fields at the edges and corners of the square film.

From the analysis the following conclusions can be drawn. In the case of polycrystalline films, the coercivity mechanism is of nucleation-type, whereas in the case of epitaxially grown films it is of pinning-type and domain walls are nucleated.

In case of polycrystalline films the coercivity is much smaller than the ideal nucleation field of $\mu_0 2K_1/J_s$ due to the exchange interaction between neighboring grains, grain boundaries and the enhanced stray fields of the polycrystalline grains.

9.5 Influence of the annealing time

From the analyses of the hysteresis loops for films heat treated for different annealing times, it is found that the quality of epitaxial films and the coercivity of isotropic films are affected by annealing duration. In Fig. 9.4 the influence of the annealing time on the coercivity is plotted for epitaxial $L1_0$-$Fe_{60}Pt_{40}$ films, partially textured $L1_0$-$Fe_{57}Pt_{43}$ films, and for isotropic $L1_0$-$Fe_{50}Pt_{50}$ films.

In the case of epitaxially grown films, the magnetic anisotropy is decreasing by with increasing the annealing time over 240 min. This means that the epitaxial structure of film is degraded by the formation of misoriented grains.

In the case of partially textured films the hysteresis loops did not change for different annealing times.

In the case of the isotropic films, increasing the annealing time over 240 min leads to a decrease of the coercivity, but does not change the isotropic character. This change of the coercivity with the annealing time seems to be caused by the formation of large grains during long annealing times.

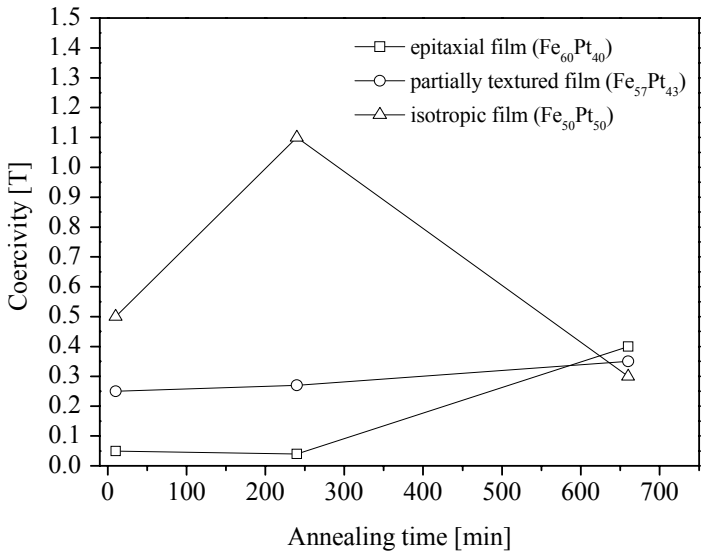

Fig. 9.3 Variation of the coercivity measured at 40 K with increasing the annealing time.

10. Summary

The Fe/Pd and Fe/Pt multilayers have been deposited by ion beam sputtering. This technique allows to easily vary the composition by changing the individual layer thicknesses. By applying different annealing temperatures, and times the transformation into the ordered $L1_0$- phase was studied. The annealing parameters for epitaxial and polycrystalline film growth have been optimized. The correlation between the microstructure and the magnetic properties could be quantitatively analyzed by determining the microstructural parameters within the framework of the theory of micromagnetism.

1. $L1_0$-FePd thin films

- By annealing treatment at 500 ºC for 30 min in high vacuum and hydrogen atmosphere, the Fe/Pd multilayers on quartz substrates transform into the ordered $L1_0$-FePd films with (111) texture.

- The atmosphere during the annealing treatment of the multilayers affects the microstructure and magnetic properties of the resulting ordered $L1_0$-FePd films. Annealing of the multilayers in vacuum results in higher coercive fields and better squareness of the hysteresis loops than annealing in hydrogen atmosphere. It is found that compared to in vacuum annealed samples the surfaces of in hydrogen heat-treated samples are very rough and the grain sizes are rather large. This is due to an abnormal grain growth in the films during annealing in a reducing atmosphere.

- If the Fe/Pd multilayers are deposited on MgO substrates and annealed at 500 ºC for 30 min in Ar atmosphere the resulting ordered $L1_0$-FePd film can be easier magnetized when the external field is applied perpendicular to the film layer, i.e. the out-of-plane direction is a preferred orientation due to the chemical ordering to $L1_0$-FePd.

2. $L1_0$-FePt thin films

- *Fe/Pt multilayers*

Fe/Pt multilayers deposited on a MgO (001) substrate are composed of layers which are oriented such that Fe (110) planes (*d*-spacing 0.203 nm) and Pt (100) planes (*d*-spacing 0.196 nm) are parallel to Mg (100) planes (*d*-spacing 0.21 nm) in order to minimize the strain energy in the layers. In the case of very thin individual Fe layers, e.g. for (Pt 14 Å / Fe 16 Å) × 21 the Fe/Pt multilayers may contain grains in the as-deposited state.

All the Fe/Pt multilayers show a typical soft magnetic behavior resulting from the Fe layers. The shape anisotropy is dominant and the magnetic anisotropy of the multilayers does not depend on the elemental layer thicknesses.

- *Formation mechanism of $L1_0$-FePt*

For the first time, the formation mechanism of epitaxially grown ordered $L1_0$-FePt monolayers of composition $Fe_{60}Pt_{40}$ from Fe-Pt multilayers was observed by in-situ heating in the TEM. The transformation into ordered $L1_0$-FePt starts from small nuclei in the Pt layers which are formed by Fe diffusion into the Pt layers and significantly grow in size during heating.

In the case of the presence of grains in the as-deposited Fe/Pt multilayers ordered $L1_0$-FePt is formed inside the grains during annealing resulting in polycrystalline $L1_0$-FePt films.

- *Microstructural and magnetic properties of $L1_0$-FePt films*

The final film composition after annealing are controlled by the individual layer thicknesses of the as-deposited Fe/Pt multilayers. The microstructure and magnetic properties of ordered $L1_0$-FePt are related to the Fe content in the films which could be shown for a film thickness of about 54 nm. Films with nominal composition of $Fe_{50}Pt_{50}$ show an isotropic behavior of the hysteresis loop, i.e. for fields applied parallel and perpendicular to the film plane, the hysteresis loops look like the same. These magnetic properties are due to the formation of polycrystalline grains with random orientation of the tetragonal *c*-axis. Films with nominal compositions of $Fe_{57}Pt_{43}$ and $Fe_{54}Pt_{46}$ are partly textured. Films with a Fe-rich composition, e.g. $Fe_{60}Pt_{40}$, and thicknesses thicker than 54 nm (e.g., precursors (Pt 14 Å / Fe 16 Å) × 18 / MgO and (Pt 56 Å / Fe 64 Å) ×5 / MgO) preferentially result in an epitaxial single layer with the tetragonal *c*-axis

aligned perpendicular to the film plane, and exhibit a high perpendicular magnetic anisotropy. By decreasing the film thickness to 27 nm also for nominal composition of $Fe_{53}Pt_{47}$ epitaxially grown films with a high perpendicular magnetic anisotropy are obtained (e.g. precursor (Pt 16Å / Fe 14 Å) × 9).

The coercivity $\mu_0 H_c$ of the epitaxial films for a given nominal composition increases with decreasing film thickness, due to the decreasing demagnetization factor N_{eff} and volume of the films.

- *Temperature dependence of the intrinsic magnetic properties of $L1_0$-FePt*

From the hysteresis loops measurements the temperature dependence of the anisotropy constant K_1, the spontaneous polarization J_s and the exchange constant A could be determined. All three intrinsic magnetic properties decrease with increasing temperature. At room temperature values of K_1 = 4.60 MJ/m^3, J_s = 1.43 T and A = 3.97 pJ/m are found for stoichiometric $Fe_{50}Pt_{50}$ films. The temperature dependence of the intrinsic magnetic properties is not known so far in literature. However, it is a basic requirement for the analysis of the coercivity by microstructural parameters.

- *Microstructural parameters of $L1_0$-FePt films*

For the $L1_0$-$Fe_{50}Pt_{50}$ films with a polycrystalline structure and isotropic magnetization behaviour, the values of α and N_{eff} are 0.306 and 0.358, respectively. For the epitaxially grown $L1_0$-$Fe_{60}Pt_{40}$ films with perpendicular magnetic anisotropy, the values of α and N_{eff} are 0.019 and 0.0032, respectively. The values of α is directly related to the coercivity which is much larger for polycrystalline films compared to the epitaxially grown films. The values of N_{eff} are directly related to the grain shape in the films and are larger for polycrystalline films due to the polyhedral grain shape resulting in enhanced stray field at the edges and corners of the grains. From the analysis it can be concluded that for polycrystalline films the coercivity mechanism is of nucleation-type and for epitaxially grown films of pinning-type where domain walls are nucleated.

The results obtained in the present thesis are a prerequisite to tailor $L1_0$-FePt films with optimized properties for technical applications. Depending on the individual layer thickness of

Fe/Pt multilayers, epitaxially grown or polycrystalline $L1_0$-FePt films can be realized during annealing. Especially the epitaxially grown $L1_0$-FePt films are very interesting candidates for realizing ultra-high density perpendicular recording media.

11. Zusammenfassung

Die wichtigste Frage in der magnetischen Datenspeichertechnologie ist, wie die Speicherdichte über 100 Gbit/inch^2 erhöht werden kann. Die konventionellen longitudinalen magnetischen Speichermedien kommen aufgrund des superparamagnetischen Effekts dafür nicht in Frage. Aussichtsreichste Kandidaten zur Erzielung von Speicherdichten von 1 TBit / inch^2 sind Speichermedien mit leichter Richtung senkrecht zur Schichtebene auf der Basis von $L1_0$-FePt und $L1_0$-FePd. Die groβen magnetokristallinen Anisotropien ($K_1(\mathrm{FePt}) = 6.6\ \mathrm{MJ/m^3}$, $K_1(\mathrm{FePd}) = 1.8\ \mathrm{MJ/m^3}$) resultieren in groβen Koerzitivfeldern, die wiederum die Voraussetzung für eine groβe thermische Stabilität der gespeicherten Information bilden. $L1_0$-FePt und $L1_0$-FePd entstehen z. B. durch Wärmebehandeln von Fe/Pt- und Fe/Pd- Viellagenschichten. Die $L1_0$-Phase besitzt eine fct-Struktur. Entlang der tetragonalen *c*-Achse wechseln sich atomare Lagen von Fe und Pt ab, wodurch sich eine strukturelle Anisotropie ergibt. Damit die tetragonale *c*-Achse senkrecht zur Schichtebene orientiert ist, werden in der Regel MgO (001) Substrate verwendet. Allerdings ist der genaue Mechanismus für das epitaktische Wachstum von $L1_0$-FePt-Schichten noch nicht bekannt.

In dieser Arbeit wurden mittels Ionenstrahlsputtern Fe/Pd und Fe/Pt Viellagenschichten hergestellt. Mit dieser Technik lässt sich die Zusammensetzung über die Schichtdichten der Einzellagen leicht verändern. Erstmals wurde die Umwandlung in die geordnete $L1_0$-Phase während der Wärmebehandlung bei verschiedenen Temperaturen und unterschiedlichen detailliert mittels in-situ-TEM untersucht. Die Anlassparameter wurden optimiert, um epitaktische oder polykristalline Schichten zu erhalten. Die Korrelation zwischen der Mikrostruktur and den magnetischen Eigenschaften konnte im Rahmen der Theorie des Mikromagnetismus mit Hilfe von Mikrostrukturparametern quantitativ analysiert werden. Für die Analyse war die Bestimmung der Temperaturabhängigkeit der intrinsischen magnetischen Eigenschaften von $L1_0$-FePt erforderlich. Im einzelnen wurden folgende Ergebnisse erzielt.

1. Dünne $L1_0$-FePd Schichten

- Fe/Pd Viellagenschichten auf Quartzsubstraten wandeln sich durch Anlassen bei 500 ºC für 30 min in Vakuum oder H_2-Atmosphäre in geordnete $L1_0$-FePd Schichten um, die dann eine (111) Textur aufweisen.

- Die Atmosphäre während der Wärmebehandlung der Viellagenschichten beeinflusst die Mikrostruktur und die magnetischen Eigenschaften der geordneten $L1_0$-FePd Schichten. Anlassen in Vakuum führt zu größeren Koerzitivfeldern und rechteckigeren Hysteresekurven als Anlassen in Wasserstoffatmosphäre. In Wasserstoffatmosphäre angelassene Proben weisen eine sehr raue Filmoberfläche mit großen Körnern auf.

- Fe/Pd Viellagenschichten auf MgO Substraten wandeln sich während einer Wärmebehandlung bei 500 ºC für 30 min in Argon in $L1_0$-FePd Schichten um, die eine Textur senkrecht zur Filmebene aufweisen.

2. Dünne $L1_0$-FePt Schichten

- Fe/Pt-Viellagenschichten:

  Fe/Pt-Viellagenschichten wachsen so auf MgO (001) Substraten auf, dass die Fe (110)-Ebenen (Gitterabstand 0.203 nm) und Pt (100)-Ebenen (Gitterabstand 0.196 nm) parallel zu den MgO (100)-Ebenen (Gitterabstand 0.210 nm) orientiert sind. Dadurch werden Spannungen in den Lagen minimiert. Im Falle von sehr dünnen Fe-Einzellagen bilden sich in den Fe/Pt Viellagenschichten Körner aus. Dies ist z. B. der Fall für (Pt 14 Å / Fe 16 Å) × 21.

  Alle Fe/Pt Viellagenschichten zeigen wegen der Fe-Schichten ein weichmagnetisches Verhalten. Die Formanisotropie ist die dominierende Form der magnetischen Anisotropie. Die magnetische Anisotropie der Viellagenschichten hängt nicht von der Dicke der Einzellagen ab.

- Bildungsmechanismus für $L1_0$-FePt:

  Zum ersten Mal ist es gelungen, mit Hilfe von in-situ Heizexperimenten im TEM die Bildung von epitaktisch gewachsenen $L1_0$-FePt Monolagen der Zusammensetzung $Fe_{60}Pt_{40}$ aus entsprechenden Fe/Pt-Viellagenschichten zu beobachten. Die Umwandlung in geordnetes $L1_0$-FePt geht von kleinen Keimen in den Pt Einzellagen aus. Diese Keime bilden sich während der Wärmebehandlung durch Diffusion von Fe in die Pt-Einzellagen. Ihre Größe nimmt mit zunehmender Dauer der Wärmebehandlung deutlich zu.

Sind in den Fe/Pt-Viellagenschichten Körner vorhanden, so bildet sich während der Wärmebehandlung innerhalb der Körner die geordnete $L1_0$-FePt Phase aus und man erhält polykristalline $L1_0$-FePt Schichten.

- Mikrostrukturelle and magnetische Eigenschaften der $L1_0$-FePt-Schichten

  Die Zusammensetzung der $L1_0$-FePt Schichten ist bestimmt durch die Dicke der Einzellagen der Fe/Pt Viellagenschichten. Die Mikrostruktur und die magnetischen Eigenschaften der $L1_0$-FePt Schichte hängen vom Fe Gehalt der Proben ab. Dies wurde am Beispiel von 54 nm dicken Schichten gezeigt:

  Für eine nominelle Zusammensetzung von $Fe_{50}Pt_{50}$ ist die Hysteresekurve isotrop, d. h. für Felder parallel und senkrecht zur Schichtebene sind die Hystereskurven identisch. Ursache hierfür ist die polykristalline Struktur der Schichten mit einer statistischen Orientierung der tetragonalen *c*-Achse in den einzelnen Körnern. Für eine nominelle Zusammensetzung von $Fe_{57}Pt_{43}$ und $Fe_{54}Pt_{46}$ sind die Schichten teilweise texturiert. Für sehr Fe-reiche nominelle Zusammensetzungen wie z. B. $Fe_{60}Pt_{40}$ und Schichtdicken größer als 54 nm erhält man epitaktisch gewachsene Schichten, bei denen die tetragonale *c*-Achse senkrecht zur Schichtebene orientiert ist.

  Bei kleinen Schichtdicken wie z. B. 27 nm wachsen auch Schichten mit einer nominellen Zusammensetzung von $Fe_{50}Pt_{50}$ epitaktisch und weisen eine groβe senkrechte magnetische Anisotropie auf.

  Für eine bestimmte nominelle Zusammensetzung nimmt das Koerzitivfeld von epitaktischen Schichten mit abnehmender Schichtdicke, aufgrund des kleiner werdenden Schichtvolumens und Entmagnetisierungsfaktors N_{eff} zu.

- Temperaturabhängigkeit der intrinsische magnetische Eigenschaften von $L1_0$-FePt-Schichten

  Aus den Messungen der Hysteresekurve konnte die Temperaturabhängigkeit der Anisotropiekonstante K_1, der spontanen Polarisation J_s und der Austauschkonstante A bestimmt werden. Mit steigender Temperatur nehmen alle drei intrinsischen magnetischen Eigenschaften ab. Bei Raumtemperatur wurden für stöchiometrische $Fe_{50}Pt_{50}$ Schichte Werte von K_1 = 4.60 MJ/m^3, J_s = 1.43 T und A = 3.97 pJ/m ermittelt.

Die Temperaturabhängigkeit der intrinsischen magnetischen Eigenschaften ist in der Literatur bisher noch nicht bekannt. Sie ist die Grundvoraussetzung für die Analyse des Koerzitivfelds mit Mikrostrukturparametern benötigt.

- Mikrostrukturparameter von $L1_0$-FePt-Schichten

  Für $L1_0$-$Fe_{50}Pt_{50}$ Schichten mit einer polykristallinen Struktur und isotropen Magnetisierungsverhalten wurden die Mikrostrukturparameter α und N_{eff} zu 0.306 und 0.358 bestimmt. Für die epitaktisch gewachsenen $L1_0$-$Fe_{60}Pt_{40}$ Schichten mit magnetischer Anistropie senkrecht zur Schichtebene wurden α- und N_{eff} -Werte von 0.019 und 0.0032 ermittelt.

  Der Mikrostrukturparameter α spiegelt direkt die Größe des Koerzitivfelds wieder. Das Koerzitivfeld ist bei polykristallinen Schichten deutlich größer als bei epitaktisch gewachsenen Schichten. Der Mikrostrukturparameter N_{eff} ist ein Maβ für die Beschaffenheit der Körner in den Schichten. Bei polykristallinen Schichten resultieren größere Werte für N_{eff}, da an den Ecken und Kanten der polyederförmigen Körner die Streufelder überhöht sind.

  Die Analyse hat gezeigt, dass es sich bei polykristallinen Schichten um einen keimbildungsgehärteten Mechanismus handelt, der für die groβen Koerzitivfelder verantwortlich ist.

  Bei den epitaktisch gewachsenen Schichten liegt ein Pinning-Mechanismus zugrunde, wobei die Domänenwände durch Keimbildung entstehen.

Mit den Ergebnissen dieser Arbeit ist es in Zukunft möglich, $L1_0$-FePt-Schichten mit optimierten magnetischen Eigenschaften maβgeschneidert für technische Anwendungen herzustellen. Je nach gewählter Schichtdicke der einzelnen Schichten in den Fe/Pt Viellagenschichten können während einer Wärmebehandlung epitaktisch gewachsene oder polykristalline $L1_0$-FePt Schichten realisiert werden. Insbesondere die epitaktisch gewachsenen $L1_0$-FePt Schichten sind interessante Kandidaten für die Realisierung von neuartigen magnetischen Speichermedien höchster Speicherdichte.

Literature

[1] E. Daniel and C. Denis, Magnetic recording: First 100 years IEEE Press, 1998.

[2] D. Weller and A. Moser, IEEE Trans. Magn. **35** (1999) 4423.

[3] S. Iwasaki, IEEE Trans. Magn. **20** (1999) 657.

[4] N. Hai, N. Dempsey, M. Veron, M. Verdier, and D. Givord, J. Magn. Magn. Mat. **257** (2003) L139.

[5] R. Skmoski and J. Coey, Permanent magnetism, Institute of Physics Publishing, Bristol and Philadelphia, 1999.

[6] R. Farrow, D. Weller, R. Marks, M. Toney, A. Cebolada, and G. Harp, J. Appl. Phys. **79** (1996) 5967.

[7] J. Thiele, L. Folks, M. Toney, and D.Weller, J. Appl. Phys. **84** (1998) 5686.

[8] M. Visokay and R. Sinclair, Appl. Phys. Lett. **66** (1995) 1692.

[9] C. Luo and D. Sellmyer, Appl. Phys. Lett. **75** (1999) 3162.

[10] T. Klemmer, D. Hoydick, H. Okumura, B. Zhang, and W. Soffa, Scr. Metall. Mater. **33** (1995) 1793.

[11] R. Farrow, D. Weller, R. Marks, M. Toney, S. Hom, G. Harp, and A. Cebolada, Appl. Phys. Lett. **69** (1996) 1166.

[12] A. Cebolada, D. Weller, J. Stitch, G. Harp, R. Farrow, R. Marks, R. Savoy, and J. Scott, Phys. Rev. B **50** (1994) 3419.

[13] M. Yan, N. Powers, and D. Sellmyer, J. Appl. Phys. **93** (2003) 8292.

[14] H. Zeng, M. Yan, N. Powers, and D. Sellmyer, Appl. Phys. Lett. **80** (2002) 2350.

[15] P. Rasmussen, X. Rui, and J. Shield, Appl. Phys. Lett. **86** (2005) 191915.

[16] Y. Endo, K. Oikawa, T. Miyazaki, O. Kitakami, and Y. Shimada, J. Appl. Phys. **94** (2003) 7222.

[17] W. Heisenberg, Z. Phys. **38** (1926) 441.

[18] W. Brown, Jr., Phys. Rev. **58** (1940) 736.

[19] W. Brown, Jr., Micromagnetics, Interscience Publishers, 1963.

[20] R. Fischer, T. Schrefl, H. Kronmüller, and J. Fidler, J. Magn. Magn. Mat. **150** (1995) 329.

[21] R. Hertel and H. Kronmüller, Phys. Rev. B **60** (1999) 7366.

[22] A. Hubert and R. Schäfer, Magnetic domains, Springer, 1998.

[23] E. Kneller, Ferromagnetismus, Springer, 1962.

[24] E. Frei, S. Shtrikman, and D. Treves, Phys. Rev. **106** (1957) 446.

[25] H. Kronmüller, Phys. Stat. Sol. (b) **144** (1987) 385.

[26] M. Sagawa and S. Hirosawa, J. Phys. Paris Colloque **49** (1987) 617.

[27] H. Kronmüller, K. Durst, and G. Martinek, J. Magn. Magn. Mat. **69** (1987) 149.

[28] G. Martinek and H. Kronmüller, J. Magn. Magn. Mat. **86** (1990) 177.

[29] H. Kronmüller and M.Fähnle, Micromagnetism and the microstructure of ferromagnetic Solids, Cambridge press, 2003.

[30] H. Kronmüller, K. Durst, and M. Sagawa, J. Magn. Magn. Mat. **74** (1988) 291.

[31] H. Kronmüller, J. Appl. Phys. **52** (1981) 1859.

[32] H. Danan, in Colloque Nationale de Magnetisme, CNRS, 1958, p. 81.

[33] M. Neel, R. Pauthenet, G. Rimet, and V. Gion, J. Appl. Phys. **31** (1960) 279.

[34] J. Hong, J. Kane, J. Hashimoto, M. Yamagishi, K. Noma, and H. Kanai, in 12th Magnetic recording conference, 2001.

[35] Z. Zhang, in Intermag. Europe 2002, 2002.

[36] M. Plumer, J. V. Ek, and D. Weller, The physics of high density magnetic recording, Springer, 2001.

[37] A. Moser, K. Takano, D. Margulies, M. Albrecht, Y. Sonobe, Y. Ikeda, S. Sun, and E. Fullerton, J. Phys. D **35** (2002) R157.

[38] M. Noda, IEEE Trans. Magn. **37** (2001) 75.

[39] W. Bennett, B. Zhang, and H. Richter, IEEE Trans. Magn. **34** (1998) 743.

[40] J. Wang, M. Alex, P. Tan, and M. Yan, J. Appl. Phys. **85** (1999) 4997.

[41] E. Fullerton, D. Margulies, M. Schabes, M. Caney, B. Gurney, A. Moser, M. Best, G. Zelter, J. Rubin, and H. Rosen, Appl. Phys. Lett. **77** (2000) 3806.

[42] B. Engel, C. England, R. V. Leeuwen, M. Wiedmann, and C. Falco, Phys. Rev. Lett. **67** (1991) 1910.

[43] G. Bertero and R. Sinclair, Appl. Phys. Lett. **64** (1994) 3997.

[44] J. MacLaren and R. Victoria, Appl. Phys. Lett. **66** (1995) 3377.

[45] H. Takano, Y. Nishida, A. Kuroda, H. Sawaguchi, Y. Hoseoe, T. Kawabe, H. Aoi, H. Muraka, Y. Nakamura, and K. Ouchi, J. Magn. Magn. Mat. **235** (2001) 241.

[46] T. Leonhardt, Y. Chen, M. Rao, D. Laughlin, D. Lambeth, and M. Kryder, J. Appl. Phys. **85** (1999) 4307.

[47] T. Suzuki, T. Kiya, N. Honda, and K. Ouchi, IEEE Trans. Magn. **36** (2000) 2417.

[48] D. Laughlin, S. Kumar, Y. Peng, and A. Roy, IEEE Trans. Magn. **36** (2005) 2402.

[49] R. Victoria and J. MacLaren, Phys. Rev. B **47** (1993) 11583.

[50] A. Kikukawa, Y. Honda, Y. Hirayama, and M. Futamoto, IEEE Trans. Magn. **36** (2000) 2402.

[51] Y. Ikeda, Y. Sonobe, and H. Uchida, IEEE Trans. Magn. **34** (2000) 3097.

[52] Y. Sonobe, Y. Ikeda, and Y. Tagushira, IEEE Trans. Magn. **35** (1999) 2769.

[53] T. Massalski, ed., Binary Alloy Phase Diagrams, ASM international, 1990.

[54] O. Gutfleisch, J. Lyubia, K. Müller, and L. Schultz, Advanced Engineering Materials 7 (2005) 208.

[55] T. Shima, K. Takanashi, Y. Takanashi, and K. Hono, Appl. Phys. Lett. **85** (2004) 2571.

[56] E. Bauer, Z. Kristallogr. 110 (1958) 372.

[57] C. You, Y. Takahashi, and K. Hono, J. Appl. Phys. 100 (2006) 056105.

[58] T. Shima, K. Takanashi, Y. Takanashi, K. Hono, G. Li, and S. Ishio, J. Appl. Phys. **99** (2006) 033516.

[59] J. Attane, Y. Samson, A. Mordy, D. Hally, and C. Beigue, Appl. Phys. Lett. **79** (2001) 794.

[60] J. Attene, Y. Samson, A. Mordy, J. Toussaint, G. Dubois, A. Mongin, and J. Jamet, Phys. Rev. Lett. **93** (2004) 25703.

[61] D. Smith, Thin-film deposition, Mc Graw-Hill, 1991.

[62] J. Harper and J. Cuomo, J. Vac. Sci. Tech. **21** (1982) 737.

[63] JCPDS cards, 29-0718, International center for powder diffraction, 1994.

[64] JCPDS cards, 43-1359, International center for powder diffraction, 1994.

[65] U. Welzel, J. Ligot, P. Lamparter, A. Vermendern, and E. Mittemeijer, J. Appl. Cryst. **38** (2005) 1.

[66] L. Reimer, Transmission electron microscopy, Springer, 1997.

[67] J. Clarke and A. Braginski, The SQUID handbook, Wiley-VCH, 2004.

[68] I. Schuller, Phys. Rev. Lett. **44** (1980) 1597.

[69] B. Warren, X-ray diffraction, Addison Wesley, 1969.

[70] B. Cullity, Elements of X-ray diffraction, Addison Wesley, 1978.

[71] L. Parratt, Phys. Rev. **95** (1954) 359.

[72] W. Sucksmith and J. Thomson, Proc. Roy. Soc. Lond. A **225** (1954) 362.

[73] F. von. Zeppelin, Diplomarbeit University of Stuttgart, 1999.

[74] D. Köhler, Dissertation University of Stuttgart, 1992.

[75] T. Wagner and D. Müller, Zeitschrift fur Metallkunde **93** (2002) 401.

[76] H. Callen and E. Callen, J. Phys. Chem. Solid **27** (1966) 1271.

[77] A. Forkl, M. Hirscher, T. Mizoguchi, H. Kronmüller, and H. Harbermeier, J. Magn. Magn. Mat. **93** (1991) 261.

[78] W. Zeiger, W. Brückner, J. Schumann, W. Pitschke, and H. Worcha, Thin Solid Films **370** (2000) 315.

[79] F. Witt and R. Vook, J. Appl. Phys. **39** (1968) 2773.

[80] A. Aharoni, J. Appl. Phys. **83** (1998) 3432.

Acknowledgements

This Ph.D. thesis has been carried out at the Max-Planck-Institute for Metals Research in Stuttgart. The financial support of the International Max-Planck-Research School for Advanced Materials is gratefully acknowledged.

I would like to acknowledge Prof. Dr. Gisela Schütz, who agreed to become the "Hauptberichter" in my examination.

I want to thank Prof. Dr. Eduard Arzt, who agreed to become the "Mitberichter" in my examination.

I also thank Prof. Dr. Fritz Aldinger, who agreed to become the "Prüfungsvorsitzender" in my examination.

I also thank Dr. Michael Hirscher for his support during my studies at the Max-Planck-Institute.

I would like to thank gratefully and sincerely Dr. Dagmar Goll for her guidance, understanding, and patience. Her mentorship was paramount in providing many experiences consistent with my long-term carrier goals in the field of magnetism. She encouraged me to grow not only as an experimentalist and an independent thinker. Without the encouragement and continual guidance from Dr. Dagmar Goll in the case of difficulties, I am not sure this thesis would have been completed. I would also like to thank the members of Dr. Dagmar Goll's research group, Achim Breitling, Stefan Soehnle, and Sebastian Macke for their understanding and help. Especially I am very grateful for the friendship of Achim Breitling, with whom I discussed closely and solved many experimental problems. I am sure he will get a great doctoral degree.

There were many other people in MPI-MF who helped me. Thanks to Theresa Dragon for her kind help in preparing TEM samples and taking Kerr microscope images. Bernd Ludescher kindly helped in preparing thin films samples. Together with Dr. Udo Welzel, and Maritta Dudek, I had many intensive discussions and I received from them all the X-ray pole figures of my samples. I thank Dr. Ewald Bischoff for composition analyses of FePt films. I thank Ulrike

Eigenthaler who produced the TEM samples in the FIB/SEM dual beam facility. Dr. Wilfried Sigle, and Marion Kelsch of the “Zentrum für Transmissionelektronen mikroskopie” performed the TEM investigations. I take this opportunity to express my appreciation to them.

I would like to thank my wife Dr. Yun Sung Woo for her support, encouragement, quiet patience and unwavering love.

Finally, and most importantly, I thank God for giving me the opportunity to study and live in Germany.

Curriculum Vitae

Nam Hoon Goo

Date of birth and birthplace: 4th August 1973, Seoul, Korea

Education:

- 1989-1992: Sung Nam High School, Seoul, Korea.
- 1992-1998: Bachelor in Metallurgical Engineering, Hanyang University, Seoul, Korea.
- 1998-2000: Master in Metallurgical Engineering, Hanyang University, Seoul, Korea.
- 2003-2007: Dissertation at the Max-Planck-Institute for Metals Research, Stuttgart, Germany.
- 2003-2007: Member of the Max-Planck-Research School for Advanced Material.